COMPUTER AIDED ANALYSIS OF LATE GADOLINIUM ENHANCED CARDIAC MRI

WEI DONG

(B.Eng.), Huazhong University of Science and Technology

A THESIS SUBMITTED FOR THE DEGREE OF

DOCTOR OF PHILOSOPHY

DEPARTMENT OF

ELECTRICAL AND COMPUTER ENGINEERING

NATIONAL UNIVERSITY OF SINGAPORE

2013

DECLARATION

I hereby declare that this thesis is my original work and it has been written by me in its entirety.

I have duly acknowledged all the sources of information which have been used in the thesis.

This thesis has also not been submitted for any degree in any university previously.

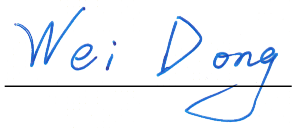

WEI DONG

May 22, 2013

Acknowledgements

I would like to thank my research advisors, Assoc. Prof. ONG Sim-Heng and Dr. SUN Ying, for their guidance and help during my Ph.D. candidature. I would also like to thank Dr. CHAI Ping, for his valuable advice from a cardiologist's point of view and drawing of the manual reference. Many thanks go to Dr. Lynette LS TEO as well for her drawing of the manual reference and help with the journal modification.

I would like to express my deepest gratitude to my thesis committee, Assoc. Prof. CHEONG Loong Fah, Dr. CHUI Chee Kong and the anonymous examiner for their valuable comments.

This thesis is not possible to be done without the support and encouragement from my family. I would like to thank my parents and wife for their unconditional support at all times during my graduate life. I would like to dedicate this thesis to my little daughter who motivated me most on my path to the Ph.D. degree.

Finally, I would like to thank the Academic Research Fund, National University of Singapore, Ministry of Education, Singapore for funding the CMR studies. I am also grateful to the radiographers and staff at the Department of Diagnostic Imaging, National University Hospital, Singapore, for helping with the CMR scans.

Contents

Summary

Viability assessment of the myocardium after myocardial infarction is essential for diagnosis and therapy planning. Late gadolinium enhanced (LGE) cardiac magnetic resonance (CMR) imaging protocol can directly visualize and thus discriminate non-viable myocardium (i.e., infarcts) from normal myocardium via hyper-enhanced intensities. Although the analysis of LGE CMR images can be done manually, it is not only time-consuming but also subject to inter-observer variation. Therefore, computer aided (semi-) automatic techniques are of great research values. Technically we divide the analysis of LGE CMR images into two stages: (i) myocardium segmentation and (ii) infarct classification within the segmented myocardium. In this thesis, we provide solutions for both stages.

For myocardium segmentation, we propose a comprehensive 3D method. Given myocardial contours in cine images as *a priori* knowledge, the method initially propagates the *a priori* segmentation from cine to LGE images via translational registration. Two meshes representing respectively endocardial and epicardial surfaces are then constructed with the propagated contours. After construction, the two meshes are deformed towards the myocardial edge points detected in both short-axis (SA) and long-axis (LA) LGE images in a unified 3D coordinate system. Based on the intensity characteristics of the left ventri-

cle (LV) in LGE images, we propose a novel parametric model of the LV for consistent myocardial edge points detection regardless of pathological status of the myocardium (infarcted or healthy) and of the type of the LGE images (SA or LA). Experimental results on both real patient and simulated phantom data have shown that the method is able to generate accurate segmentation for LGE images and is robust with respect to varied *a priori* segmentation in the referenced cine images. Two prominent novelties about this method are the effective utilization of the LA images and proposal of the novel parametric model of the LV.

For infarct classification, a novel method which employs a 3D graph-cut algorithm is proposed. Different from most related works, our method employs no threshold at all and is 3D in nature. Crucial pre-processing measures are taken to handle inconsistent intensities and misalignment artifacts across slices. Based on the bimodal intensity distribution of the LV and spatial continuity of the infarcted and normal myocardium, it then classifies the myocardium into infarcted and normal with the graph-cut algorithm. After a necessary post-processing step to eliminate potential false positives / negatives, infarct quantification can be generated from the segmented and classified myocardium. Qualitative and quantitative evaluations using real patient data have shown that our method is able to produce accurate classification results and has the potential to be developed further as a clinical tool to generate objective quantification of LGE CMR images.

List of Tables

LIST OF TABLES

List of Figures

List of Abbreviations

1D	One dimensional
2C	Two-chamber
2D	Two dimensional
3D	Three dimensional
4C	Four-chamber
4D	Four dimensional
AHA	American Heart Association
BA	Bland-Altman (Bland & Altman, 1986)
BP	Blood pool
CAD	Coronary artery disease
CMR	Cardiac magnetic resonance
CT	Computed tomography
DC	Dice coefficient (Dice, 1945)
DICOM	Digital Imaging and Communications in Medicine
ECG	Electrocardiography
I/M%	Infarct percentage
IOP	The 'ImageOrientationPatient' field in standard DICOM header
IPP	The 'ImagePositionPatient' field in standard DICOM header
LA	Long-axis
LAD	Left anterior descending
LCX	Left circumflex
LGE	Late gadolinium enhanced
LV	Left ventricle
MRI	Magnetic resonance imaging
MSD	Mean of squared differences
MVO	Microvascular obstruction
NCC	Normalized cross correlation
NMI	Normalized mutual information
PI	Pattern intensity (Weese *et al.*, 1997)
PS	The 'PixelSpacing' field in standard DICOM header
RCA	Right coronary artery
ROI	Region of interest
SA	Short-axis
SPAMM	SPAtial Modulation of Magnetization
XCAT	Extended cardiac-torso (Segars *et al.*, 2010)

Chapter 1

Introduction

This thesis aims at computer-aided automatic analysis of late gadolinium enhanced (LGE) cardiac magnetic resonance (CMR) images, including segmentation of the myocardium, as well as identification and quantification of myocardial infarcts. Section 1.1 briefly introduces the motivation behind the analysis of LGE CMR images. The scope and contributions of the thesis are highlighted in Section 1.2. Section 1.3 gives an overview of the organization of this thesis.

1.1 Motivation

Ischemic heart disease, or coronary artery disease (CAD), is one of the leading causes of death in western countries (Kishore & Michelow, 2011). It refers to the ischemia of cardiac muscles (i.e., the myocardium) due to stenosis of the supplying arteries. In the case of a severe stenosis or even complete occlusion, the patient undergoes a myocardial infarction, i.e., heart attack. Viability assessment of the myocardium is essential for diagnosis and therapy plan-

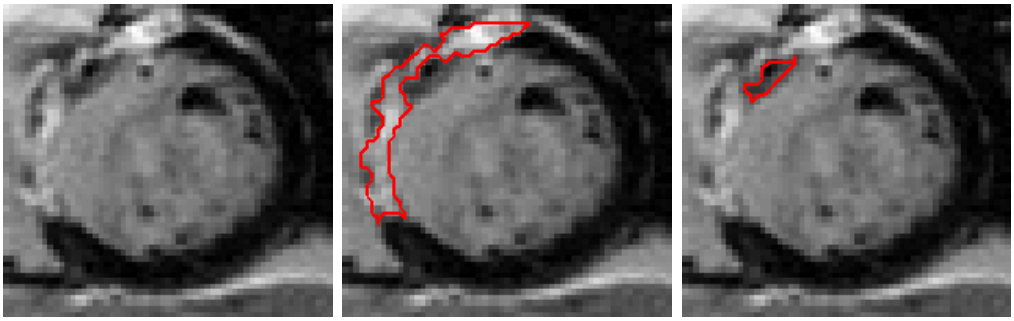

(a) (b) (c)

Figure 1.1: An example LGE image: (a) the original image; (b) the hyper-enhanced infarct is outlined. (c) the MVO is outlined.

ning after myocardial infarction. LGE CMR offers the capability to directly visualize and thus discriminate non-viable myocardium (i.e., infarcts) from normal myocardium (Kim *et al.*, 1999). In a typical LGE CMR examination, a gadolinium-based contrast agent is injected and a single-frame sequence is acquired 10-20 minutes later, by which time infarcts will exhibit hyper-enhanced intensities compared to healthy myocardium. This phenomenon has been hypothesized to be the result of delayed wash-out kinetics of the contrast agent in non-viable myocardium. Post-mortem histologic staining of the myocardium using animal models has shown that the hyper-enhanced regions in LGE CMR images correlate well with the location and extent of non-viable tissue (Fieno *et al.*, 2000; Kim *et al.*, 1999). One exception is the no-reflow phenomenon called *microvascular obstruction* (MVO), which is mostly observed in acute infarctions (Abdel-Aty & Tillmanns, 2010). In such cases, the infarcted subendocardial myocardium appear as dark as normal myocardium because no contrast agent can flow into these regions. Figure 1.1 shows an LGE image with a hyper-enhanced infarct and MVO.

Technically the analysis of LGE CMR images can be divided into two stages,

that is, segmentation of the myocardium and classification of infarcts inside the segmented myocardium. Although the analysis can be done manually by experts, it is not only time-consuming but also subject to inter-observer variation. Therefore, computer aided (semi-) automatic techniques are highly desired. However, the automation is not straightforward. First, automatic segmentation of the myocardium is often difficult due to the intensity heterogeneity of the myocardium and intensity similarity between the infarcts and blood pool (BP). Second, misclassification of infarcts can happen because of the intensity inconsistency and misalignment artifacts of a stack of slices, image noise and other artifacts. As far as we know, there are only few works on automatic myocardium segmentation in the literature, but more on automatic infarct classification given the myocardium segmented. Correspondingly, research works aimed at complete automatic analysis of LGE CMR images incorporating both stages are also very few.

An extra stage beyond the analysis of the LGE data itself is the joint analysis with complementary types of CMR data, which can reveal more insights than with the LGE CMR alone.

1.2 Scope and Contributions

This dissertation is aimed at the development of computer aided automatic techniques for the analysis of LGE CMR images. The goal is to achieve highly reliable, accurate, reproducible and efficient methods that require minimal user inputs.

We first propose a comprehensive 3D method for myocardium segmenta-

tion in LGE CMR images. Given myocardial contours in cine images as *a priori* knowledge, the method initially propagates the *a priori* segmentation from cine to LGE images via 2D translational registration. Two meshes representing respectively endocardial and epicardial surfaces are then constructed with the propagated contours. After construction, the two meshes are deformed towards the myocardial edge points detected in both short-axis (SA) and long-axis (LA) LGE images in a unified 3D coordinate system. Taking into account the intensity characteristics of the left ventricle (LV) in LGE images, we propose a novel parametric model of the LV for consistent myocardial edge points detection regardless of pathological status of the myocardium (infarcted or healthy) and of the type of the LGE images (SA or LA). The final meshes after the nonrigid deformation are themselves a 3D segmentation of the myocardium.

For subsequent infarct classification within the segmented myocardium, a novel method which employs a 3D graph-cut algorithm is proposed. Different from most related works, this method employs no threshold at all and is real 3D in nature. It also includes two crucial pre-processing measures – corrections of misalignment artifacts and intensity inconsistency – that were omitted or improperly handled in previous works. Based on the bimodal intensity distribution of the LV and spatial continuity of the infarcted and normal myocardium, it classifies the myocardium into infarcted and normal with the graph-cut algorithm. After a post-processing step to eliminate false positives / negatives, infarct quantification can be generated from the segmented and classified myocardium.

For both 3D myocardium segmentation and infarct classification, it is necessary to correct spatial and intensity distortions (i.e., misalignment artifacts and inconsistent intensities) in the set of LGE images beforehand. We propose

methods of handling these distortions: (i) For misalignment correction, an effective and robust method which improves upon the state of the art is proposed. This method not only utilizes the similarity at intersecting parts between slices, but also utilizes the intrinsic continuity of the heart throughout the stack of SA slices. It realigns the slices by minimizing a joint cost combining weighted dissimilarity measurements between the intersecting slices and between the contiguous SA slices. (ii) For intensity normalization, we propose a novel method which only considers local regional intensities of the LV and thus can effectively eliminate or reduce the intensity inconsistency in LV regions. The rationale underlying our normalization method is that intensities of the BP should be roughly the same across slices. To normalize the BP and hence LV intensities more accurately by avoiding negative impact from papillary muscles, the method employs an iterative algorithm based on the intensity distribution of the LV.

To summarise, this thesis makes the following contributions toward computer aided analysis of LGE CMR images:

1. Two effective methods that correct for the spatial and intensity distortions in a set of LGE images, before they can be processed together in 3D.

2. A comprehensive method for 3D myocardium segmentation. This method originally incorporates LA images to provide complementary information on myocardial boundaries between the largely spaced SA images, and adaptively deals with potential infarcts using a novel model of the LV in LGE images.

3. A 3D classification method to identify infarcts within the segmented myocardium. This method employs a volumetric graph-cut algorithm for a

real 3D classification and avoids the use of a global threshold.

These contributions together constitute a complete 3D processing flow of LGE CMR images (Fig. 1.2). In a nutshell , the overall contribution of this thesis is a complete and comprehensive 3D framework for computer aided analysis of LGE CMR.

Although in this thesis we do not present specific methods for the joint analysis of LGE and other types of CMR, such an analysis, in addition to the analysis of the non-viable myocardium in LGE CMR images, is important because it can reveal further insights for diagnosis and therapy planning. Therefore, we provide the basic background knowledge and also suggest future research directions for this joint analysis in addition to the LGE CMR analysis.

1.3 Thesis Organisation

Chapter 2 introduces the background knowledge about the anatomy of the human heart and ischemic heart disease, as well as basic knowledge about the CMR scans involved in this dissertation. Related works on computer aided analysis of LGE CMR images are also reviewed. Chapter 3 describes how we handle both intensity and spatial distortions of an LGE CMR volume, that is, inconsistent intensities and misalignment artifacts across slices of the volume. Chapter 4 presents our 3D method for myocardium segmentation in LGE CMR images as well as its experimental validation. Chapter 5 presents the 3D classification method that identifies infarcts within the segmented myocardium for quantitative analysis. It also includes the experimental validation of both the infarct classification method and the entire quantification framework. Chapter 6

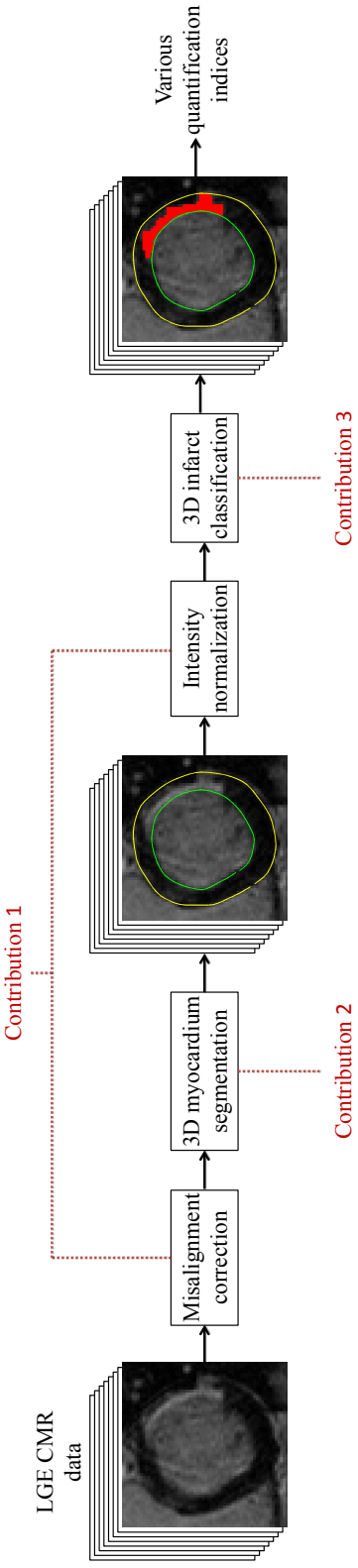

Figure 1.2: The complete processing flowchart of LGE CMR images in this thesis.

concludes this thesis and points out a few directions for future works.

Chapter 2

Background

This chapter provides the background knowledge about computer aided analysis of LGE CMR images. Section 2.1 introduces the anatomy of the human heart and ischemic heart disease. Section 2.2 introduces three commonly performed CMR scans on patients of ischemic heart disease and their correlations and differences. Section 2.3 introduces the standardized myocardial segmentation and nomenclature for tomographic imaging of the heart recommended by the American Heart Association. Section 2.4 discusses the two commonly existing spatial and intensity distortions (i.e., misalignment artifacts and intensity inconsistency, respectively), and reviews previous works on correction of these distortions. Sections 2.5 and 2.6 review related works on myocardium segmentation and infarct classification, respectively. Lastly Section 2.7 describes a few attempts for joint analysis of LGE CMR data with other types of cardiac scans.

2.1 Human Heart Anatomy and Ischemic Heart Disease

The human heart has four chambers (Fig. 2.1) and the pathway of blood through it consists of a pulmonary circuit and a systemic circuit:

- The left atrium is the upper left chamber that receives oxygenated blood from the lungs through the pulmonary veins and pumps the blood into the left ventricle through the mitral valve.
- The right atrium is the upper right chamber that receives blood from the superior vena cava and pumps the blood through the tricuspid valve to the right ventricle.
- The left ventricle is the lower left chamber that pumps oxygenated blood into the body through the aortic valve to the aorta.
- The right ventricle is the lower right chamber that pumps deoxygenated blood into the lungs through the pulmonary valve to the pulmonary arteries.

Of the four chambers, the left ventricle (LV) is the largest and strongest. It is also the most important because it is responsible for pumping the oxygenated blood to all parts of the body. Therefore, the LV draws most attention of cardiologists and its functionalities, abnormalities and pathologies have been extensively studied. The outer wall of the human heart consists of three layers. The outer layer is called the *epicardium*. The middle layer is called the *myocardium*, comprising cardiac muscles which contract to pump. The inner layer is called

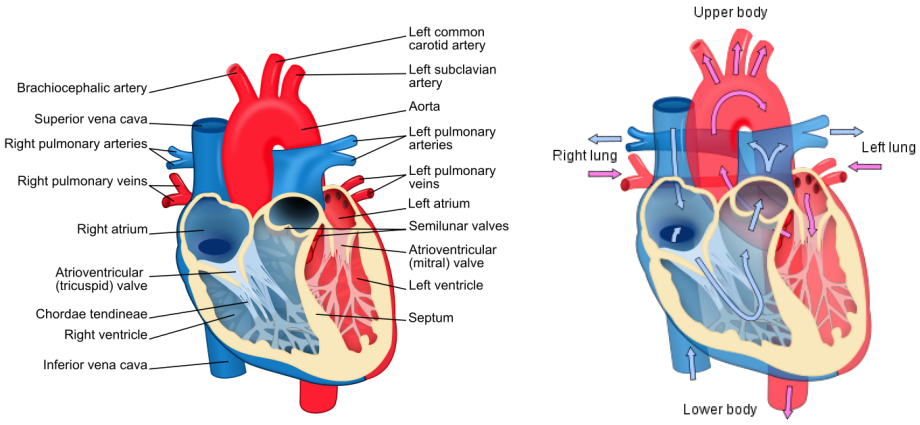

(a) (b)

Figure 2.1: Heart diagrams: (a) the heart anatomy; (b) the blood flow. The blue color indicates deoxygenated blood pathways and red indicates oxygenated pathways. These two images are from the Wikipedia (`http://en.wikipedia.org/wiki/Main_Page`).

the *endocardium*. The part of the myocardium that separates the left and right ventricles is called the *septum*.

As muscle tissue, the myocardium requires oxygen to operate. Oxygenated blood is supplied to the heart via *coronary arteries*, numerous vessels surrounding the heart. *Ischemic heart disease*, or coronary artery disease (CAD), refers to ischemia of the myocardium due to stenosis of the coronary arteries. It is one of the leading causes of death in western countries (Kishore & Michelow, 2011). If a stenosis develops to completely occlude the vessel, the patient undergoes a myocardial *infarction*, i.e., heart attack. The part of the myocardium which undergoes a prolonged shortage of oxygen is damaged and can be either non-viable or hibernating after the infarction. Only the hibernating myocardium has the potential to resume contraction after re-vascularisation (Rahimtoola, 1989). The infarcted non-viable myocardium is called infarct / infarction / scar interchangeably. Since the supplying arteries penetrates from epicardium inwards

to endocardium, in CAD the infarcts originate from sub-endocardium and grow outwards (Hunold *et al.*, 2005; Reimer *et al.*, 1979).

2.2 Cine, LGE and Tagged CMR

Magnetic resonance imaging (MRI) has become one of the standard clinical diagnostic tools for cardiovascular diseases and there are many different techniques optimized for the scan of the heart. In this dissertation, three specific imaging sequences are involved, that is, cine, LGE and tagged CMR.

2.2.1 Imaging Planes in CMR

Unlike CT scans, CMR scans are usually performed along the major axes of the LV instead of those of the body. The most frequently acquired image orientations in CMR include two LA views: the four-chamber (4C) and two-chamber (2C) views, and multiple contiguous SA views. If we consider the LV as a cone, then an SA view transects the LV with an imaging plane perpendicular to the axis of this cone (Figs. 2.2(a) and (d)). A series of parallel SA views are acquired from the mitral valve to the apex with a constant interval, covering the entire LV. Both the 4C and 2C views bisect the heart with imaging planes along the axis of the LV cone: while the 4C view cuts the heart through all the four chambers (Figs. 2.2(b) and (e)), the 2C view cuts the heart only through the left atrium and ventricle (Figs. 2.2(c) and (f)). Usually the stack of SA images is the major source of information in CMR studies while the 4C and 2C LA images are only used as supplementary reference when necessary. In practice, the LV is not a perfect cone and the imaging planes of the SA, 4C and 2C views are

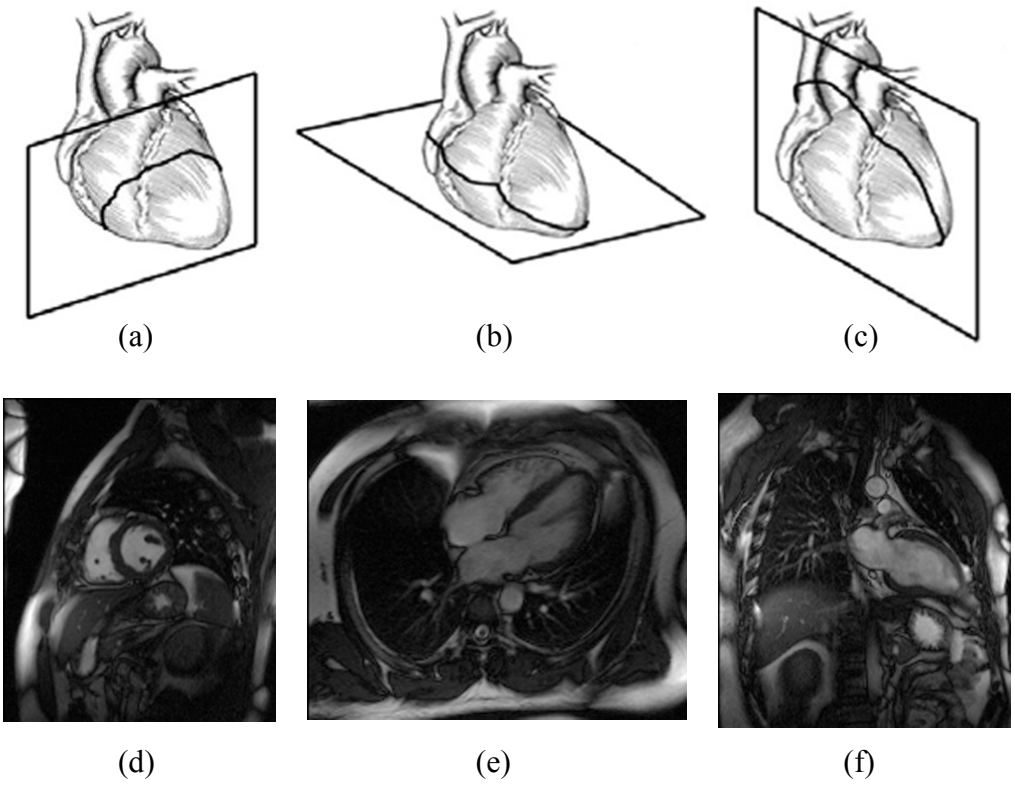

Figure 2.2: Most frequently acquired standard imaging planes in CMR: (a) the SA view; (b) the 4C view; (c) the 2C view; (d)-(f) exemplary SA, 4C and 2C cine CMR images.

not strictly perpendicular to each other. As there is no definite standard on how to determine orientations of the SA, 4C and 2C views, different strategies are adopted by CMR practitioners.

2.2.2 Cine CMR

Cine CMR can provide both anatomical and functional information of the heart. It produces consecutive frames corresponding to different phases of the cardiac cycle and hence can be used to calculate important functional indices such as ejection fraction. Electrocardiography (ECG) gating is commonly used for

phase prediction. In cine CMR images the blood is bright and the myocardium is dark, and the contrast between them is usually quite high. Figure 2.3 shows a mid-LV SA slice of cine CMR, including 24 frames covering the entire cardiac cycle [1] (for examples of LA cine images see Figs. 2.2(e) and(f)).

2.2.3 LGE CMR

Recall that viability assessment of the myocardium is essential for diagnosis and therapy planning after myocardial infarction (Section 1.1). In particular, the detection, localization and quantification of the infarcts, are important for determining whether and which part(s) of the myocardium may benefit from a re-vascularization therapy. Among various acquisition protocols used in CMR imaging, LGE imaging protocol offers the capability to directly visualize and thus discriminate infarcts from normal myocardium (Kim *et al.*, 1999). In a typical LGE CMR examination, a gadolinium-based contrast agent is injected and a single-frame sequence is acquired 10-20 minutes later, by which time infarcts will exhibit hyper-enhanced intensities compared to healthy myocardium. This phenomenon has been hypothesized to be the result of delayed wash-out kinetics of the contrast agent in non-viable myocardium. Post-mortem histologic staining of the myocardium using animal models has shown that the hyper-enhanced regions in LGE CMR images correlate well with the location and extent of non-viable tissue (Fieno *et al.*, 2000; Kim *et al.*, 1999). One exception is the no-reflow phenomenon called *microvascular obstruction* (MVO), which is mostly observed in acute infarctions (Abdel-Aty & Tillmanns, 2010). In such cases,

[1] In fact there are 25 frames for every cine slice in our dataset, but for the purpose of maximizing figure display area we only include 24 phases here.

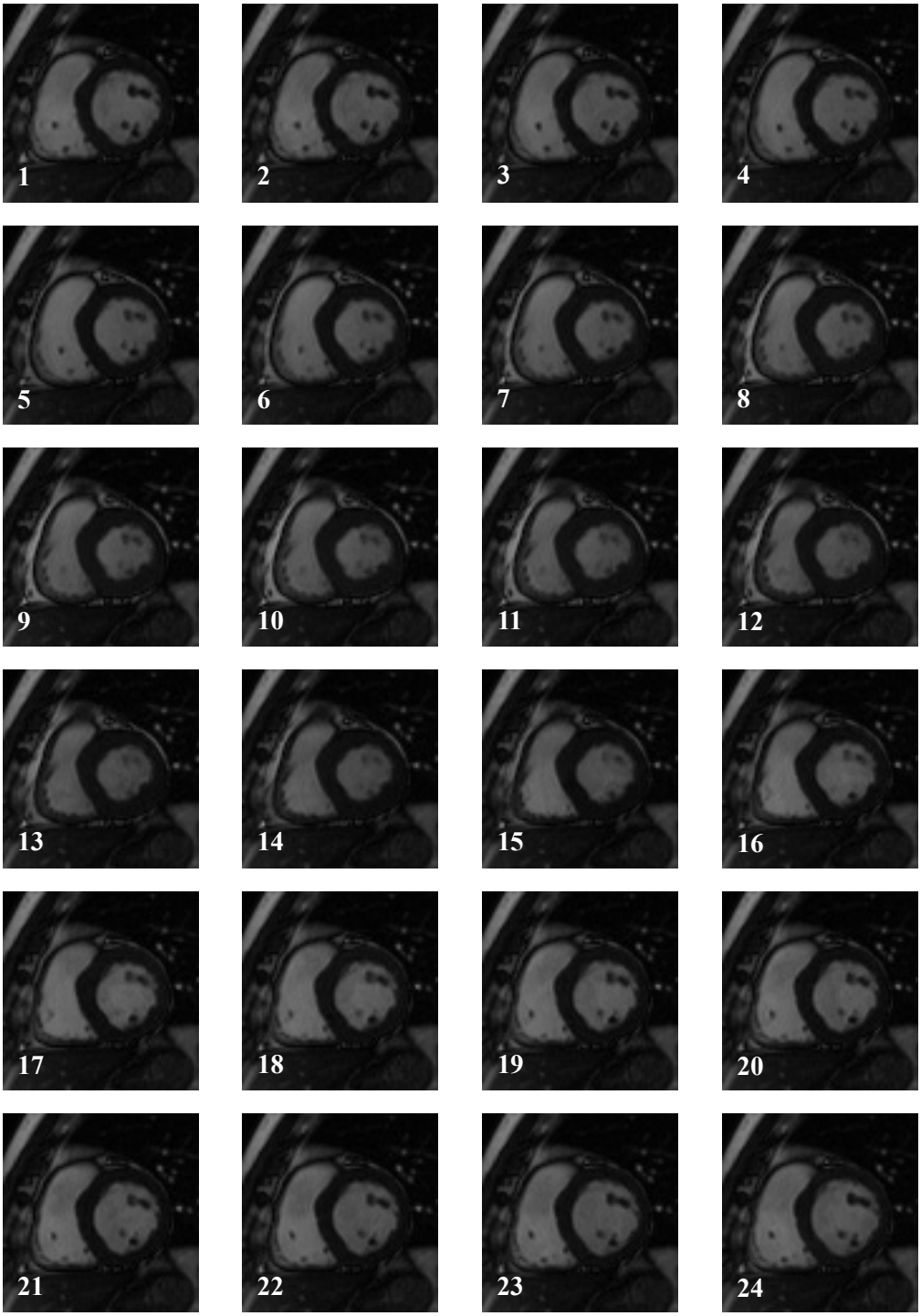

Figure 2.3: 24 frames of a mid-LV cine SA slice covering the entire cardiac cycle. The frame numbers are shown in the bottom left corner of each image.

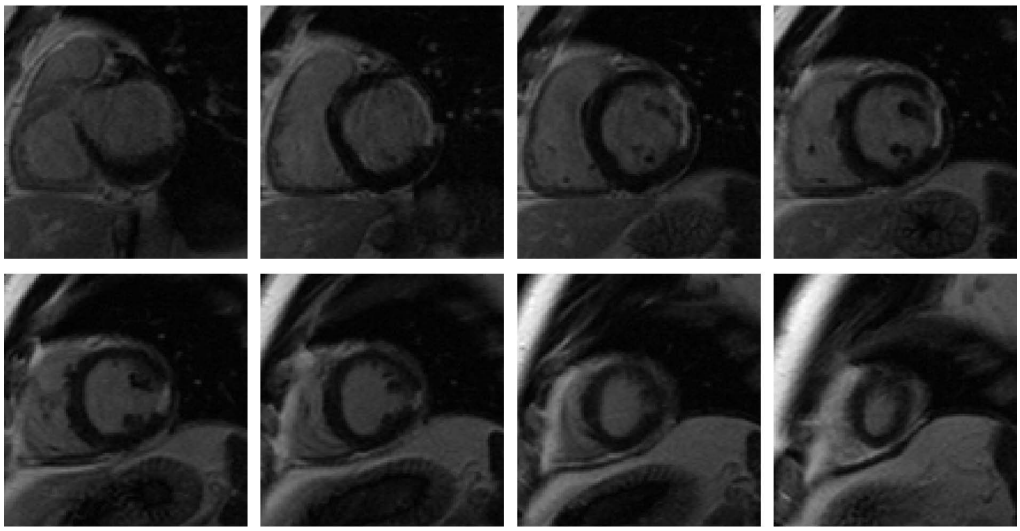

Figure 2.4: A stack of SA LGE images of a patient.

the involved *sub-endocardial* regions appear as dark as normal myocardium because no contrast agent can flow into these regions. Figure 1.1 shows an LGE image with a hyper-enhanced infarct and MVO.

Different from the cine sequence, an LGE sequence only scans one phase of the cardiac cycle – usually the mid-diastole. A stack of SA LGE images of a patient is shown in Fig. 2.4, while 4C and 2C LA LGE images of the same patient are shown in Fig. 2.5. As in cine images, the blood is bright and the myocardium is dark; but the contrast in LGE images is not as high as in cine images. A comparison of an SA LGE image with its corresponding cine image from the same patient is shown in Fig. 2.6; as we can see the myocardium looks similar except that in the LGE image the infarct is hyper-enhanced. Due to its ability to identify non-viable myocardium, LGE CMR is routinely performed by more and more cardiologists.

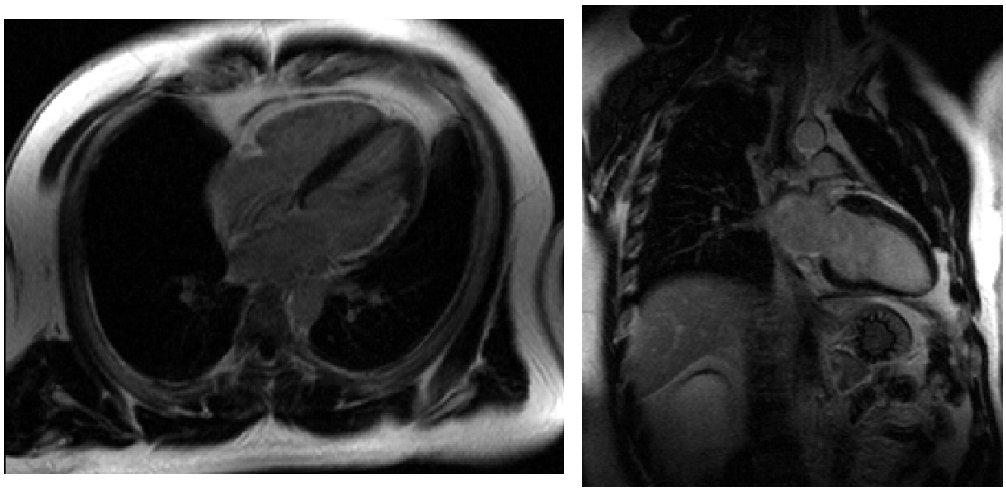

Figure 2.5: 4C (left) and 2C (right) LGE images from the same patient as in Fig. 2.4.

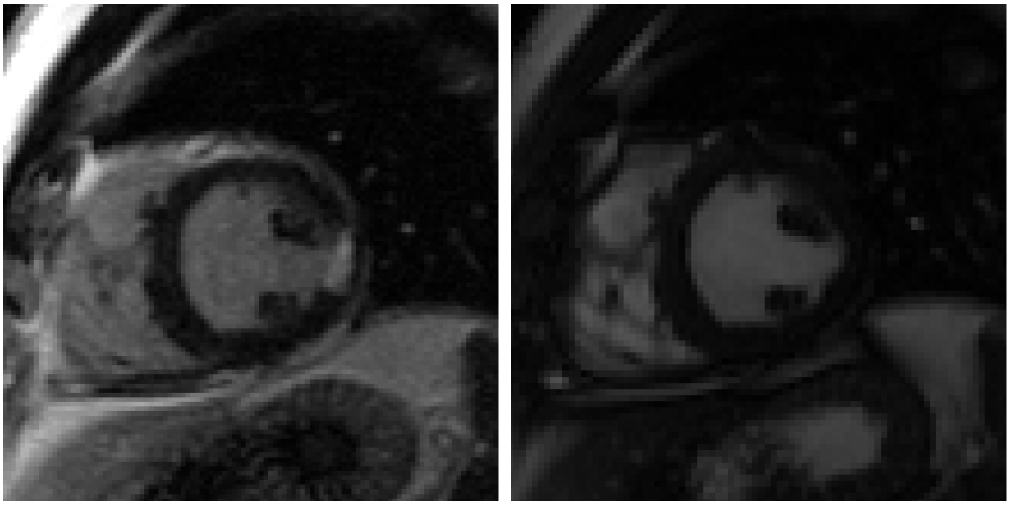

Figure 2.6: A pair of corresponding LGE (left) and cine (right) SA images.

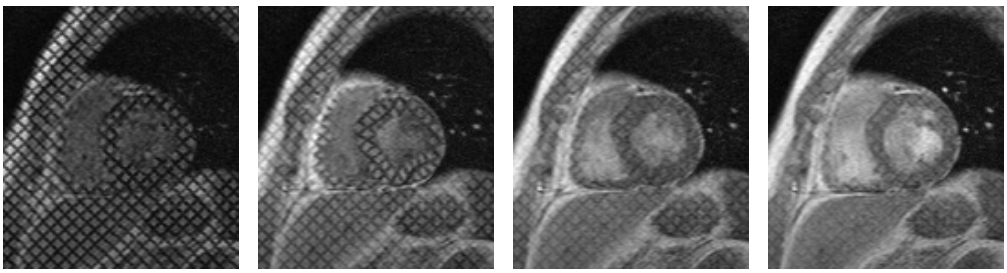

Figure 2.7: Four frames of a tagged SA slice that are evenly distributed in the R-R interval. Fading of the tag pattern is obvious.

2.2.4 Tagged CMR

Tagged CMR uses a special pulse sequence (SPAMM: SPAtial Modulation of Magnetization) to create temporary features – tags in the myocardium, which deform together with the myocardium as the heart beats and are captured in the multi-framed tagged CMR images (Zerhouni *et al.*, 1988). Figure 2.7 shows four frames of a tagged SA slice that are evenly distributed in the R-R interval. By tracking the tag pattern, motion of the myocardium can be quantitatively recovered. While tagged CMR is similar to cine CMR in that they are both dynamic images of the heart and thus both can provide information on myocardial motion, the difference is that tagged CMR provides direct and more accurate quantification of the regional heart motion and strain while cine CMR provides clearer anatomical structures. However, tagged CMR requires longer imaging times and hence often has fewer frames than cine CMR of similar quality and spatial resolution. The decoding of motion information carried by the tags also presents an overhead. Moveover, the tag pattern usually fades before an entire cardiac cycle can be imaged (which can be observed in Fig. 2.7), causing the motion recovery to be terminated early; occasionally the fading is even too fast to provide any useful motion tracking.

2.3 Standardized Myocardial Segmentation and Nomenclature

2.3.1 The Three Slice Levels and 17 Myocardial Segments

The American Heart Association (AHA) has recommended that the LV be divided into equal thirds perpendicular to the LA of the heart (Cerqueira *et al.*, 2002), which will generate three circular *basal*, *mid-cavity*, and *apical* SA slices of the LV. In CMR, usually there are more than three SA slices and they could be merged to create just three thick SA slices (e.g., Valindria *et al.*, 2011). The real apex which is beyond the apical SA slice can be evaluated from the 4C and 2C LA views. Further, the LV myocardium is divided into 17 segments for standardization (Fig. 2.8). With respect to the circumferential location, the basal and mid-cavity SA slices are divided into six segments of 60° each. The attachment of the right ventricular wall to the LV is used to identify and separate the septum from the LV anterior and inferior free walls. The apical SA slice is divided into fewer, i.e., four segments. Therefore, 16 segments are prescribed in the three SA slices. Lastly, the 17^{th} segment is extracted from the true apex in the 4C and 2C views.

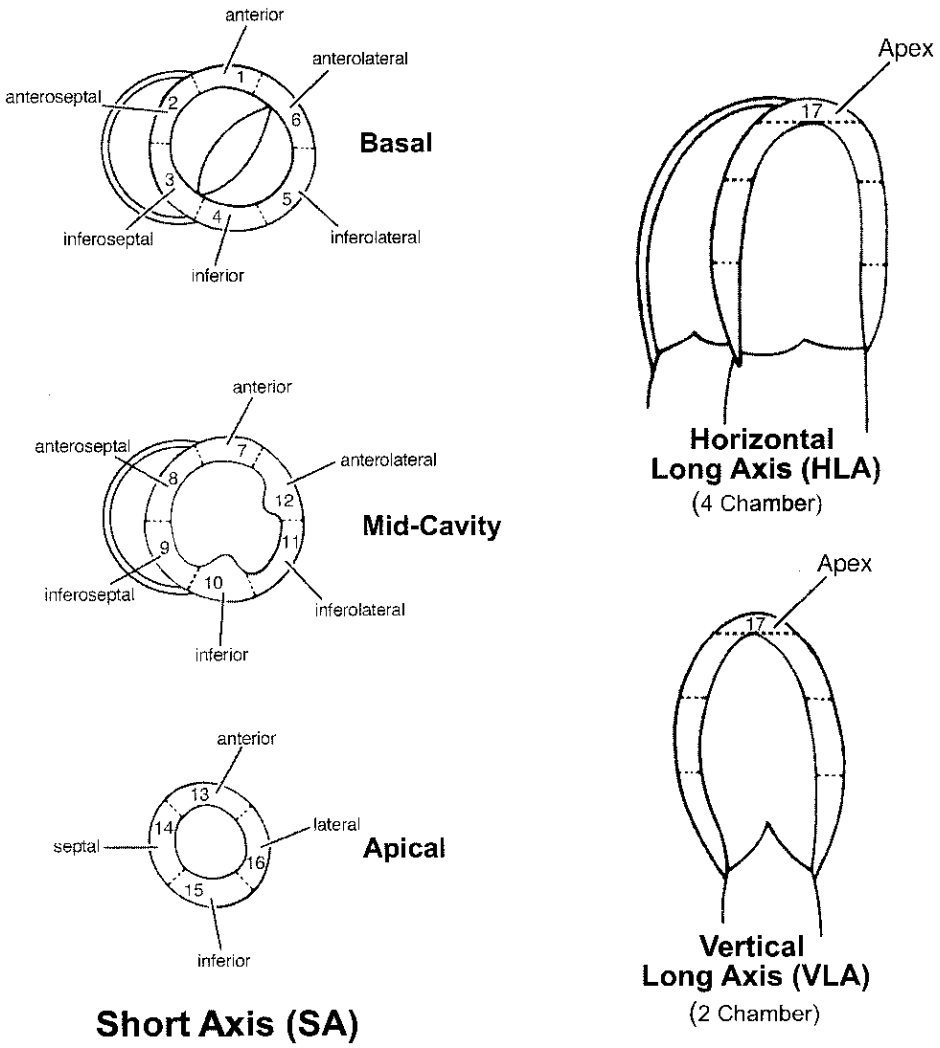

Figure 2.8: Left: the basal, mid-cavity and apical SA slices; right: the 4C and 2C LA views. IDs of the 17-segment model recommended by the AHA are overlaid locally. This figure originated from (Cerqueira *et al.*, 2002).

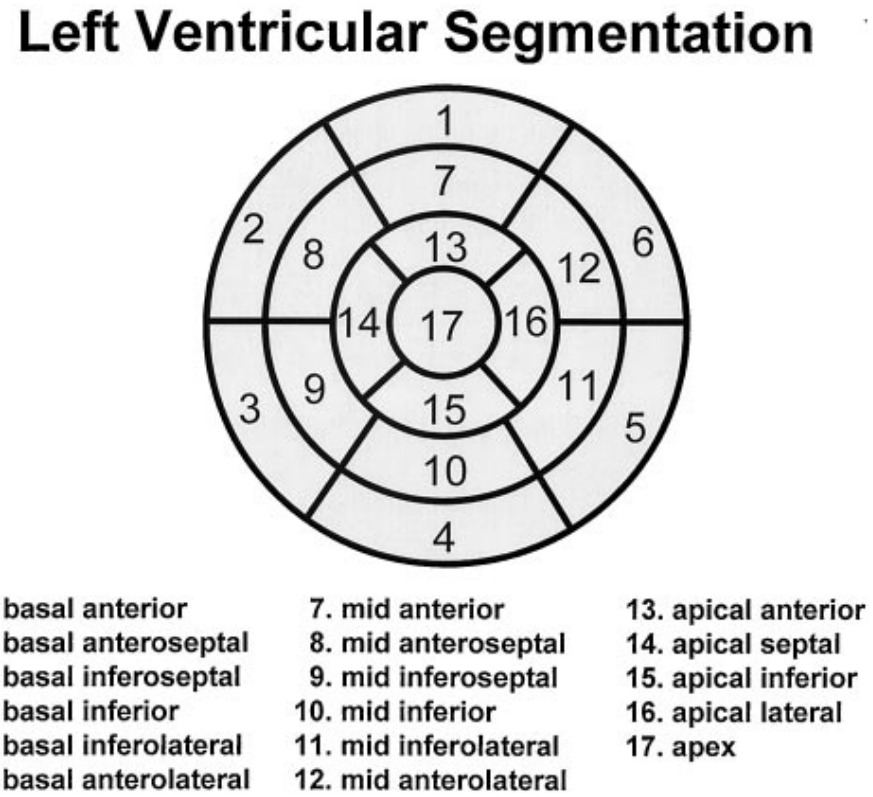

Figure 2.9: The bull's-eye plot of the AHA-recommended 17 myocardial segments. Also shown below the plot are the recommended nomenclature for the segments. This figure originated from (Cerqueira *et al.*, 2002).

2.3.2 Nomenclature

Figure 2.9 shows the location and AHA-recommended nomenclature for the 17 myocardial segments using a bull's-eye plot. The adjectives basal, mid and apical are used to indicate the location along the LA of the LV. The circumferential locations of the 6×2 segments on the basal and mid-cavity SA slices are indicated by *anterior, anteroseptal, inferoseptal, inferior, inferolateral* and *anterolateral*, and those of the 4 segments on the apical SA slice are indicated by *anterior, septal, inferior* and *lateral*. The 17^{th} segment from the LA slices is simply called the *apex*.

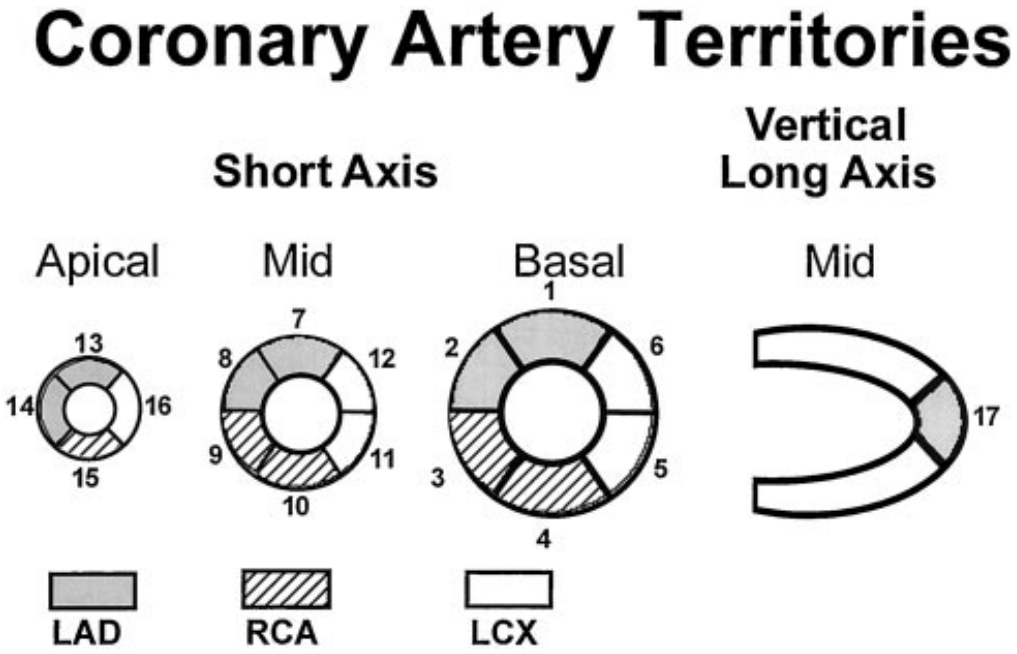

Figure 2.10: The general assignment of the 17 myocardial segments to the coronary artery territories. LAD: left anterior descending; RCA: right coronary artery; LCX: left circumflex. This figure originated from (Cerqueira *et al.*, 2002).

2.3.3 Assignment of Segments to Coronary Artery Territories

The AHA has also recommended the general assignment of the 17 myocardial segments to one of the 3 major coronary arteries, with the precaution that the variability in the coronary artery blood supply to myocardial segments is enormous. The assignment is shown in Fig. 2.10. Segments 1, 2, 7, 8, 13, 14, and 17 are assigned to the left anterior descending (LAD) coronary artery distribution. Segments 3, 4, 9, 10, and 15 are assigned to the right coronary artery (RCA) when it is dominant. Segments 5, 6, 11, 12, and 16 generally are assigned to the left circumflex (LCX) artery.

2.3.4 The 16-Segment Model for LGE CMR Quantification

Since the 17^{th} segment, which is extracted from the apex in 4C and 2C LA views, is rarely used for infarct quantification by cardiologists in LGE CMR studies, only the 1^{st}-16^{th} segments (denoted by Seg_{1-16}) extracted from SA views are studied in this thesis.

2.4 Spatial and Intensity Distortions

A set of LGE SA images often suffer from both spatial and intensity distortions, that is, misalignment artifacts and intensity inconsistency across images, respectively.

2.4.1 Misalignment Artifacts

Misalignment artifacts are common for multi-slice CMR data. Clinically, a few consecutive SA slices and 1-3 standard LA slices are acquired. Depending on different imaging protocols, each slice can be multi-framed (e.g., cine) or single-framed (e.g., LGE). Slices are usually acquired in multiple breath-holds, introducing differences in lung volume which in turn cause displacement of the heart (McLeish *et al.*, 2002). Misalignment artifacts can also be caused by patient motion and heartbeat; the former can be considered similar to the breath-related artifacts, while the latter is often neglected due to the use of ECG gating. Misalignment artifacts cause slices to move away from their true positions relative to each other (Fig. 2.11) and, if not tackled, may lead to distortion of the 3D reconstruction from the multi-slice data.

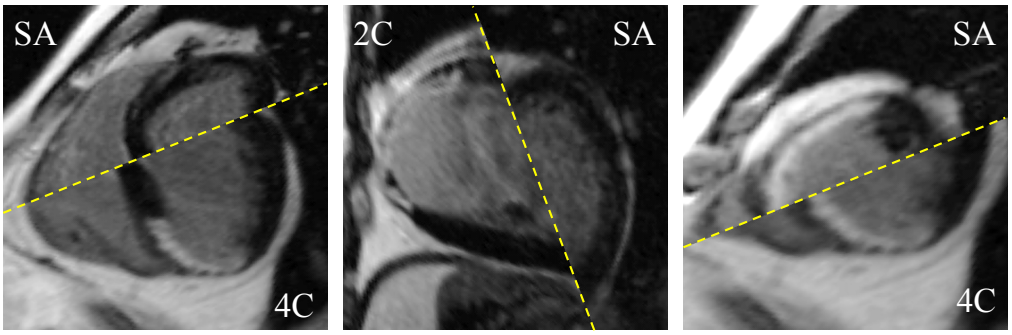

Figure 2.11: Misalignment artifacts illustrated with intersections between SA and LA slices.

Over the past decades, various approaches have been proposed to realign a set of CMR slices. Hennemuth *et al.* (2008) registered LGE slices to a whole-heart coronary angiography volume slice by slice by maximizing similarity measures in the overlapping image parts. However, the high resolution whole-heart volume data is not widely available under clinical settings. Lötjönen *et al.* (2004) and Barajas *et al.* (2006) proposed methods more suitable for clinically acquired CMR data, where slices were realigned by maximizing normalized mutual information (NMI) of the intersecting parts between slices. However, no regularization term was included to avoid unrealistic movements. Recently, Elen *et al.* (2010) introduced an effective regularization term favoring original spacing among SA slices, but its underlying assumption that the original spacing be correct is sometimes broken by superior-inferior motion of the heart. A common deficiency of (Barajas *et al.*, 2006; Elen *et al.*, 2010; Lötjönen *et al.*, 2004) is that they merely used similarity at the intersections between slices but ignored the anatomical continuity of the heart within the stack of SA slices. Furthermore, they all worked with multi-frame slices. As LGE data is single-frame, the available information that can be used for its realignment is $N_{\mathrm{f}} - 1$

times fewer, where N_{f} is the number of available frames.

2.4.2 Intensity Inconsistency

Signal intensities may vary from one LGE image to another even in the same dataset due to different time delays after injection of the contrast agent. A usual pattern is that the intensities tend to become brighter from the mitral valve to the apex (Fig. 2.12). This inconsistency cause the intensities of infarcts and normal myocardium in different slices to be different. Therefore, for any infarct classification method that is based on multiple slices, normalization of the intensity across slices is necessary. However, very few works in the literature explicitly handled this issue. To the best of our knowledge, the work by Valindria *et al.* (2011) was the only one that did so. The authors adjusted the intensity of each slice to the same range as in the first slice. Although doing so can make the overall intensity characteristics of the entire images more consistent, it does not necessarily normalize the intensities of the LV, which is the real target but only occupies a relatively small area in each image.

2.5 Myocardium Segmentation

The delineation of myocardial contours is a prerequisite to subsequent automatic localization and quantification of infarcts – nearly all such works (Elagouni *et al.*, 2010; Hennemuth *et al.*, 2008; Kolipaka *et al.*, 2005; Tao *et al.*, 2010; Valindria *et al.*, 2011) in the literature assume that high quality myocardium segmentation is given, either manually or (semi-) automatically. Since manual delineation is not only time-consuming but also subject to inter-observer

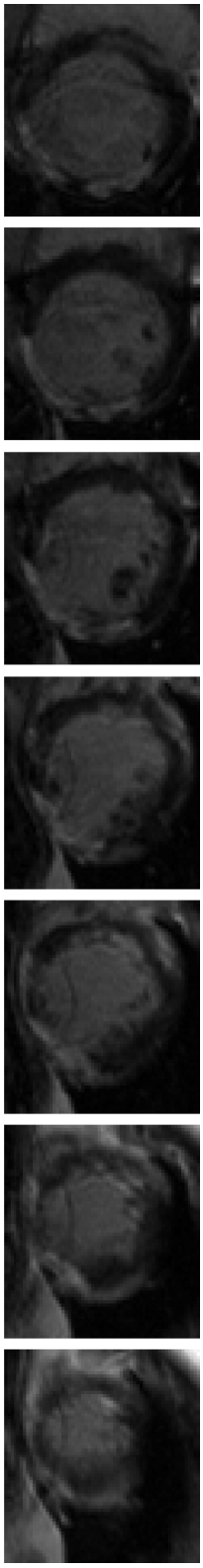

Figure 2.12: Illustration of the intensity inconsistency with a stack of SA LGE images from one dataset. The images become brighter from the mitral valve to the apex.

variability, it is highly desirable to automate the process. However, the automation is usually difficult due to the intensity heterogeneity of the myocardium and intensity similarity between the infarcts and BP. To the best of our knowledge, there has been little research aimed at fully automatic myocardial segmentation in LGE images, and there is no commercially or publicly available automatic segmentation tool for clinical use. Most existing approaches utilize pre-delineated myocardial contours in cine CMR data of the same patient as *a priori* knowledge (Ciofolo *et al.*, 2008; Dikici *et al.*, 2004). Such an approach is reasonable because the cine data, as the most frequently analyzed CMR data, is always acquired for a patient who is asked to remain still during the entire acquisition process. This approach has two important advantages. First, the pre-delineated LV in the cine data provides *a priori* knowledge about the shape and appearance of the LV in the LGE data, making the automatic segmentation more reliable, especially when the contrast between the BP and infarcts is poor. Second, many methods have been proposed for (semi-)automatic segmentation of the cine data (Chen *et al.*, 2008; Hautvast *et al.*, 2006; Li *et al.*, 2009, to name a few), and hence the entire process can be automated. Nevertheless, the major difficulties of this approach include: (i) displacement and nonrigid deformation between the cine and LGE data due to respiratory and body motion and inaccurate ECG gating; and (ii) different intensity characteristics of the cine and LGE data.

In one of the pioneering works on automatic segmentation of LGE images, Dikici *et al.* (2004) proposed to obtain *a priori* segmentation for the target LGE image by nonrigid registration of two nearby cine frames as well as of corresponding cine and LGE images, and then deform the *a priori* segmentation with

a five-parameter affine transformation by maximizing the probability of correct segmentation. Although elastic deformation of the LV between the *a priori* segmentation and its actual shape in the LGE image was partly compensated for by interpolating the deformation field between the two nearby cine frames, residual deformation may still remain because: (i) the ECG gating is inherently imperfect; and (ii) the interpolation of the deformation field is linear, while the deformation of the heart is known to be nonrigid. Consequently, a global affine transformation is inadequate to capture shape changes of the myocardium.

More recently, Ciofolo *et al.* (2008) proposed to first initialize and deform 2D myocardial contours according to image evidence in LGE images. The myocardium was divided into four quadrants and those likely to contain large areas of infarcts were treated differently. Subsequently, the 3D meshes that were preconstructed from cine images were registered towards the stack of contours from LGE images. It was novel to treat potential infarcts differently for the segmentation, but the division into four quadrants was too coarse to account for small infarcts. In addition, there was no correction of misalignment artifacts. McLeish *et al.* (2002) studied the motion of the heart due to respiration and found considerable displacements that should not be neglected. For a 3D mesh representation of the LV, there is a high risk of the original physical shape being distorted if the misalignment of slices is not corrected. Finally, shared information between the LGE and cine data was not fully utilized – although the shared geometric information was used via registration of the 3D meshes and the stack of 2D contours, the shared intensity information was unused.

In our previous work (Wei *et al.*, 2011), we presented an automatic segmentation method that fully utilizes shared information between corresponding cine

and LGE images. Given myocardial contours in cine images, the segmentation of LGE images was achieved in a coarse-to-fine manner. Affine registration was first performed between the corresponding cine and LGE image pair, followed by nonrigid registration, and finally local deformation of myocardial contours driven by forces derived from local features of the LGE image. At the stage of local deformation, we proposed an adaptive detection of endocardial edges by selecting one of the two cases – normal endocardium and sub-endocardial infarcts – and also included an effective thickness constraint into the evolution scheme. Despite its fairly good performance in the preliminary experiments, this method had the following drawbacks: (i) SA images were segmented individually in 2D without utilizing the inherent 3D information; (ii) the b-spline based nonrigid registration was slow; and (iii) the adaptive detection of infarcted and healthy myocardial edges was primitive.

2.6 Infarct Classification

Once the myocardium has been segmented, the next step is to classify it into infarcted and normal regions (or in other words, to segment infarcts from the normal myocardium). There are much more works on infarct classification than on myocardium segmentation, probably because this step is relatively easier.

Early works on infarct classification were purely intensity based with a global threshold, e.g., (Amado *et al.*, 2004; Kolipaka *et al.*, 2005). These methods suffer from the lack of spatial continuity, resulting in spatially separate false positives due to noise or artifacts. To overcome this problem, Hsu *et al.* (2006a,b) proposed the feature analysis and combined thresholding method, which en-

forces spatial constraints by assuming that the infarcts are generally sub-endocardial and reasonably large. Recent works applied more advanced techniques to this problem. Heiberg *et al.* (2005) proposed a level set algorithm to regularize the thresholding and exclude small regions that constitute noise rather than infarction. Similarly, Metwally *et al.* (2010) proposed to enhance the thresholding using k-means clustering. In (Hennemuth *et al.*, 2008) and (Elagouni *et al.*, 2010), advanced signal intensity analysis is carried out based on the Rician distribution of noisy MRI data (Gudbjartsson & Patz, 1995), where the myocardium is modeled with a mixture model comprising a Rayleigh distribution for normal myocardium plus a Gaussian for infarcts. However, these methods are generally 2D and hence do not take advantage of 3D spatial and intensity continuity.

Recently, Tao *et al.* (2010) proposed a method which first globally thresholds the image followed by false-positive and false-negative removal combining intensity and spatial information. The method has three novelties: (i) The LV BP is included as the same class as the infarcts during classification. (ii) All SA slices of a patient are used together in the intensity distribution analysis to derive the global threshold. This strategy works effectively when there is no obvious intensity inconsistency in a set of LGE images but *degenerates* in the presence of significant intensity inconsistency. (iii) The Otsu threshold (Otsu, 1979) which maximizes the ratio of between-class and within-class variances is adopted, so there is no need to make any assumption regarding the underlying true distribution. Nevertheless, this work suffers from two drawbacks: there is neither correction for intensity inconsistency nor correction for misalignment artifacts across slices, and it is still based on a global threshold.

Instead of adopting the popular Rician model, Valindria *et al.* (2011) pro-

posed to use a mixture model of two Gaussian distributions. A global threshold is determined as the mean of the two Gaussian centers. Similar to (Tao *et al.*, 2010), post-processing based on connected component analysis (Gonzalez & Woods, 2008) is conducted to remove false-positives. It is the only work in the literature that handled both misalignment artifacts and intensity inconsistency. SA slices are realigned by aligning myocardial centers of all slices in a line; however, this is not always correct since anatomically the slices' myocardial centers do not necessarily form a line. The intensity of each slice is adjusted to the same range as in the first slice. Although doing so can make the overall intensity characteristics of the entire images more consistent, it does not necessarily normalize the intensities of the LV, which despite being the real target only occupies a relatively small area in each image. Another drawback of this work is that again global thresholding is performed as the major classification process.

2.7 Joint Analysis with Other Types of CMR

LGE CMR provides direct visualization of non-viable myocardium with hyper-enhanced intensities. When LGE CMR is combined with cardiac scans that reveal information on myocardial perfusion or contraction, regions of the myocardium that are dysfunctional but not hyper-enhanced in LGE CMR images can be identified. This type of dysfunctional myocardium has the potential to resume its normal functionality if re-vascularised and hence is called *hibernating* myocardium (Rahimtoola, 1989). Usually doctors identify dysfunctional myocardium by detecting perfusion defects and / or abnormal contractibilities. In

CMR, the former is always examined by perfusion sequences while the latter can be examined by cine and tagged sequences. Although cardiologists routinely jointly inspect the three kinds of images (perfusion, contracting and LGE) side by side with the delicate correlations in mind, it is technically difficult to correlate corresponding regions across images of different protocols via computer vision. Major difficulties come from the differences in imaging planes, cardiac phases and intensity characteristics of the different types of CMR images.

Perfusion CMR images the first pass of the contrast agent through the myocardium after bolus injection. Blood perfusion defects (i.e., ischemia) can be identified by observing temporal intensity changes of the myocardium. The frames of a perfusion sequence are triggered at the same phase of multiple cardiac cycles, therefore they are not supposed to contain any myocardium motion. Meanwhile, a perfusion sequence contains much fewer slices (usually 3-4 slices) than the cine and LGE sequences. Hennemuth *et al.* (2008) investigated the joint inspection of LGE and perfusion CMR data and showed that it can yield clinically useful information. A similar approach was proposed earlier in (Breeuwer *et al.*, 2003) with a less sophisticated visualization scheme. However, due to the sparsity of the perfusion data as compared to the LGE data, a large portion of the LGE slices do not have an exact location match in the perfusion data for an accurate reference of regional perfusion status.

In contrast, cine CMR has comparable slice density to LGE CMR and shows dynamics of the myocardium in addition to the heart anatomy. Noble *et al.* (2004) fused infarct transmurality information derived from LGE images with wall thickening information derived from cine images via image registration and suggested candidate areas for re-vascularisation with the fused bull's-eye plot.

Recently, Liu *et al.* (2011) developed dedicated algorithms to propagate suspicious infarcts identified in LGE images to cine images of all cardiac phases. Different non-rigid registration techniques were proposed and employed for the temporal registration of cine frames and cross-protocol registration of LGE and cine images, respectively. Hyper-enhanced regions identified in LGE images were correlated with regional wall motion abnormalities derived from cine images. Despite providing accurate myocardial wall measurements such as the thickness, cine CMR is not suitable for extraction of accurate strain tensors of the myocardium due to the absence of distinctive landmarks within the myocardium (Axel *et al.*, 2005; Makela *et al.*, 2002).

Tagged CMR also has comparable slice density to LGE CMR and can provide accurate myocardial strain tensors. Although joint analysis of patient LGE and tagged CMR seems promising, research works that actually did so (Inoue *et al.*, 2010; Ryf *et al.*, 2006) are rare in the literature probably because of the dual burden of (i) processing both kinds of data and (ii) matching them with necessary accuracy. The workload is laborious if the analysis is done manually; otherwise, sophisticated algorithms able to handle both kinds of data are needed. Compared with the techniques proposed in this thesis, the analysis of the LGE data in both cited previous works (Inoue *et al.*, 2010; Ryf *et al.*, 2006) on joint analysis of the LGE and tagged CMR was rather primitive.

Chapter 3

Correction of Spatial and Intensity Distortions

This chapter describes how we pre-process LGE CMR datasets to eliminate or at least greatly reduce spatial and intensity distortions, before they can be processed in 3D. Section 3.1 presents our method for the correction of the spatial distortion – misalignment artifacts across slices of a set of LGE data. Section 3.2 presents our method for the correction of the intensity distortion – inconsistent intensities across slices.

3.1 Misalignment Correction of Clinical CMR Data

As introduced in Section 2.4.1, misalignment artifacts are common for multi-slice CMR data and, if not tackled, may lead to distortion of the 3D reconstruction from the multi-slice data. In this section, we propose an effective and robust method for misalignment correction of both multi-framed (such as the cine) and

single-framed (such as the LGE) clinical CMR data. Unlike previous methods which merely rely on similarity measurement at intersections of slices, we propose to also utilize the innate physical continuity of the heart throughout the SA stack to establish interlinks within the SA slices and group them together. This is achieved by introducing a novel cost term, namely, the contiguous cost, between adjacent SA slices. The contiguous cost not only prevents unrealistic movement of the slices, but also improves the accuracy of the misalignment correction.

Since misalignment correction is not the major focus of this thesis but an auxiliary (though critical) step, we did not include a comprehensive evaluation of the proposed correction method. Instead, a preliminary evaluation should be sufficient to demonstrate its effectiveness. The preliminary experimental results on both real patient and simulated data show that our method can robustly eliminate or reduce misalignment artifacts even with single-framed data, and the comparative study with simulated data further demonstrates that the contiguous cost can significantly improve the accuracy of the misalignment correction.

The rest of this section is organized as follows. Section 3.1.1 describes the proposed method. Section 3.1.2 presents the experimental results on both real patient and simulated data, followed by the discussion in Section 3.1.3. Section 3.1.4 concludes this section.

3.1.1 Method

Since frames of a single slice are always scanned in a single breath-hold, there should be no breathing-related misalignment among them. If we further assume

that there is no significant patient motion during the breath-hold, all frames of the same slice should share the same position (Barajas *et al.*, 2006; Elen *et al.*, 2010; Lötjönen *et al.*, 2004). Therefore, with multi-framed data there is $N_{\mathrm{f}} - 1$ times more information for misalignment correction than with single-framed data (where N_{f} is the number of available frames), and the correction is made much easier. Meanwhile, as more frames simply mean an augmentation of available information, it is trivial for a method that works for single-framed data to support multi-framed data. As we require our method to be capable of being applied to single-framed data such as LGE data, in addition to the multi-framed, and need to test its robustness with such data, we will present the method only with single-framed datasets[1].

In our method, we incorporate only translational but no rotational correction based on two research findings: (i) a study on motion and deformation of the heart due to respiration found only very small rotations (typically a couple of degrees) (McLeish *et al.*, 2002), and (ii) in another study (Elen *et al.*, 2010), a method capable of full 3D translational and rotational corrections found no significant improvement on final results with the rotational correction.

3.1.1.1 Intersecting cost

The intersecting cost refers to the dissimilarity measure along the intersecting line between a pair of intersecting slices. Assume there are m SA and n LA slices (denoted by I^k_{SA} and I^j_{LA}, where $k \in [1, m]$ and $j \in [1, n]$). The position and orientation of a slice in the patient coordinate system are uniquely defined

[1]Even for 4D data we will only use the single frame at the mid-diastole phase, which is the scan phase of our LGE data.

by two fields of the standard DICOM header – ImagePositionPatient (IPP) and ImageOrientationPatient (IOP), respectively. Given IPP and IOP of two slices, their intersection line can be computed. Then, two line segments are sampled along the intersection line on both slices (Figs. 3.1 (a) and (b)). The smaller PixelSpacing (PS, from the DICOM header) of the two slices' is used as the step size during sampling with linear interpolation. Finally, the intersecting cost between the two slices is defined as the dissimilarity measure of the two sampled line segments:

$$E_{\text{int}} = \begin{cases} E_{\text{int}}(I^k_{\text{SA}} \bigcap I^j_{\text{LA}}) = \mathscr{C}_{\boldsymbol{s}}(\boldsymbol{s}^k_{\text{SA}}, \boldsymbol{s}^j_{\text{LA}}), \\ E_{\text{int}}(I^j_{\text{LA}} \bigcap I^{j'}_{\text{LA}}) = \mathscr{C}_{\boldsymbol{s}}(\boldsymbol{s}^j_{\text{LA}}, \boldsymbol{s}^{j'}_{\text{LA}}), \end{cases} \tag{3.1}$$

where $I^k_{\text{SA}} \bigcap I^j_{\text{LA}}$ denotes the intersection between the k^{th} SA and j^{th} LA slices, and $I^j_{\text{LA}} \bigcap I^{j'}_{\text{LA}}$ the intersection between the j^{th} and j'^{th} LA slices ($j \neq j'$), $\boldsymbol{s}^k_{\text{SA}}$ and $\boldsymbol{s}^j_{\text{LA}}$ the sampled line segments on SA and LA slices respectively, and $\mathscr{C}_{\boldsymbol{s}}$ a function measuring dissimilarity between two line segments.

$\boldsymbol{s}^k_{\text{SA}}$ and $\boldsymbol{s}^j_{\text{LA}}$ depend on IPP, IOP and PS of the two intersecting slices. Of the three, IOP and PS can be considered constants as neither is changed by our method. Consequently, E_{int} is actually a function of IPP. Particularly, IPP of a slice stores the x, y and z coordinates of the slice in the patient coordinate system. Thus, translation of a slice can be achieved conveniently by changing its IPP. As we are only interested in the LV, only a fraction of the intersection line between SA and LA slices is sampled to form $\boldsymbol{s}^k_{\text{SA}}$ and $\boldsymbol{s}^j_{\text{LA}}$. The sampling range is confined within a region of interest (ROI) on each SA slice, which is predefined by identifying a bounding box that well contains the LV. Only

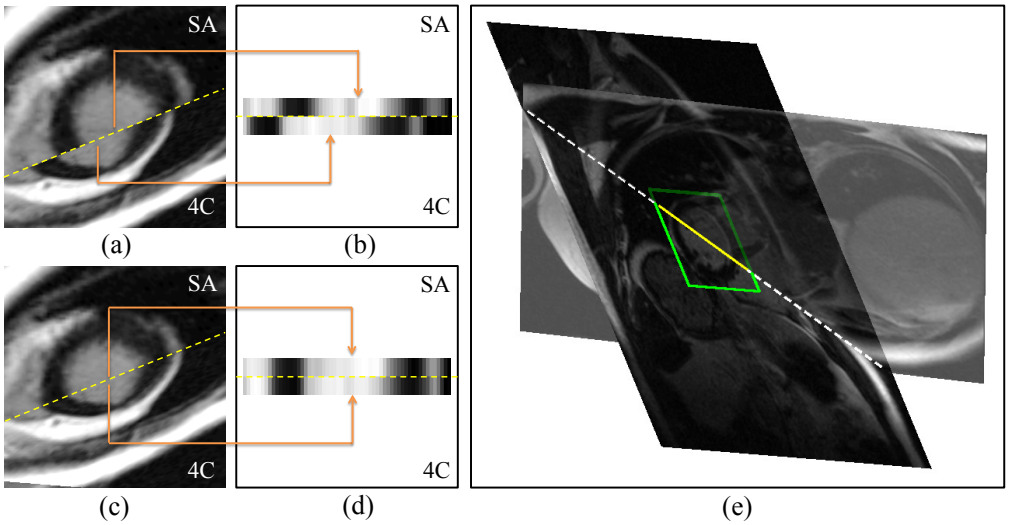

Figure 3.1: Illustration of the intersecting cost. (a)-(b) The intersecting part between an SA and a 4C slice before misalignment correction. (c)-(d) The same intersecting part after misalignment correction. (e) $\boldsymbol{l}^i_{\mathrm{SA}}$ and $\boldsymbol{l}^j_{\mathrm{LA}}$ are sampled along the intersection (dashed white) line only from the portion (yellow segment) lying within the SA slice's ROI (green rectangle).

the portion lying within the ROI is sampled (Fig. 3.1 (e)). However, for the intersection line between different LA slices, the entire length is sampled to form $\boldsymbol{s}^j_{\mathrm{LA}}$ and $\boldsymbol{s}^{j'}_{\mathrm{LA}}$. This is because if only the portion within the LV is sampled, there would be too little discriminative information (mostly from the BP) to determine relative positions of the LA slices.

3.1.1.2 Contiguous cost

The contiguous cost refers to the discontinuity measure between two adjacent SA slices. The LV is naturally smooth, and hence its representation throughout the stack of SA slices should be continuous[1]. Although the continuity of the LV

[1] Although there could sometimes be a gap between adjacent SA slices in clinical CMR data, this gap is always small enough to obtain a correct 3D representation of the LV, and thus the smoothness of the LV is retained.

throughout the SA stack is an important physical property, it has been ignored by previous works. We define the discontinuity measure between contiguous SA slices as the contiguous cost (as opposed to the intersecting cost). The contiguous cost is combined with the already defined intersecting cost to form the total cost to be minimized. On one hand, the contiguous cost acts as a regularization to the intersecting cost, preventing it from pushing slices to unrealistic locations; on the other hand, it can also improve the correction accuracy since it is derived from a strong physical property of the LV anatomy.

The discontinuity is measured by the dissimilarity between two regions of the same area sampled from adjacent SA slices. Although the LV appears different in adjacent slices due to different imaging locations, the change is gradual. Therefore, by minimizing the dissimilarity via translation of slices, the original relative positions of the SA slices can be recovered. Again the ROI is predefined for each SA slice. However, since the ROI is defined as the bounding box which well contains the LV, its size is varied for most SA slices as the LV size varies in most SA slices; furthermore, during the translation, SA slices are deviated from each other, and so are their ROIs. To solve this problem, we project the two ROIs of adjacent SA slices onto a middle plane and find the smallest rectangle which can completely contain the two projections on that plane, and then project this rectangle back onto the SA slices under consideration to determine the regions used for the discontinuity measure (Fig. 3.2). Noting that the projections are all along the normal to the SA planes, these procedures are actually finding the smallest cuboid whose top and bottom faces are in the SA slices (planes) under consideration and can completely contain the corresponding ROI in each slice. Denoting the two regions sampled from the two adjacent SA slices by

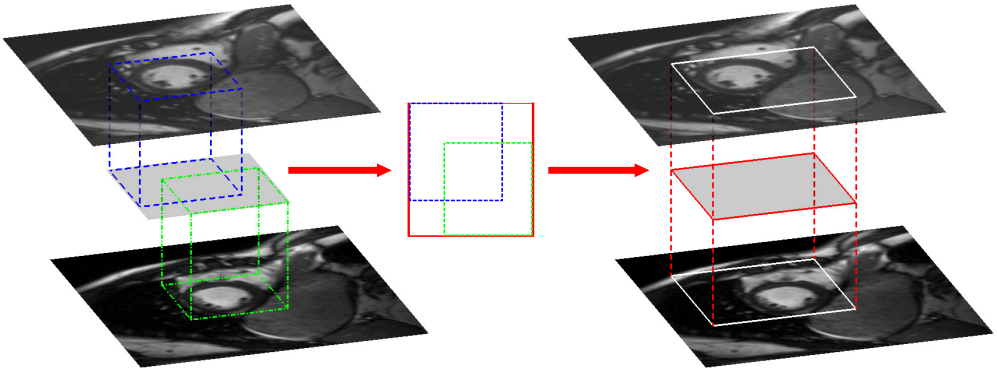

Figure 3.2: Illustration of the contiguous cost: the regions (white rectangles) in which R_{SA}^{k} and R_{SA}^{k+1} are sampled are defined by finding the smallest cuboid whose top and bottom faces are in the involved SA slices (planes) and can completely contain the corresponding ROI (dashed blue and green) in each slice. Distance between contiguous SA slices is exaggerated here for better visualization.

R_{SA}^{k} and R_{SA}^{k+1}, the contiguous cost is defined as:

$$E_{\mathrm{cnt}}(I_{\mathrm{SA}}^{i} \parallel I_{\mathrm{SA}}^{i+1}) = \mathscr{C}_R(R_{\mathrm{SA}}^{i}, R_{\mathrm{SA}}^{i+1}),\ i \in [1, m-1], \tag{3.2}$$

where $I_{\mathrm{SA}}^{k} \parallel I_{\mathrm{SA}}^{k+1}$ denotes the adjacency of two consecutive SA slices, and $\mathscr{C}_R$ is a function measuring dissimilarity between two regions.

E_{cnt} is also a function of IPP, as the regions sampled on adjacent SA slices are determined by their IPPs (plus the constants IOP and PS). Furthermore, because the translation of slices takes place in the patient coordinate system (instead of any of those coinciding with the SA plane), E_{cnt} is fully dependent on slices' translations in all x-, y-, and z- directions.

3.1.1.3 Total cost

The total cost is a summation of all the intersecting and contiguous costs. The intersecting cost is computed for all intersecting slices, including intersections

between SA and LA slices, and between different LA slices; each intersection is counted only once. The contiguous cost is computed for all pairs of adjacent SA slices; each adjacency is also counted only once. Now we can write the total cost as:

$$\begin{aligned} E_{\text{align}}(\mathit{IPP}_{\text{all}}) = &\sum_{i=1}^{m}\sum_{j=1}^{n} E_{\text{int}}(I_{\text{SA}}^{i} \cap I_{\text{LA}}^{j}) + \sum_{j=1}^{n-1}\sum_{j'=j+1}^{n} E_{\text{int}}(I_{\text{LA}}^{j} \cap I_{\text{LA}}^{j'}) \\ &+ \varepsilon \sum_{i=1}^{m-1} E_{\text{cnt}}(I_{\text{SA}}^{i} \parallel I_{\text{SA}}^{i+1}), \end{aligned} \tag{3.3}$$

where $\mathit{IPP}_{\text{all}} = \{\mathit{IPP}_{\text{SA}}^{k},\ \mathit{IPP}_{\text{LA}}^{j} \mid k \in [1,m], j \in [1,n]\}$ represents x, y, z coordinates of all slices under the patient coordinate system, and ε a weighting factor. E_{align} is minimized to find the optimal $\mathit{IPP}_{\text{all}}^{\text{opt}}$ set, which is the corrected positions of all the slices.

3.1.2 Preliminary Results

3.1.2.1 Data description and experimental settings

We have tested the proposed misalignment correction method on real patient cine and LGE data, as well as on simulated data. The real patient data were clinically acquired with ECG gating by a 1.5T Siemens Symphony MRI scanner from 10 patients who were diagnosed as having experienced myocardial infarction. The LGE data were acquired following a bolus injection of Gadolinium-based contrast agent. The in-plane isotropic pixel size ranges from 1.56-1.98 mm for the cine data and 1.17-1.56 mm for the LGE data. The slice thickness is 7 mm and there is a gap of 3 mm between contiguous SA slices for both kinds of data. The stack of SA slices covers the LV from the valve to the apex; based

on the individual heart size, there are 6-9 usable SA slices in a dataset. The standard 2C and 4C LA views were acquired. Although there are 25 frames for the cine data, we only select the frame corresponding to the mid-diastole phase. The simulated data will be described in Section 3.1.2.3 when we present the quantitative study.

For both $\mathscr{C}_{\boldsymbol{s}}$ and $\mathscr{C}_R$ we use the mean of squared differences (MSD). Noting that the intensities of the same structures may vary in different slices, the sampled $\boldsymbol{s}^k_{\mathrm{SA}}$, $\boldsymbol{s}^j_{\mathrm{LA}}$ and R^k_{SA} are pre-normalized to zero mean and unit standard deviation before being fed to $\mathscr{C}_{\boldsymbol{s}}$ and $\mathscr{C}_R$. The weighting factor ε is set to 0.01 empirically.

3.1.2.2 Qualitative study

For all the 10 sets of cine and LGE data, significant misalignment is observed in at least one SA slice via visual inspection of intersecting parts between SA and LA slices (see Figs. 3.3 a and c for example). After applying the proposed correction method, discrepancies at intersecting parts of the SA and LA slices are greatly reduced or even eliminated (Figs. 3.3 b, d and f), and the myocardium appears much more continuous and smoother in cross-sections of the SA stacks (Fig. 3.3 h). In addition, no unrealistic re-locating of slices (e.g., SA slices are deviated far away from central axis of the LV) is found. These qualitative results indicate that our misalignment correction method can effectively recover the original positions of the slices relative to each other. Besides, we also find that the method works better for cine data than for LGE data. This finding is not surprising: although the resolution of LGE data is higher, cine data has better contrast and more consistent brightness patterns across slices.

Figure 3.3: Exemplary results of our method. a-f: intersecting parts of slices before (upper row) and after applying our method. g-h: cross-section of a stack of SA slices before (upper row) and after applying our method. i-j: a comparison of the correction results without (upper row) and with E_{cnt} via cross-section of an SA stack. Data type: a, b, g, h – cine, the rest – LGE.

3.1.2.3 Quantitative study

The real patient data cannot be used for the quantitative study due to the lack of ground truth. To overcome this problem, we have generated two sets of simulated data from two cardiac CT volumes. With multi-slice technique, a cardiac CT volume can be deemed free of breathing-related misalignment artifacts; besides, CT data has much higher resolution than MRI. We have re-sampled the CT volumes to get two sets of conventional SA and LA slices which correspond to our clinical LGE data and visually examined the generated slices to ensure no distortion of the LV. The simulated data are used as *pseudo* ground truth and denoted by Sim_1 and Sim_2 respectively.

To simulate misalignment artifacts of clinical CMR data, each slice of the simulated data is deviated from the pseudo ground truth in all three axial directions with a different random variable for each direction. Then we apply our method to the purposely misaligned slices to recover the pseudo ground truth. Since almost all clinical analysis is performed with the stack of SA slices and LA slices are usually only for reference purposes, we focus on the errors of the recovered positions of SA slices only. As all slices are moved simultaneously and in fact it is the relative positions of slices that really matter, relative coordinates are used to quantify the errors. One problem of using relative coordinates is that the choice of the reference slice could introduce considerable bias, e.g., the selection of a badly replaced slice as reference will cause the error to be high even if the rest slices are correctly realigned. Therefore, we propose to calculate for each SA slice a misalignment error which is averaged from its displacement errors (in Euclidian distance) measured with every possible reference, i.e., ev-

ery SA slice in the dataset being used, including itself. Thus, the bias can be evened out effectively. In order to demonstrate the usefulness of the novel contiguous cost, we perform the misalignment correction both with and without the contiguous cost on the simulated data and compare the results.

The misalignment and recovery procedure is repeated 50 times for each dataset to produce statistically valid results. Consequently, $N = 50 \times m$ slices are used for the analysis of mean misalignment errors, where m is the number of SA slices in a dataset; since the misalignment and recovery procedure produces only one maximum error at each repeat, $N = 50$ measurements are used for the analysis of maximum misalignment errors. Furthermore, the study is conducted with random variables drawn from uniform distributions of three different ranges: [-3.5 3.5], [-5.25 5.25] and [-7.5 7.5] mm. The results are summarized in Table 3.1. We can see that both the mean and maximum misalignment errors are greatly reduced after correction; when the introduced misalignments are drawn from the more clinically practical [-3.5 3.5] mm range, our method achieves highly accurate corrections with mean residual misalignment errors smaller than 1.4 mm. This evidences the effectiveness of our method in recovering the slices' true relative positions. In addition, the inclusion of E_{cnt} reduces the mean / maximum residual errors for both datasets; standard deviations of the residual errors are reduced as well. This suggests that the proposed contiguous cost truly improves accuracy and robustness of the misalignment correction. Meanwhile, the improvement becomes more significant as magnitude of the misalignment increases.

Table 3.1: Mean and maximum misalignment errors (mm) of the simulated data before and after correction.

	No correction		Correction without E_{cnt}		Correction with E_{cnt}	
	mean	max	mean	max	mean	max
Sim_1	4.07±0.76	5.15±0.50	1.65±0.93	2.97±1.13	**1.38±0.80**	**2.57±0.95**
	6.02±1.12	7.55±0.89	2.69±1.52	4.84±2.12	**2.33±1.32**	**4.09±1.83**
	8.07±1.48	10.22±1.07	4.42±2.47	7.54±3.06	**3.62±2.10**	**6.26±2.94**
Sim_2	4.06±0.78	5.07±0.58	1.57±1.01	2.78±1.32	**1.36±0.86**	**2.48±1.15**
	5.99±1.15	7.50±0.95	2.78±1.65	4.81±2.08	**2.41±1.53**	**4.11±1.97**
	7.85±1.42	9.64±1.22	4.94±2.62	8.11±3.07	**4.00±2.16**	**6.77±2.64**

3.1.3 Discussion

One important reason for the improvement brought by the contiguous cost is that it establishes interlinks within the stack of SA slices and groups them together. When there is only the intersecting cost, each SA slice is only directly related with LA slices, yet isolated from other SA slices. In such a case, individual SA slices are susceptible to local minima of the intersecting cost and unable to escape once trapped. Figure 3.3 i shows an example, in which most of the SA slices are aligned reasonably well but the central one is trapped by a local minimum of the intersecting cost and far away from the rest. After the contiguous cost is incorporated, the introduced interlinks of the SA slices pull it out and further make the LV structure more continuous and smoother throughout the SA stack (Fig. 3.3 j). In this way, the misalignment errors are greatly reduced. Another reason could be that the contiguous cost in itself models a basic physical property of the subject being scanned, so it can improve the overall realignment once incorporated.

One potential limitation of our method is that the contiguous cost does not work for sparse SA slices, e.g., when there is only one slice for each of the basal, mid-cavity and apical levels of the LV. However, the method would still work for such cases by setting the weight for the contiguous cost $\varepsilon = 0$, in which case the method is purely intersection based and thus quite similar to (Lötjönen *et al.*, 2004). Fortunately, most LGE CMR data nowadays have SA slices with slice spacings smaller than 1 cm (unless otherwise intentionally scanned in a sparse way) and our method utilizes this advantageous feature when available. For future work, it would be interesting to study the impacts of different slice

spacings on the method.

3.1.4 Conclusion

In this section we present a robust method for the correction of misalignment artifacts in clinical multi-sliced CMR data. Unlike most preceding works which merely relied on the intersecting costs between slices, we propose to incorporate an extra novel cost term – contiguous cost – which utilizes the continuity of the imaged LV all through the stack of SA slices. Since the contiguous cost establishes interlinks among the once isolated SA slices and groups them together, our method can reduce the susceptibility of individual SA slices being trapped by local minima of the intersecting cost. The experimental results on real patient as well as simulated data have shown that by combining the proposed contiguous cost with the conventional intersecting cost, our method can produce high-quality correction even with single-framed data. The comparative study with the simulated data has further demonstrated that the inclusion of the contiguous cost can improve the accuracy of the misalignment correction.

3.2 Correction of Intensity Inconsistency

As introduced in Section 2.4.2, intensities of different slices in a set of LGE data can be inconsistent due to different time delays after the contrast agent injection. This inconsistency may cause false classification of infarcts as the infarcts are largely identified via intensities. In this section, we propose a novel method which only considers local regional intensities of the LV and thus can effectively eliminate or reduce the intensity inconsistency in the LV region. The

rationale underlying the proposed method is that the intensity of the BP should be roughly the same across slices. Assuming the myocardial contours are given, the BP region in each image can be simply obtained by masking the region enclosed by the endocardial contour. However, dark papillary muscles are also considered as BP pixels in this way. In order to normalize the BP and hence LV intensities more accurately, we have implemented an iterative algorithm based on the intensity distribution of the LV.

3.2.1 Rician Distribution of the LV in LGE CMR Images

In the presence of noise, the intensity of MR images is shown to be governed by a Rician distribution (Gudbjartsson & Patz, 1995). In the case of the LV in LGE images, the Rayleigh distribution models normal myocardium (dark regions) while the Gaussian distribution models infarcts plus the BP (bright regions), and the entire LV is modeled with the mixture model:

$$\begin{aligned} Rcn(x) &= Pr_{\mathrm{Ray}}(x) + Pr_{\mathrm{Gau}}(x) \\ &= \underbrace{\alpha_{\mathrm{R}} \frac{x}{\sigma_{\mathrm{R}}^2} \exp(-\frac{x^2}{2\sigma_{\mathrm{R}}^2})}_{\text{Rayleigh distribution}} + \underbrace{\alpha_{\mathrm{G}} \frac{1}{\sqrt{2\pi}\sigma_{\mathrm{G}}} \exp[-\frac{1}{2}(\frac{x-\mu_G}{\sigma_{\mathrm{G}}})^2]}_{\text{Gaussian distribution}}, \end{aligned} \tag{3.4}$$

where $Pr_{\mathrm{Ray}}(x)$ and $Pr_{\mathrm{Gau}}(x)$ denote the Rayleigh and Gaussian distributions respectively, and α_{R}, δ_{R}, α_{G}, δ_{G}, μ_G their parameters. The combination of the BP and infarcts as one class is not only reasonable because there is no significant difference between their intensity distributions (Kolipaka *et al.*, 2005), but also helpful to make the assumed bimodal distribution more prominent (Tao *et al.*, 2010). During the acquisition of LGE CMR images, technologists try to

null signals from the normal myocardium as much as possible in order to give prominence to the hyper-enhanced regions. Consequently, the intensities of the normal myocardium is often shifted to the dark side with an unknown offset. It has been suggested that introducing an extra offset parameter a to the Rayleigh distribution would lead to more accurate estimation of (3.4) (Elagouni *et al.*, 2010). We follow this approach and thus $Pr_{\mathrm{Ray}}(x)$ becomes:

$$Pr_{\mathrm{Ray}}(x) = \alpha_{\mathrm{R}} \frac{(x+a)}{\sigma_{\mathrm{R}}^2} \exp\left[-\frac{(x+a)^2}{2\sigma_{\mathrm{R}}^2}\right]. \tag{3.5}$$

We extract all the LV voxels from the regions enclosed by the epicardial contours in the stack of SA slices and obtain the intensity histogram. We then obtain a *relative probability* distribution by normalizing the histogram with the largest frequency count and fit the relative probability distribution to (3.4) to solve for $Rcn(x)$. Figure 3.4 shows an example of the fitted Rician distribution overlaid on the relative probability distribution. The intersection of $Pr_{\mathrm{Ray}}(x)$ and $Pr_{\mathrm{Gau}}(x)$ is found and denoted as i_{thrh}. Thereafter BP voxels can be extracted from the regions enclosed by the endocardial contours but excluding those with intensities smaller than i_{thrh} (considered as papillary muscles). We take the middle slice in the SA stack as the reference and calculate the mean intensity of its BP pixels $i_{\mathrm{m\_ref}}$. Then the rest of the slices are normalized by multiplying the factor $i_{\mathrm{m\_ref}}/i_{\mathrm{m\_k}}$, where $i_{\mathrm{m\_k}}$ is the mean intensity of the BP pixels in the k^{th} slice. Finally, the whole stack of slices are normalized *together* to the range $[0, 1]$.

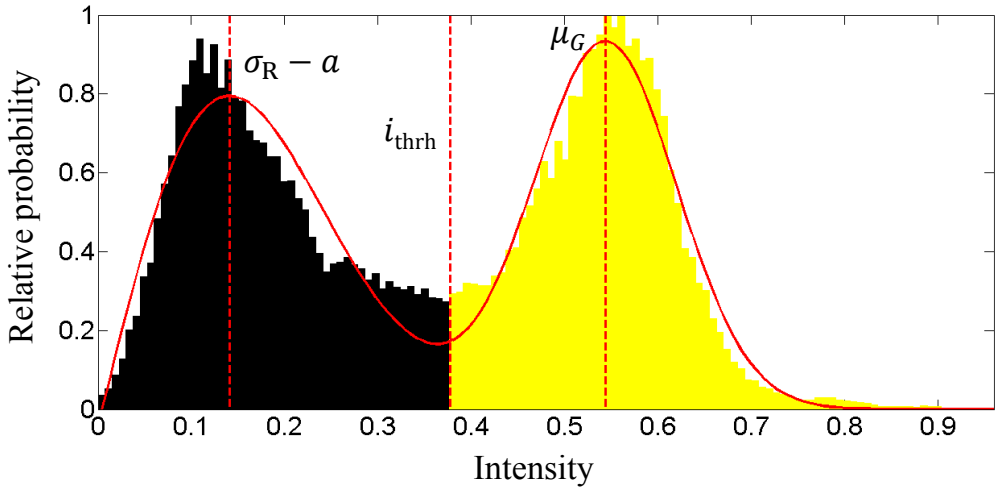

Figure 3.4: The fitted Rician distribution overlaid on the relative probability distribution. Also overlaid are vertical position lines of $\sigma_{\mathrm{R}} - a$, i_{thrh} and μ_G.

3.2.2 Iterative Normalization

Since the above described procedure may have changed the shape of the underlying intensity histogram of the stack of LGE slices, it is likely that if we repeat we would still find $i_{\mathrm{m\_ref}}/i_{\mathrm{m\_k}}$ unequal to 1 (as i_{thrh} is changed along with the histogram shape). Therefore, we iterate the normalizing procedure until the histogram stabilizes, which is determined by examining how close the ratio $i_{\mathrm{m\_ref}}/i_{\mathrm{m\_k}}$ is to 1 for every slice. Figure 3.5 shows slices of a dataset before and after the intensity normalization as a comparison. The final $Pr_{\mathrm{Ray}}(x)$ and $Pr_{\mathrm{Gau}}(x)$ obtained when the iteration stops will be used further for infarct classification by the graph-cut algorithm (presented later in Section 5.1.2).

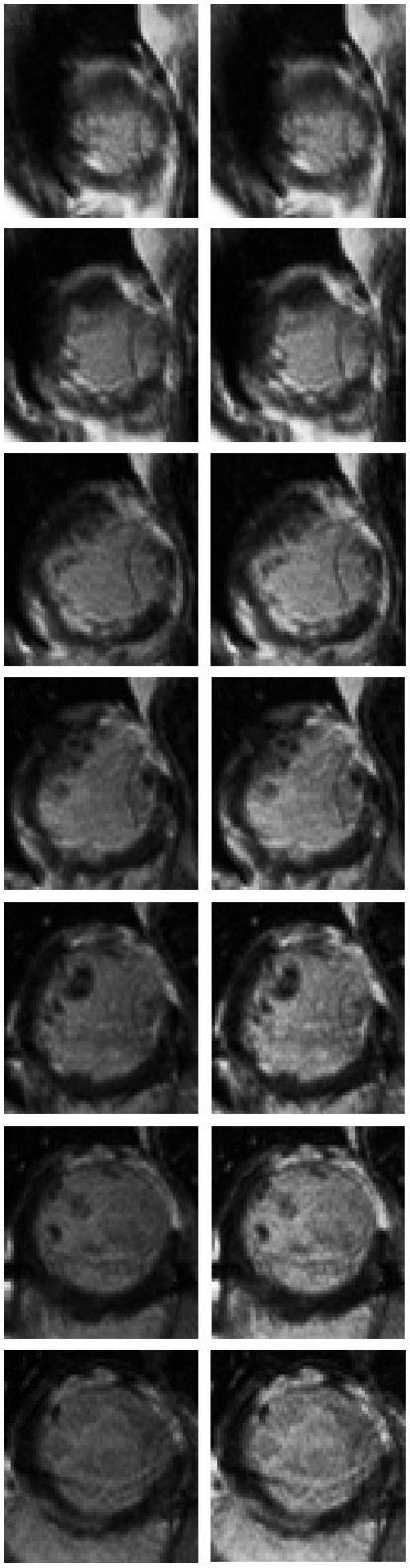

Figure 3.5: Illustration of the intensity normalization. First row: a stack of original SA images in one dataset; images become brighter from the mitral valve to the apex. Second row: the same image stack after the correction of intensity inconsistency; the image intensities, especially in the LV regions, are more consistent.

Chapter 4

Myocardium Segmentation

This chapter presents a comprehensive 3D method for myocardium segmentation in LGE CMR images, which greatly improves upon our previous work on a 2D myocardium segmentation method (Wei *et al.*, 2011). Section 4.1 first gives an overview of the proposed 3D method and its features that distinguish the method from most related works. Then Sections 4.2 to 4.5 describe the method in detail. Finally, Section 4.6 presents and discusses the experimental results.

4.1 Overview

Given myocardial contours in cine images as *a priori* knowledge, our 3D segmentation method initially propagates the *a priori* segmentation from cine to LGE images via 2D translational registration. Two meshes representing respectively endocardial and epicardial surfaces are then constructed with the propagated contours. After construction, the two meshes are deformed towards the myocardial edge points detected in both SA and LA LGE images in a unified

3D coordinate system. Taking into account the intensity characteristics of the LV in LGE images, we propose a novel parametric model of the LV for consistent myocardial edge points detection regardless of pathological status of the myocardium (infarcted or healthy) and of the type of the LGE images (SA or LA). The final meshes after the nonrigid deformation are themselves a 3D segmentation of the myocardium. We have evaluated the proposed method with 20 sets of real patient and 4 sets of simulated phantom data. Both distance- and region-based performance metrics confirm the observation that the method can generate accurate and reliable results for myocardial segmentation of LGE images. We have also tested the robustness of the method with respect to varied *a priori* segmentation in both practical and simulated settings. Experimental results show that the proposed method can greatly compensate variations in the given *a priori* knowledge and consistently produce accurate segmentations.

The proposed method is distinct from the related works (Ciofolo *et al.*, 2008; Dikici *et al.*, 2004) in four aspects. (i) We integrate the standard 4C and 2C LA images with SA images for the 3D segmentation. Besides providing complementary information about the LV between the largely spaced SA images, the LA images are also used for the correction of misalignment artifacts among slices. (ii) We propose a novel parametric model of the LV for LGE images based on 1D intensity profiles. This model is flexible to be applied to both SA and LA images, and self-adaptive to detect edge points of both infarcted and healthy myocardium. Further, it detects paired endocardial and epicardial edge points simultaneously. (iii) Instead of using conventional similarity metrics such as mutual information (Collignon *et al.*, 1995) and cross-correlation, experimentally we choose *pattern intensity* (Weese *et al.*, 1997) which leads to

accurate translational registration of cine and LGE images with high success rates. (iv) We introduce an effective thickness constraint for the 3D deformation scheme based on the simplex mesh geometry (Delingette, 1999), which can also be applied to other scenarios involving coupled boundaries.

The proposed method comprises four major steps: (i) selection and pre-processing of target LGE images and corresponding cine images; (ii) 2D translational registration to initially propagate the *a priori* segmentation from cine to LGE images; (iii) misalignment correction of the LGE images; and (iv) 3D non-rigid deformation of the myocardial meshes (constructed from the propagated contours) driven by features in both SA and LA LGE images.

4.2 Data Selection and Pre-Processing

First, we display all the SA LGE slices of one subject for user selection. Typically, all the slices are chosen, except for the most basal slice(s) in which the myocardium is very thin and dim, and the most apical slice(s) in which the myocardium can hardly be discerned or the slices are already out of the LV. The user also selects one 4C and one 2C LA LGE slice based on image contrast. Once the target LGE slices are chosen, the corresponding SA cine images are automatically selected. While a cine sequence includes multiple frames which cover the entire cardiac cycle, an LGE sequence has only one frame usually triggered between end-systole and end-diastole. We select the cine image with the same slice location as and the closest phase[1] to the LGE image according to the DICOM header information, and delineate the myocardial contours in the

[1]Due to the inherent imperfection of the ECG gating, exact phase matching is often impossible.

selected cine image as *a priori* segmentation. The delineation is done with a semi-automatic method (Li *et al.*, 2009) with manual corrections where necessary. Finally, we normalize each pair of corresponding cine and LGE SA images to the same physical resolution (pixel size) by resizing the cine image.

4.3 Translational Registration

The segmentation starts by propagating the *a priori* segmentation in the cine image to the LGE image by 2D translational registration. In our previous work (Wei *et al.*, 2011), we implemented a constrained affine registration using normalized cross correlation (NCC) as the similarity metric. However, after extensive experiments with different similarity metrics and degrees of freedom, we found that by using *pattern intensity* (PI; Weese *et al.*, 1997) as the similarity metric, a translational registration can already reach the same or sometimes better performance.

The key factor leading to the good performance of the simple translational registration is the employment of PI as the similarity metric (a detailed comparative study is presented in Section 4.6.5, page 87). Given two images I_1 and I_2, PI operates on the difference image $I_{\text{diff}} = I_1 - I_2$. If I_1 and I_2 are two well-registered images of the same object, structures from this object should vanish and there should be a minimum number of structures or patterns in I_{diff}. A suitable similarity measure should, therefore, characterize the *structuredness* of I_{diff}. PI considers a pixel of I_{diff} to belong to a structure if it has a significantly different value from its neighboring pixels. Using a constant radius r to

define the neighborhood, the PI is defined as:

$$\begin{aligned} P_{r,\delta}(I_1, I_2) &= P_{r,\delta}(I_{\text{diff}}) \\ &= \frac{1}{N_{I_{\text{diff}}}} \sum_{x,y} \frac{1}{N_r} \sum_{v,w} \frac{\delta^2}{\delta^2 + [I_{\text{diff}}(x,y) - I_{\text{diff}}(v,w)]^2}, \end{aligned} \tag{4.1}$$

where (x, y) denotes the pixels in I_{diff}, and (v, w) the neighboring pixels of (x, y) within radius r; they satisfy the relationship $(x-v)^2+(y-w)^2 \leq r^2$. $N_{I_{\text{diff}}}$ and N_r denote the number of pixels in I_{diff} and the neighborhood respectively. A constant δ is introduced to suppress the impact of noise.

A rectangular ROI is defined in the cine image regarding the LV, and used as the matching window for the calculation of the similarity measure. As shown in Fig. 4.1(a), we first identify the bounding box of the LV in the cine image with the pre-delineated epicardial contour, and then define the ROI by enlarging the bounding box to twice its original size. A window of the same size as the ROI is placed in the LGE image and translated to search for the best match, i.e., the one giving the maximum $P(I_{\text{diff}})$ between the two windows. After obtaining the optimal translation, the pre-segmented myocardial contours in the cine image (Fig. 4.1(b)) are translated accordingly and become a coarse segmentation of the myocardium in the LGE image. Figure 4.1(c) shows an example result of this translational registration. In general the translated contours are close to the myocardial boundaries. However, a discrepancy exists in the region highlighted with the red square. Such discrepancies are often caused by the elastic deformation and out-of-plane motion of the heart, and different tissue structures such as pericardial fat. Therefore, nonrigid deformation is needed to eliminate such discrepancies.

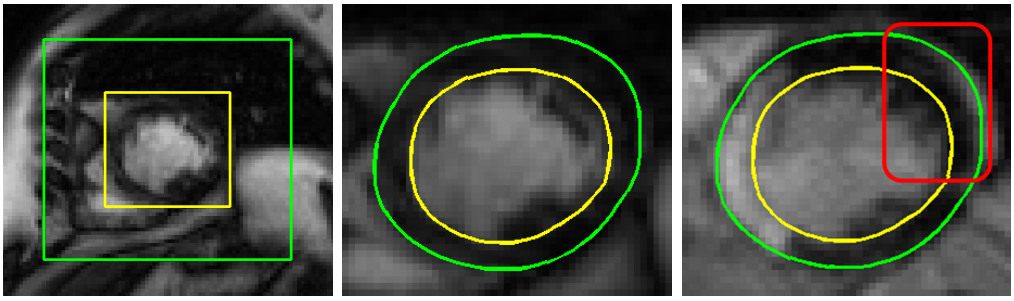

(a) (b) (c)

Figure 4.1: Illustration of the translational registration. (a) The cine image with bounding box of the LV (the yellow square) and the defined ROI (the green square) overlaid. (b) The cine image with pre-delineated contours overlaid. (c) The LGE image with translated contours overlaid. In general the contours segment the myocardium closely, but in the region indicated by the red square, a discrepancy is observed.

4.4 Misalignment Correction

Prior to our 3D nonrigid deformation, misalignment of a set of LGE slices must be corrected. We have discussed the causes and impacts of misalignment artifacts in Section 2.4.1. More specific to our 3D segmentation framework, misalignment can cause at least two problems. First, if one SA slice is largely deviated from its original 3D position within the LV, the external attracting force derived from this slice would conflict with the internal smoothing force derived from the rest SA slices that remain in their original 3D positions. Second, if the LA and SA slices are not correctly aligned, reliable integration of them to facilitate the 3D segmentation would be impossible. We use the method presented in Section 3.1 to correct any potential misalignment artifacts in our LGE datasets. The coarse epicardial contours obtained by the translation registration are used to define the ROI's in SA slices required by the correction method.

4.5 Three-Dimensional Nonrigid Deformation

After misalignment correction, we apply a 3D nonrigid deformation to surface meshes constructed with the coarse endocardial and epicardial contours obtained via the translational registration (denoted by $C_{\mathrm{endo,\,rigid}}$ and $C_{\mathrm{epi,\,rigid}}$ afterwards). First, we detect myocardial edge points in both SA and LA LGE images. Second, we initialize two simplex meshes (Delingette, 1999) with $C_{\mathrm{endo,\,rigid}}$ and $C_{\mathrm{epi,\,rigid}}$, respectively. Third, we deform the meshes with both external and internal forces. The final meshes after the deformation are naturally a 3D segmentation of the LV.

4.5.1 A Novel Parametric Model of the LV in LGE Images

Taking into account intensity characteristics of the myocardium in LGE images, we propose a novel parametric model of the LV based on 1D intensity profiles (Kaftan *et al.*, 2009; Vu *et al.*, 2007; Zadicario *et al.*, 2008). This model has the following desirable properties: it automatically adapts to either healthy or infarcted myocardium and consistently detects reliable myocardial edge points; it is flexible to be applied to both SA and LA images with minor alteration; it detects paired endocardial and epicardial edge points at the same time with variable thickness of the myocardium; and it does not make the assumption that enhancements always reside sub-endocardium in every infarcted SA image, which was made by our earlier work (Wei *et al.*, 2011).

We now introduce the proposed model with reference to an SA image (Fig. 4.2). We find the LV center O_{LV} by averaging all the contour points on $C_{\mathrm{endo,\,rigid}}$ and $C_{\mathrm{epi,\,rigid}}$, and then sample 1D intensity profiles along 79 evenly

spaced radial directions emanating from O_{LV} (Fig. 4.2(a)). These intensity profile samples are denoted by $I_{\mathrm{sample}}(\theta)$.

We model 1D intensity patterns along the radial rays from O_{LV} to beyond the epicardium with intensity profile templates $I_{\mathrm{templt}}(w, t, s, d)$, where w denotes the distance from O_{LV} to the endocardium, t the thickness of the myocardium, s the thickness of the enhancement and d the distance from the endocardium to the enhancement. The endocardial and epicardial edge points can be expressed by the parameters w and t:

$$\begin{aligned} C_{\mathrm{endo}}(\theta) &= O_{\mathrm{LV}} + \boldsymbol{n}(\theta) \cdot w(\theta), \\ C_{\mathrm{epi}}(\theta) &= O_{\mathrm{LV}} + \boldsymbol{n}(\theta) \cdot [w(\theta) + t(\theta)], \end{aligned} \tag{4.2}$$

where $\boldsymbol{n}$ denotes the unit vector along the emanating ray. For every sampled angle θ, if $w(\theta)$, $t(\theta)$, $s(\theta)$ and $d(\theta)$ are correct, they would produce an $I_{\mathrm{templt}}(w,\, t,\, s,\, d)$ which is most similar to $I_{\mathrm{sample}}(\theta)$. Therefore, the problem of finding C_{endo} and C_{epi} is now converted to searching for the desired $(w_{\mathrm{d}},\, t_{\mathrm{d}},\, s_{\mathrm{d}},\, d_{\mathrm{d}})$ for each θ. Let $Err(I_1,\, I_2)$ denote a mismatch measurement function, for which we adopt the commonly used MSD. Thus the desired $(w_{\mathrm{d}},\, t_{\mathrm{d}},\, s_{\mathrm{d}},\, d_{\mathrm{d}})$ is given by:

$$(w_{\mathrm{d}},\, t_{\mathrm{d}},\, s_{\mathrm{d}},\, d_{\mathrm{d}}) = \arg\min\{Err[I_{\mathrm{templt}}(w,\, t,\, s,\, d),\, I_{\mathrm{sample}}]\}. \tag{4.3}$$

As $I_{\mathrm{sample}}(\theta)$ is purposely sampled far beyond epicardium and thus always longer than the devised $I_{\mathrm{templt}}(w,\, t,\, s,\, d)$, when we compare the two only the first $w(\theta) + t(\theta)$ pixels of $I_{\mathrm{sample}}(\theta)$ are used.

For infarcted myocardium (e.g., the red ray in Fig. 4.2(b)), an exemplary

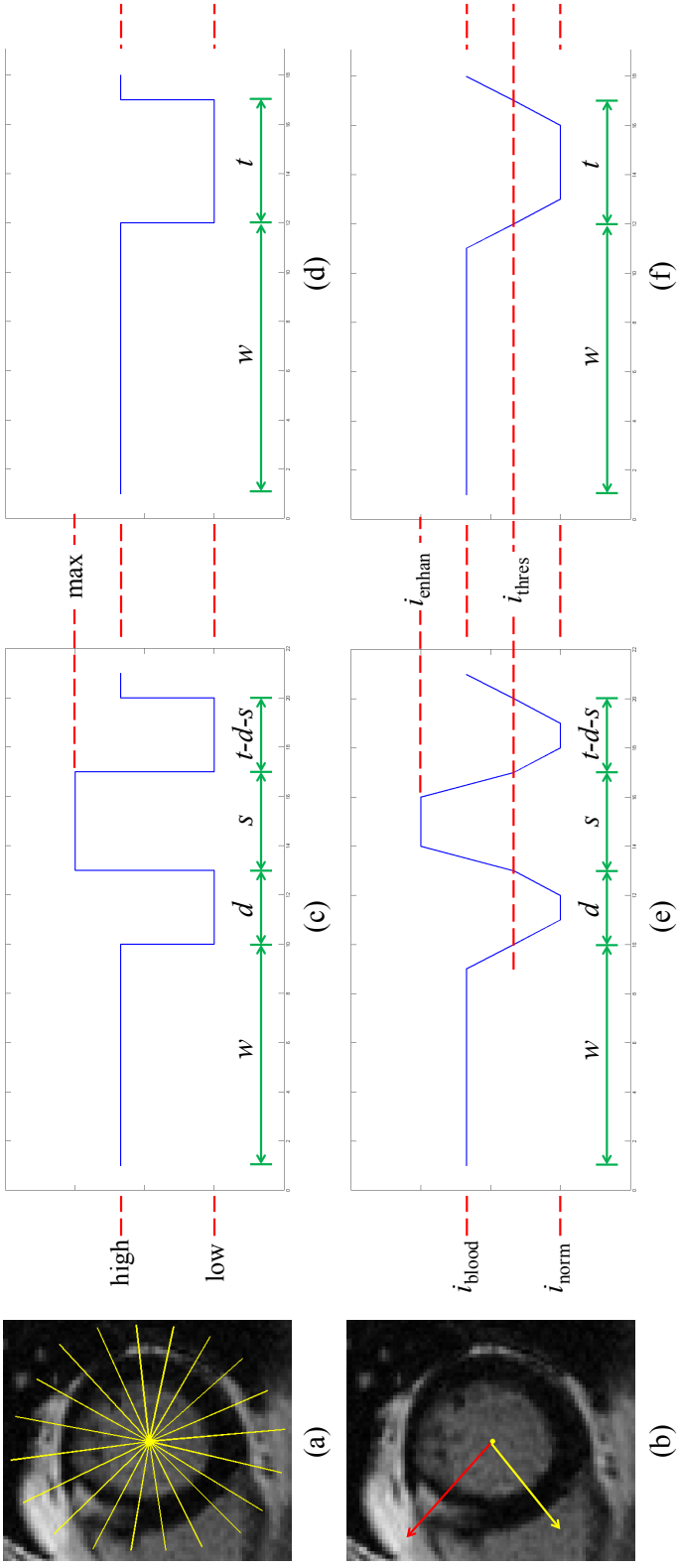

Figure 4.2: (a) A representative SA LGE image is sampled along evenly spaced rays. (b) Yellow ray: a sample ray corresponding to normal myocardium; red ray: a sample ray corresponding to infarcted myocardium. (c) An intensity profile template $I_{\text{templt}}(w, t, s, d)$ devised to model the case of infarcted myocardium. (d) An intensity profile template simplified from (c), i.e., $s = 0$, to model the case of normal myocardium. (e)-(f) More realistic intensity profile templates with values estimated from the LGE image and gradual transitions. Note: for better illustration, relative lengths of w, t, s and d in (c)-(f) do not strictly follow the two sample rays in (b).

$I_{\text{templt}}(w,\ t,\ s,\ d)$ is shown in Fig. 4.2(c). The first w pixels are set to high (the BP), followed by d pixels low (the un-enhanced myocardium), then s pixels maximum (the enhancement should display a higher intensity than the BP in an *ideal* case) and the remaining $(t-d-s)$ pixels low. This template is able to cover most enhancement patterns found in ischemic heart disease: for sub-endocardial enhancements, $d = 0$ and $s < t$; for transmural enhancements, $d = 0$ and $s = t$; for mid-myocardium enhancements, such as in cases of MVO, $d > 0$ and $0 < s < t$. For normal myocardium (e.g., the yellow ray in Fig. 4.2 (b)), $s = 0$ and the value of d has no impact (but has to satisfy $0 \leq d \leq t$), and the corresponding profile template is illustrated in Fig. 4.2 (d).

Since nearly all infarcts originate from the sub-endocardium (Hunold *et al.*, 2005; Reimer *et al.*, 1979), our previous work assumed that enhancements always reside there in every SA image with infarcts (Wei *et al.*, 2011). However, this assumption is occasionally violated in practice. One such example is shown in Fig. 4.3, where three consecutive SA LGE slices are displayed. The infarcts do grow from the sub-endocardium in 3D. But when the leftmost slice is treated alone, the assumption no longer holds due to the loss of 3D spatial continuity. A possible solution is to keep this assumption but impose it in 3D (Hsu *et al.*, 2006b). Alternatively, we completely relax the assumption and introduce the parameter $d(\theta)$ to describe the position of the enhancement within the myocardium. Without this assumption, our model is clinically more flexible to deal with diverse LGE data.

Given the translated epicardial contours, representative intensity values are estimated from the LGE images and used to devise the intensity profile templates. All the pixels enclosed by $C_{\text{epi, rigid}}$ in all the SA slices of the same

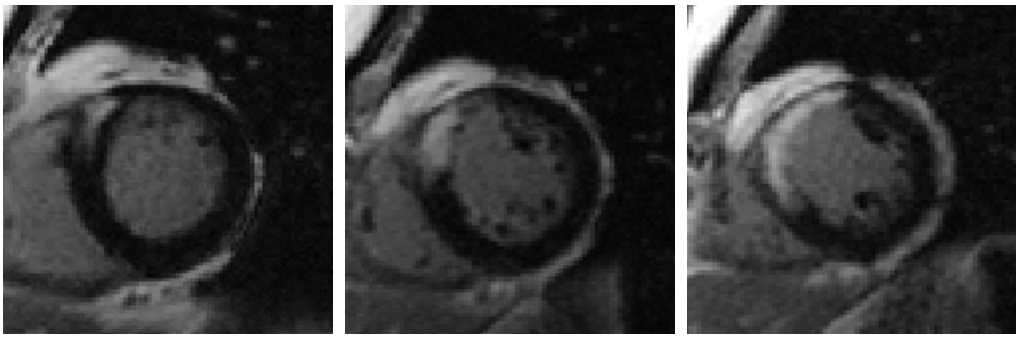

Figure 4.3: From left to right: three consecutive SA LGE slices. The infarcts grow from sub-endocardium in 3D. However, when considering the leftmost slice alone, the same conclusion can hardly be drawn due to the loss of 3D spatial continuity.

subject are classified into two classes by Otsu's threshold (Otsu, 1979) i_{thres}. Then i_{norm}, the mean of all the pixels below i_{thres} is used as the value of normal myocardium when devising the templates. All the pixels above i_{thres} are further classified by k-means clustering into two clusters, whose centers (i_{blood} and i_{enhan}) are used as the values of the BP and enhancements, respectively. To mimic the gradual transition between bright and dark regions, i_{thres} is used as the transition value. With these values, we can devise intensity profile templates which resemble the samples with higher fidelity (Figs. 4.2 (e) and (f)).

Figure 4.4 shows sample results of applying the proposed 1D profile model to myocardium of various typical pathological states: normal myocardium, sub-endocardial, transmural and mid-myocardial infarcts. For each example, a radial direction is designated and starting positions of endocardial and epicardial edge points are manually placed along it. To mimic the discrepancies after translational registration, these starting points are deliberately placed off true myocardial boundaries. Then the desired $(w_{\mathrm{d}},\, t_{\mathrm{d}},\, s_{\mathrm{d}},\, d_{\mathrm{d}})$ is found by an exhaustive search of all possible combinations of $(w,\ t,\ s,\ d)$ within a narrow band of

the starting positions. During the search, the step size used for w, t, s and d is set to 1 pixel. As shown in the third column of Fig. 4.4, the detected paired endocardial and epicardial edge points are correct for all the four cases.

4.5.2 Myocardial Edge Points Detection in SA Images

Although the parametric model is flexible and adaptive, sometimes it may be trapped by similar but false edges such as the edge between the thin slice of fat and the lung surrounding the LV due to its 1D nature. In order to avoid such traps by imposing continuity constraints on individual 1D intensity profiles, we incorporate this model in an energy minimization scheme. This scheme is applicable to both SA and LA images, but we first describe it using SA images. The application of the parametric model and the energy minimization scheme to LA images will be described in the next section.

The energy to be minimized comprises an intensity profile match term and a smoothness term weighted by a constant λ:

$$E = E_{\text{match}} + \lambda \cdot E_{\text{smooth}}. \tag{4.4}$$

E_{match} is simply a summation of the mismatch measurements over all the sampled radial angles θ:

$$E_{\text{match}} = \sum_{\theta} Err[I_{\text{templt}}(w(\theta),\, t(\theta),\, s(\theta),\, d(\theta)),\, I_{\text{sample}}(\theta)]. \tag{4.5}$$

Since both the endocardial and epicardial contours are parameterized as $C(\theta) =$

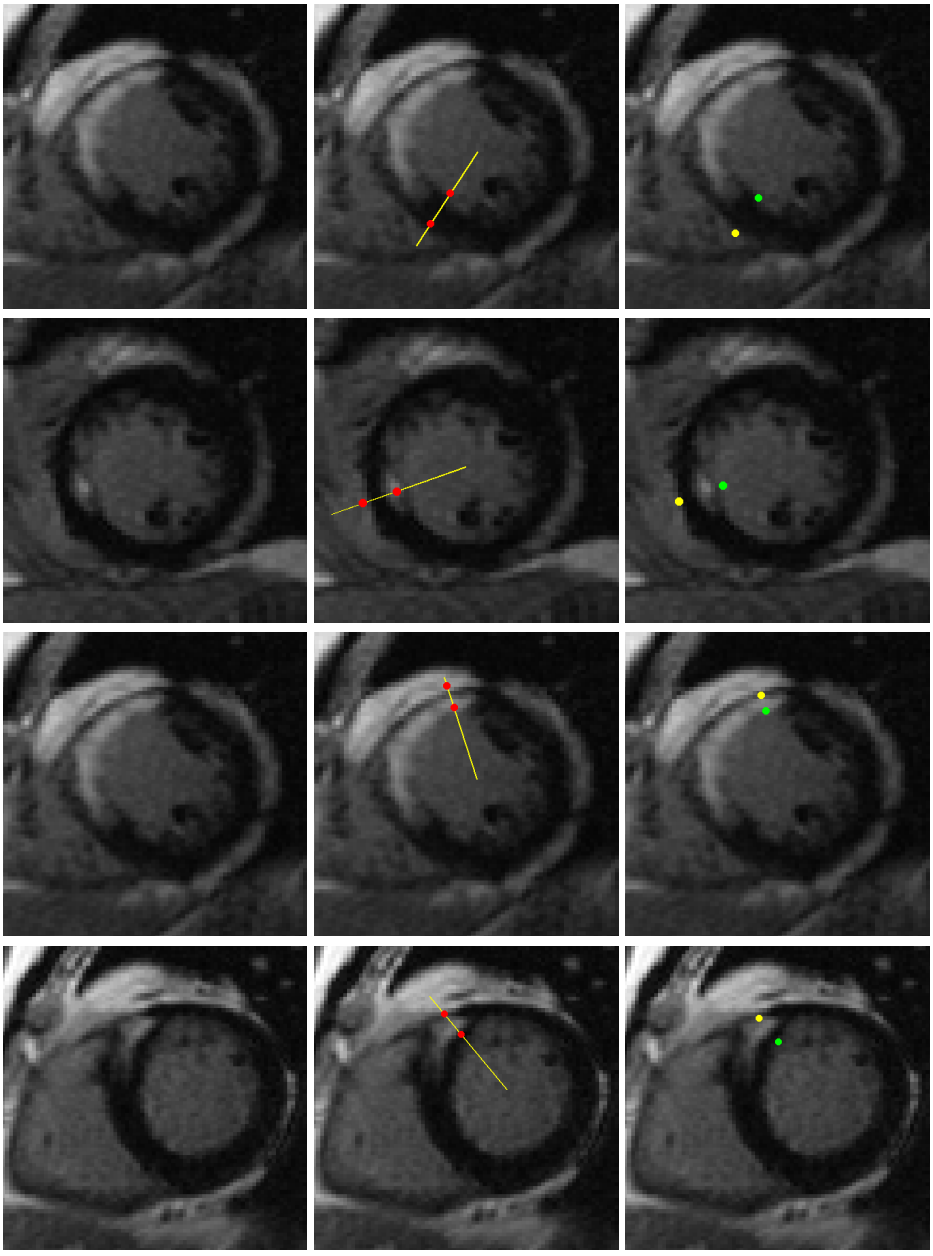

(a) (b) (c)

Figure 4.4: Sample results of applying the proposed 1D profile model to myocardium of various typical pathological states (from the first to the fourth row): normal myocardium, sub-endocardial, transmural and mid-myocardial infarcts. (a) LGE images. (b) The yellow lines indicate radial directions along which myocardial edge points are currently searched for. The manually placed red dots provide starting positions for the search. Note that they are deliberately placed off true myocardial boundaries. (c) Myocardial edge points found via exhaustive search for $(w_{\mathrm{d}},\, t_{\mathrm{d}},\, s_{\mathrm{d}},\, d_{\mathrm{d}})$ within a narrow band around the starting positions.

$(w(\theta),\, t(\theta))$, we define E_{smooth} as

$$E_{\text{smooth}} = \sum_{\theta} [(C_\theta)^2 + (C_{\theta\theta})^2], \tag{4.6}$$

where C_θ and $C_{\theta\theta}$ denote first and second order derivatives, respectively. By minimizing E_{smooth}, the endocardial and epicardial contours tend to deform into two concentric circles. The energy in (4.4) is minimized with w and t constrained within a narrow band of $(w_0,\, t_0)$, which are the original w and t computed from $C_{\text{endo, rigid}}$ and $C_{\text{epi, rigid}}$.

Next, we discuss the influence of papillary muscles (e.g., the dark region indicated by the arrow in Fig. 4.5 (c)) on the proposed model. Since we do not consider the papillary muscles when devising I_{templt}, their presence does influence the mismatch measurement $Err(I_{\text{templt}},\, I_{\text{sample}})$. However, by incorporating the parametric model into the energy minimization scheme, the detection of myocardial edge points is made robust to the papillary muscles in two ways: (i) by using a constrained optimization within a narrow band of the original $(w_0,\, t_0)$, papillary muscles resulting in $(w,\, t)$ pairs very distant from $(w_0,\, t_0)$ are directly eliminated; (ii) the continuity constraints on both w and t can prevent endocardial edge points from being dragged too far from their neighbors by the papillary muscles.

Figure 4.5 shows three examples of the detected myocardial edge points in SA images. Notably in Figs. 4.5 (b) and (c), where there is a large area of transmural infarcts completely blending in with the BP and surrounding tissues or papillary muscles are present, our method still provides reasonable myocardial edge points because of the smoothness term and narrow-band constraint.

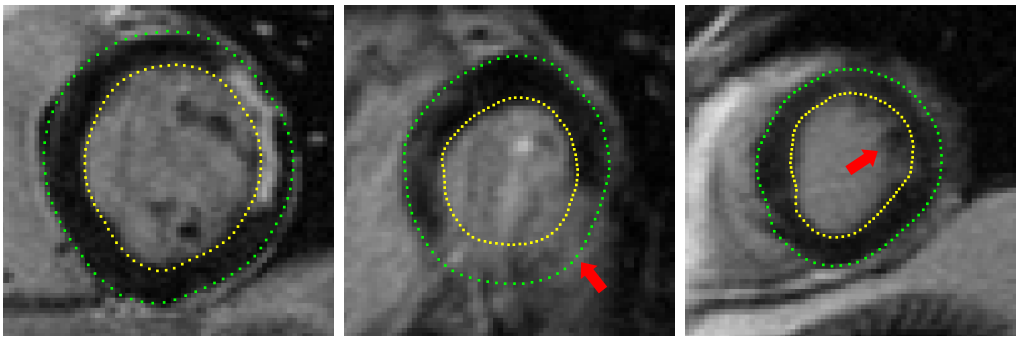

(a) (b) (c)

Figure 4.5: Examples of the detected myocardial edge points in SA images. Even when there is a large area of transmural infarcts completely blending in with the BP and surrounding tissues in (b) or papillary muscles are present in (c), our method still provides reasonable myocardial edge points.

4.5.3 Myocardial Edge Points Detection in LA Images

Different from the parameterizing variable used for SA images (i.e., radial angles θ), slice locations l along the normal to the SA image planes are used to parameterize myocardial contours in LA images (Fig. 4.6(a)). Hence, myocardial contours are expressed as $C(l) = (w(l),\, t(l))$. [1] We sample the LA images along rays pointing from the central axis of the LV to beyond the epicardium (Fig. 4.6(b)); the samples are denoted as $I_{\text{sample}}(l)$. Again, we devise $I_{\text{templt}}(w, t, s, d)$ with tentative (w, t, s, d) and search for the optimal tetrad which makes I_{templt} most resemble I_{sample} for each l.

Now two questions are how to estimate: (i) the central axis of the LV and (ii) reasonable starting points for the search of the optimal (w, t, s, d). To answer both questions, we intersect $C_{\text{endo, rigid}}$ and $C_{\text{epi, rigid}}$ with the LA image planes. The intersection points serve as the initial coarse myocardial edge points in the

[1] Note that in an LA image each l actually defines dual sets of $C_{\text{endo}}(l)$ and $C_{\text{epi}}(l)$, as the myocardium is divided into two sides by the central axis of the LV. Since we treat the two sides *separately* in exactly the same way, we use only one side for the purpose of elaboration.

Figure 4.6: (a) SA slice locations are used to parameterize myocardial contours in LA images. (b) 1D intensity profiles I_{sample} are sampled along the rays pointing from the central axis of the LV to beyond the epicardium. (c) Intersection points of the LA image with $C_{\text{endo, rigid}}$ and $C_{\text{epi, rigid}}$; they are used as starting points of the search for myocardial edge points and to estimate the central axis of the LV. (d) More points are interpolated between SA slices, in order to fully utilize information contained in the LA images.

LA images. Points on the central axis can be easily estimated by averaging the four intersection points on the same SA slices (Fig. 4.6(c)). The intersections also naturally define the parametrization scheme (i.e., values of l) by the relative location of each SA slice with respect to the LA image planes. However, the SA slices are too sparse and thus there are too few l's. On one hand, the SA slices are far away from each other, causing the loss of anatomical continuity of the myocardium; on the other hand, the LA images actually contain *far more* information than what is provided by the intersected locations. In order to retain the natural smoothness of the myocardium and utilize as much information in LA images as possible, we make l denser by linearly interpolating between neighboring SA slices (Fig. 4.6(d)). One might raise the concern that linear interpolation is not flexible enough to fit the curved LV, but this is not a problem because these points are only used as a guessing start and will be refined. The proposed myocardial edge points detection for LA images only requires a rough initialization to detect more accurate edge points.

We use the same energy minimization scheme for LA images as for SA images. The energy functional to be minimized still comprises two terms E_{match} and E_{smooth} as in (4.4). E_{match} stays the same as in (4.5), except that the parametrization variable is l. However, E_{smooth} in (4.6) must be slightly adapted to accommodate the shape of the LV in LA images. That is, in LA images w tends to gradually shrink from the base to apex of the LV. Therefore, the first order derivative of w is removed from (4.6) and E_{smooth} becomes:

$$E_{\text{smooth}} = \sum_{l} [(w_{ll})^2 + (t_l)^2 + (t_{ll})^2]. \tag{4.7}$$

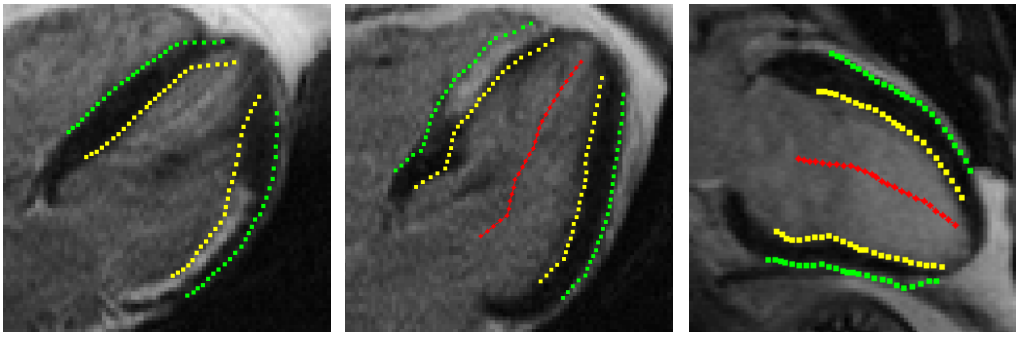

Figure 4.7: Examples of the detected myocardial edge points in LA images. The first two images are 4C views, while the last one is a 2C view.

Several examples of the detected myocardial edge points in LA images are shown in Fig. 4.7.

4.5.4 The Deformation Scheme

We use the *simplex mesh* (Delingette, 1999) geometry and a Newtonian law of motion to represent and deform the contours. Both endocardial and epicardial surfaces are represented with a simplex mesh, respectively, and deformed in an inter-related manner. At each vertex we define three forces, namely, smoothness force $\boldsymbol{F}_{\text{smooth}}$, edge attraction force $\boldsymbol{F}_{\text{edge}}$ and myocardium thickness force $\boldsymbol{F}_{\text{thick}}$. $\boldsymbol{F}_{\text{smooth}}$ imposes uniformity of vertex distribution and continuity of simplex angles (Delingette, 1999). $\boldsymbol{F}_{\text{edge}}$ draws vertices towards detected myocardial edge points along the normal direction at each vertex. Finally, $\boldsymbol{F}_{\text{thick}}$ maintains proper distances between paired endocardial and epicardial vertices. Letting p^t denote the position of any vertex at time t, the deformation scheme is given by

$$p^{t+1} = p^t + (1-\gamma)(p^t - p^{t-1}) + \alpha \boldsymbol{F}_{\text{smooth}} + \beta \boldsymbol{F}_{\text{edge}} + \mu \boldsymbol{F}_{\text{thick}}, \qquad (4.8)$$

where γ is a damping factor, and α, β and μ are respective weights.

We initialize the simplex mesh for the epicardium with $C_{\mathrm{epi,\,rigid}}$ in the steps described below.

Above all, we transform all the involved coordinates to the image coordinate system of the last SA slice. We then re-sample $C_{\mathrm{epi,\,rigid}}$ with evenly spaced radial angles. The resampling makes the connection relationship among mesh vertices straightforward by aligning all vertices on all slices along the same radial angles, hence simplifying mesh construction. After that we interpolate to obtain several planar contours evenly spaced between the physically existing SA slices. The interpolation is necessary because (i) considering the large distance between neighboring SA slices, properly densified vertices can make $\boldsymbol{F}_{\mathrm{smooth}}$ more meaningful; and (ii) some of the interpolated vertices will be attracted by myocardial edge points detected in LA images, which in turn can affect the vertices on the physically existing SA slices through $\boldsymbol{F}_{\mathrm{smooth}}$.

Now we specify the connection relationship among vertices. We use the vertices on the two boundary SA slices (the most basal and apical ones) to form two *planar 1-simplex meshes* (Delingette, 1999), where each vertex is connected to its two immediate neighbors in the image plane. These two 1-simplex meshes act as boundary conditions of the surface mesh. Planar 1-simplex meshes are used to prevent the vertices on the boundaries of the surface mesh from changing their z-values during the deformation; that is, no contraction or elongation of the entire LV in the direction perpendicular to the SA image planes. For interjacent vertices, we follow these rules: (i) vertically, each vertex is connected to its immediate above and below neighbors; (ii) horizontally, each vertex is connected to its immediate left or right neighbor alternatively, i.e., if one vertex is

connected to its immediate left neighbor, then the two vertices next to it should be connected to their right neighbors. In simplex-mesh geometry, each vertex can only be connected to three neighbors.

The simplex mesh for the endocardium is initialized in the same way. One exemplary mesh constructed with the above steps is shown at the top of Fig. 4.8.

As in the original simplex mesh work (Delingette, 1999), we define $\boldsymbol{F}_{\text{edge}}$ with the notion of closest points. For each vertex p_i, we look for the closet pre-detected myocardial edge point $\hat{p}_i$ and define the edge attraction force as:

$$\boldsymbol{F}_{\text{edge}} = \omega_i \, G\left(\frac{(\hat{p}_i - p_i)\cdot \boldsymbol{n}_i}{D_{\text{cutoff}}}\right) \boldsymbol{n}_i, \text{ where } G(x) = \begin{cases} x, & \text{if } x \leq 1, \\ 0, & \text{if } x > 1. \end{cases} \tag{4.9}$$

Here, ω_i is a weight between 0 and 1, $\boldsymbol{n}_i$ the surface normal at vertex p_i. The gating function $G(x)$ filters out potential outliers specified by the cutoff distance D_{cutoff} – if the projected distance between $\hat{p}_i$ and p_i onto $\boldsymbol{n}_i$ is larger than D_{cutoff}, then $\hat{p}_i$ is considered an outlier and has no effect on p_i. The value of D_{cutoff} controls the tradeoff between capture range and robustness against outliers during mesh deformation.

ω_i is defined with regard to local intensity differences at $\hat{p}_i$. Recall that $\hat{p}_i$ is located on a 1D intensity profile sample I_{sample}. Assuming it is the jth pixel on I_{sample}, we calculate the weighted sum of absolute local intensity gradients (forward, backward and central differences):

$$\begin{aligned} S_i = {} & |I_{\text{sample}}(j+1) - I_{\text{sample}}(j)| + |I_{\text{sample}}(j) - I_{\text{sample}}(j-1)| \\ & + 0.5 * |I_{\text{sample}}(j+1) - I_{\text{sample}}(j-1)|, \end{aligned} \tag{4.10}$$

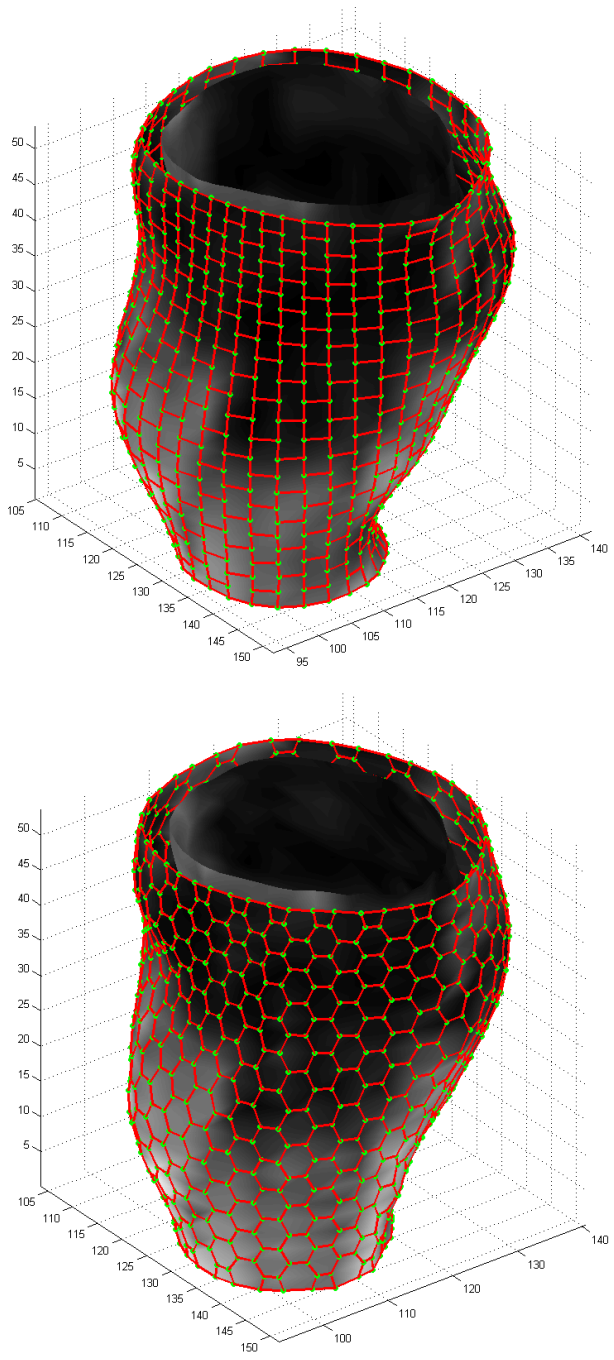

Figure 4.8: Top: illustration of an initial simplex mesh for the epicardial surface; bottom: illustration of the same simplex mesh after deformation. The green dots are the epicardial surface vertices while the red line segments represent the connection relationship among them. Also shown in both images is the endocardial surface without its mesh overlaid.

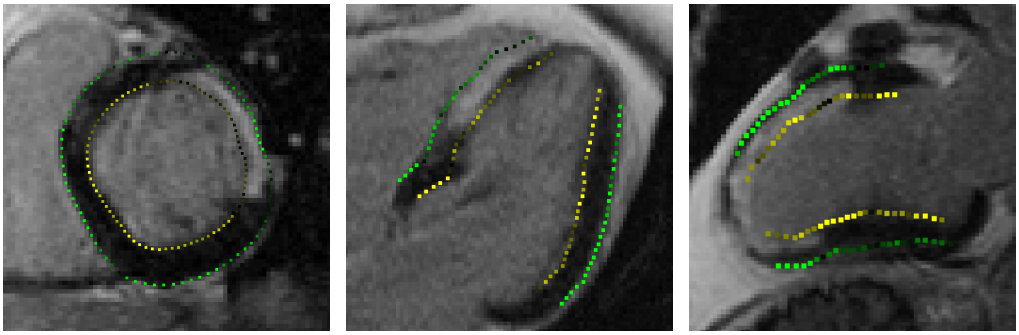

Figure 4.9: The effects of the weights on the detected myocardial edge points: the magnitude of ω_i is coded as brightness of the plot.

and define ω_i by:

$$\omega_i = \frac{S_i - \min(\{S_k\})}{\max(\{S_k\}) - \min(\{S_k\})}, \quad k = 1, 2, \cdots, n, \tag{4.11}$$

where $\{S_k\}$ is a set of S_i's to be normalized together. For SA slices, we process all the detected endocardial edge points of the entire stack as a set, and all the detected epicardial edge points as another set. For LA slices, 4C and 2C images are processed separately. The effects of the weights on the detected myocardial edge points are qualitatively visualized in Fig. 4.9, where the magnitude of ω_i is coded as brightness of the plot.

To define $\boldsymbol{F}_{\text{thick}}$, every endocardial vertex is paired with the coplanar epicardial vertex of the same re-sampling angle. Then a vector-based *spring* force is imposed to maintain the relative position between every pair. Letting p^0_{endo} denote any endocardial vertex before deformation, and p^0_{epi} its paired epicardial vertex, we define $\boldsymbol{F}_{\text{thick}}$ as:

$$\begin{aligned} \boldsymbol{F}_{\text{epi,thick}} &= p^t_{\text{endo}} + (p^0_{\text{epi}} - p^0_{\text{endo}}) - p^t_{\text{epi}}, \\ \boldsymbol{F}_{\text{endo,thick}} &= p^t_{\text{epi}} - (p^0_{\text{epi}} - p^0_{\text{endo}}) - p^t_{\text{endo}}, \end{aligned} \tag{4.12}$$

where p_*^t is the vertex after tth iteration. $\boldsymbol{F}_{\text{thick}}$ is particularly helpful when ω_i is weak at one of the paired vertices but strong at the other. In this case, as a robust supplement to $\boldsymbol{F}_{\text{smooth}}$, $\boldsymbol{F}_{\text{thick}}$ extrapolates a reasonable position for the vertex of weak ω_i with the original positional relationship between the pair.

With the meshes initialized and the driving forces defined, we can deform the two surface meshes iteratively with (4.8) [1]. In each iteration, we first fix the endocardial mesh and update the epicardial mesh, and then update the endocardial mesh with the epicardial mesh fixed. The deformation is stopped once the movement at any vertex is smaller than 0.1 pixel or the iteration reaches 30 times. A deformed surface mesh is shown at the bottom of Fig. 4.8, together with its original shape before deformation shown at the top. The two meshes obtained after the nonrigid deformation are themselves 3D segmentation of the LV. To obtain the 2D segmentation of each SA image, we simply intersect it with the final meshes.

4.6 Experimental Results and Discussion

4.6.1 Data Description

To evaluate the proposed method, we have collected 20 sets of real patient data and generated 4 sets of simulated phantom data.

[1] As the endocardial and epicardial surfaces are generally smooth with small curvatures everywhere, we do not need the advanced adaptation and refinement algorithms in (Delingette, 1999) and only impose the uniform distribution of vertices via $\boldsymbol{F}_{\text{smooth}}$.

Table 4.1: Sequence parameters used in image acquisition.

	LGE	Cine
Flip angle [degree°]	25	55-74
Repetition / Echo time [ms]	650-1000 / 4.18	40.88-44.24 / 1.24-1.34
Bandwidth [Hz/pixel]	130	965
Width / Height[a] [pixel]	176-256	144-192
Pixel spacing[b] [mm]	1.1719-1.5625	1.5625-1.9792
Slice thickness / spacing[c] [mm]	7 / 3	7 / 3

[a] Both image width and height are within the same range.
[b] Pixel spacing is isotropic in-plane.
[c] Slice spacing represents the gap distance between adjacent SA slices.

4.6.1.1 Real patient data

We have collected 20 sets of real patient data (thereafter denoted by DAT_{1-20}) with varying amounts of infarcts for the evaluation. The data were acquired with ECG gating by a 1.5T Siemens Symphony MRI scanner from 20 patients (18 males and 2 females, 38-81 years old, mean age 52 ± 10) three months after myocardial infarction, following a bolus injection of gadolinium-based contrast agent. Table 4.1 shows the sequence parameters used for the data acquisition. Cine and LGE sequences of a same subject comprise the same number of SA slices with the same scan locations. Depending on the individual heart size, there can be 8-11 SA slices for a patient. In total there were 196 SA slices for all the 20 patients and 149 slices were selected for infarction analysis. Standard 4C and 2C LA views were acquired along with the SA views. While slices of a cine sequence comprise 25 frames, slices of an LGE sequence comprise only one frame.

The data were manually analyzed by two experts independently, and the manual contours (denoted by C_{man1} and C_{man2}) were used as the reference stan-

dards in our experiments. The expert who produced C_{man1} also supervised the production of the *a priori* segmentation in cine data and had full access to the cine data during his analysis of the LGE data, while the other had no access to the cine data. Moreover, the expert who produced C_{man1} further delineated the infarcts (denoted by S_{man1}) within the myocardium, while the other delineated only the myocardium. According to C_{man1} and S_{man1}, volumetric percentage of the infarcts with respect to the entire myocardium for the 20 patients ranges from 0 to 35.05% (two cases of non-infarct) with the mean and standard deviation of $18.60 \pm 10.43\%$, and five patients had MVO. Using the 16-segments division of the myocardium recommended by the AHA (Cerqueira *et al.*, 2002), 145 out of the total $16 \times 20 = 320$ segments (i.e., 45.31%) are infarcted, and the locality distribution of the infarctions is charted in Fig. 4.10.

4.6.1.2 Simulated data

We have also generated simulated data from the 4D extended cardiac-torso (XCAT) male phantom (Segars *et al.*, 2010) for the evaluation of our 3D segmentation method. The 4D XCAT phantom is a computer generated digital phantom containing highly detailed whole-body anatomies. Specially, it incorporates parameterized models of the cardiac and respiratory motions and hence is suitable for simulation of cardiac imaging. The LGE data are simulated as follows. First a voxelized torso phantom with an isotropic voxel size of 1.34 mm is generated from the XCAT. Nine tissues are included: the myocardium, infarct, blood, pericardium, lung, spleen, liver, stomach and the rest of the body. Then every voxel in the torso phantom is randomly assigned a value according to its tissue type. After that, simulated images of standard CMR orientations (SA, 4C

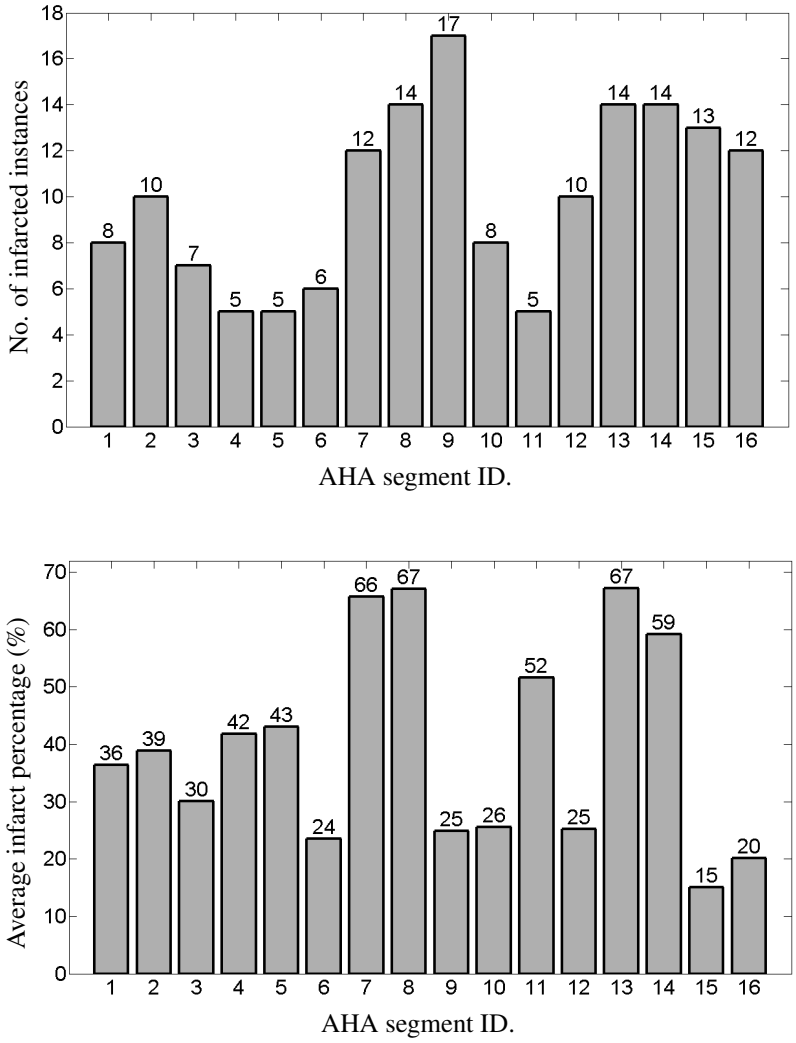

Figure 4.10: Locality distribution of the infarctions with respect to the AHA 16-segments division. Top: number of infarcted instances for each AHA segment (the total number of instances for each segment is 20). Bottom: average infarct percentage for each AHA segment, calculated with only infarcted instances.

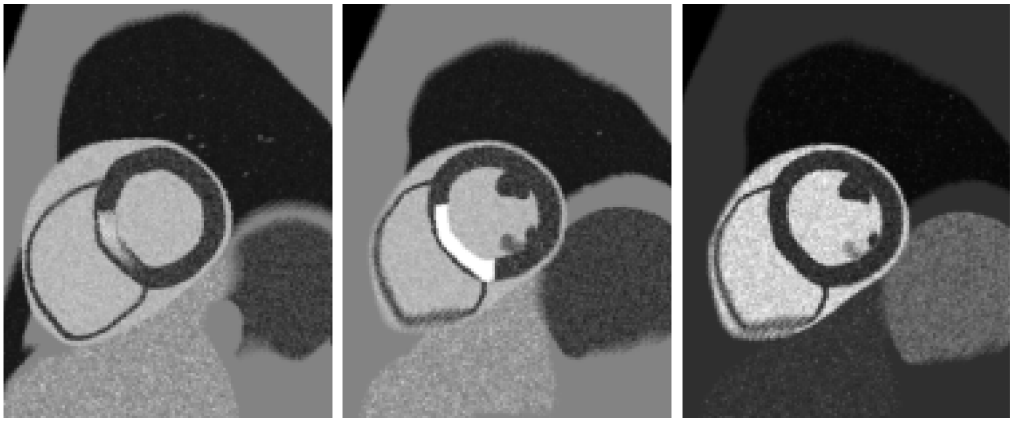

(a) (b) (c)

Figure 4.11: Examples of the simulated data: (a)-(b) LGE and (c) cine images.

and 2C) with the same slice dimensions as our real data (pixel spacing = 1.34 mm, slice thickness and spacing = 7 and 3 mm, resulting in 8 SA slices) are reconstructed from the torso volume. The cine data are simulated in the same way, except that no infarct is included. Figure 4.11 shows several examples of the simulated cine and LGE data.

To create enough difference in myocardium shape between the LGE and cine SA images, the LGE and cine data were simulated at different cardiac and respiratory phases. The infarcts were set at mid-ventricle, spanning 50 mm along the LA of the LV. Four LV volumes with infarcts located at anterior, lateral, inferior and septal walls respectively were simulated. The infarcts span 100 degrees on the myocardial circumference and are 100% transmural. Myocardial contours of the simulated data were derived from the original voxelized phantom. The cine contours are used as the *a priori* segmentation to our segmentation framework, while the LGE contours are used as the ground truth (C_{grnd}) for evaluation.

4.6.2 Quantitative Assessment of Accuracy

The accuracy of the proposed method is quantified through validation against the reference standard drawn by experts (in the case of real patient data) or the ground truth (in the case of simulated data). For this purpose, two metrics will be employed in the next few sections of this chapter.

- The Dice coefficient (Dice, 1945), abbreviated to DC afterwards, measures the overlapping rate of two regions:

$$\mathrm{DC}(R_1, R_2) = \frac{2|R_1 \bigcap R_2|}{|R_1| + |R_2|}, \tag{4.13}$$

  in which R_1 and R_2 can be in any dimension depending on the practical problem. The DC is known to be sensitive to small regions. It will be used to measure overlapping rates of the LV, BP and myocardium regions outlined in automatic results and the reference standard / ground truth.

- The mean distance error between two contours is computed as the mean perpendicular distance between them. As the perpendicular distance is actually the distance from a point on one of the contours to the other, it is also called the point-to-curve error (Petitjean & Dacher, 2011). Intuitively, the mean distance error can be used to assess accuracy of the segmentation contours.

4.6.3 Experimental Settings

In the experiments, various parameters are set as follows: (i) For the computation of PI in (4.1), $r = 5$ and $\delta = 0.1$. (ii) w_{d} and t_{d} in (4.3) are confined

within a narrow band of 7 pixels for SA images and 9 pixels for LA images centered at w_0 and t_0. (iii) For the energy function in (4.4), the weight λ is set 0.005 for both SA and LA images. (iv) For the 3D deformation scheme in (4.8), $\gamma = 0.7$, $\alpha = 0.3$, $\beta = 0.3$ and $\mu = 0.1$. (v) For the computation of $\boldsymbol{F}_{\text{edge}}$ in (4.9), $D_{\text{cutoff}} = 3$. We did not employ independent training and testing datasets because our method is not learning-based and we found it insensitive to small variations of the parameters.

In practice, we provide the functionality for manual adjustment over the automatic results in each step of the method. But to better evaluate the proposed method, minimum manual adjustments were performed in our experiments. Three SA slices (each from a different volume) were manually reallocated because of mis-registration by the misalignment correction method. Eight failures of translational registration were manually registered. No manual adjustments were performed on the final C_{auto}.

Although the final meshes produced by the 3D deformation scheme are already a 3D segmentation of the LV, we need to intersect them with the SA images to obtain corresponding 2D segmentation contours (denoted by C_{auto}), in order to compare with manual contours drawn by experts in 2D images.

4.6.4 Segmentation Accuracy

4.6.4.1 Results on real patient data

Qualitatively, we observe that segmentation results produced by the proposed method are consistently accurate for nearly all the LGE images in our database. Figure 4.12 shows some exemplary results, together with the manual contours

delineated by one of the experts (C_{man1}). Quantitatively, we have evaluated our method in terms of both distance- and region-based measures. We have calculated mean distance error and the DC between the automatic results and reference standards slice by slice. We have also calculated volumetric DCs. The results are presented in Table 4.2. Of the three groups of comparisons, C_{auto} and C_{man1} are the most similar with extremely small distances and high slice-wise and volumetric DCs. Although the difference between C_{auto} and C_{man2} is slightly larger, it is very close to the reported inter-observer variations between C_{man1} and C_{man2}. These results confirm that the myocardial segmentations produced by our method are close to those obtained by the experts.

Table 4.3 shows a comparison of the slice-wise mean distance errors of this thesis (C_{auto} versus C_{man1}), (Wei *et al.*, 2011) and (Ciofolo *et al.*, 2008). The algorithms proposed in (Wei *et al.*, 2011) were run with the same real patient data as described in this chapter, and the results were compared with C_{man1} to produce the mean distance errors. For (Ciofolo *et al.*, 2008), we simply use the *best results reported* by the authors. The comparison indicates that myocardial contours produced by our method proposed in this thesis are closest to manual delineations provided by experts, though with the caution that different data sets were used for evaluation in (Ciofolo *et al.*, 2008).

4.6.4.2 Results on simulated data

The segmentation results obtained by an expert and our method on the simulated LGE data are shown in Table 4.4. Both manual and automatic segmentations are very close to the ground truth, and the difference between the two segmentations is also small. What is noteworthy is the standard deviation of the slice-wise

Table 4.2: The segmentation accuracy evaluated with the real patient data. Shown in parentheses are the maximum mean distance errors and minimum DCs to indicate the worst cases.

	C_{man1} vs. C_{man2}	C_{auto} vs. C_{man1}	C_{auto} vs. C_{man2}
Mean distance error [mm]			
Endocardium	1.46±0.66	**0.94±0.44**	1.51±0.74
	(4.50)	(3.36)	(6.63)
Epicardium	1.56±0.58	**0.90±0.41**	1.68±0.70
	(3.76)	(3.52)	(4.99)
Both	1.46±0.47	**0.90±0.36**	1.54±0.56
	(3.44)	(3.14)	(4.71)
Slice-wise DC [%]			
LV	94.76±2.25	**96.88±1.84**	94.35±2.70
	(86.02)	(84.50)	(81.96)
BP	92.77±4.29	**95.33±3.62**	92.64±4.36
	(77.36)	(66.67)	(74.11)
Myocardium	82.93±5.28	**88.57±4.75**	82.32±5.59
	(62.27)	(60.23)	(63.25)
Volumetric DC [%]			
LV	95.06±0.91	**97.18±0.48**	94.78±0.88
	(92.69)	(95.95)	(92.52)
BP	93.65±1.47	**95.98±0.87**	93.42±1.96
	(90.37)	(93.37)	(87.74)
Myocardium	83.49±2.49	**89.19±1.42**	82.84±2.50
	(77.80)	(86.44)	(76.44)

Table 4.3: A comparison of the slice-wise mean distance errors (mm) of this thesis, (Wei *et al.*, 2011) and (Ciofolo *et al.*, 2008). N is the number of patients included for evaluation.

	N	Endocardium	Epicardium	Both
[a]This thesis	20	**0.94±0.44**	**0.90±0.41**	**0.90±0.36**
[b]Wei *et al.* (2011)	20	1.10±0.83	1.11±0.84	1.09±0.80
[c]Ciofolo *et al.* (2008)	23	2.00±0.40	1.90±0.70	–

[a] C_{auto} versus C_{man1}.

[b] The algorithms proposed in (Wei *et al.*, 2011) were run with the same data as described in Section 4.6.1.1, and the results were compared with C_{man1} to produce the mean distance errors.

[c] These are the *best results reported* in (Ciofolo *et al.*, 2008).

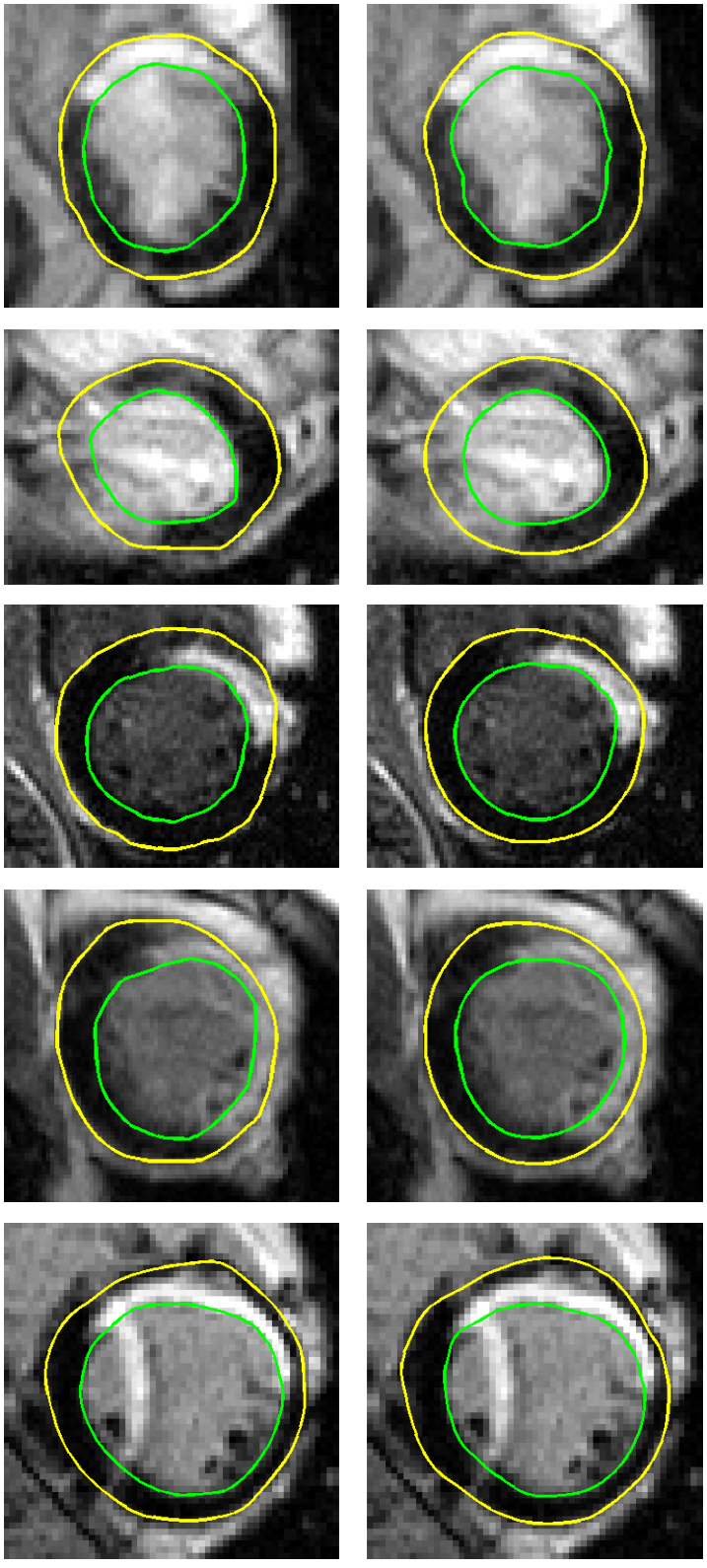

Figure 4.12: Some exemplary segmentation results of our automatic framework (C_{auto}, top row), as compared to those by one of the experts (C_{man1}, bottom row).

Table 4.4: The segmentation accuracy evaluated with the simulated data. Shown in parentheses are the maximum mean distance errors and minimum DCs to indicate the worst cases.

	C_{man1} vs. C_{grnd}	C_{auto} vs. C_{grnd}	C_{auto} vs. C_{man1}
Mean distance error [mm]			
Endocardium	**0.68±0.17**	0.73±0.49	0.71±0.34
	(1.19)	(2.26)	(1.89)
Epicardium	0.81±0.42	**0.67±0.41**	1.12±1.04
	(1.99)	(1.89)	(4.10)
Both	0.76±0.28	**0.69±0.44**	0.92±0.67
	(1.44)	(2.07)	(2.92)
Slice-wise DC [%]			
LV	95.78±4.70	**96.93±3.74**	94.22±8.42
	(81.18)	(86.38)	(69.38)
BP	**94.81±4.35**	92.86±11.20	93.79±8.32
	(81.48)	(59.83)	(64.96)
Myocardium	90.86±5.30	**92.73±5.51**	88.61±11.13
	(75.05)	(76.33)	(54.69)
Volumetric DC [%]			
LV	97.44±0.14	**98.05±0.07**	96.99±0.18
	(97.23)	(97.95)	(96.79)
BP	96.66±0.27	**97.00±0.19**	96.81±0.02
	(96.37)	(96.71)	(96.78)
Myocardium	92.58±0.50	**94.10±0.17**	91.80±0.42
	(91.85)	(93.91)	(91.31)

DCs for the BP between C_{auto} and C_{grnd}, which is obviously higher than the others. Correspondingly, relatively low DC values can be expected, such as the minimum DC at 59.83%.

4.6.5 Pattern Intensity versus Conventional Similarity Metrics

The quality of the translational registration is vital to our segmentation method, since the nonrigid mesh deformation requires the initial contours (i.e., $C_{\mathrm{endo,\,rigid}}$ and $C_{\mathrm{epi,\,rigid}}$) to be in the vicinity of the anatomical myocardial boundaries.

Table 4.5: Comparison of the translational registration results with different similarity metrics.

	PI	**NMI**	**MSD**	**NCC**
No. of failures	**8**	16	19	28
Successful rate [%]	**94.94**	89.87	87.97	82.28
Mean distance error [mm]				
Endocardium	**1.12±0.72**	1.26±0.80	1.34±0.78	1.48±0.84
Epicardium	**1.10±0.72**	1.25±0.76	1.32±0.80	1.44±0.87
Both	**1.10±0.69**	1.23±0.76	1.32±0.78	1.45±0.84
Slice-wise DC [%]				
LV	**96.08±3.59**	95.70±2.94	95.41±3.12	95.03±3.41
BP	**94.27±6.45**	93.78±4.97	93.47±4.69	92.85±4.99
Myocardium	**85.91±8.71**	84.11±9.61	83.04±9.93	81.47±11.02

Different from most registration methods, we use the PI as the similarity metric instead of conventional metrics. We have experimentally compared the registration results with different similarity metrics (including PI and the widely used MSD, NMI and NCC) from two aspects: success rate and accuracy. A registration is considered successful if the mean distances between the coarse endocardial and epicardial contours produced by the registration and the reference standard C_{man1} are smaller than 2 mm. For accuracy comparison, the metrics we use are mean distance error and the DC. All the 149 selected SA slices of the 20 subjects are used for the comparison and the results are summarized in Table 4.5. The results reveal that registration with PI has the highest success rate and accuracy.

4.6.6 Robustness with Respect to Different *A Priori* Segmentations

In order to test the consistency of the 3D segmentation method with different *a priori* segmentations, we have conducted two experiments with both practical and artificially simulated *a priori* segmentations, respectively. We select a set of LGE data with fair segmentation accuracy for the experiments, since our focus here is the consistency instead of accuracy.

Experiment 1: segmentation with different practical *a priori* segmentations. In this experiment, one observer manually drew the myocardial contours for the selected SA cine images that correspond to the target LGE images, serving as the manual *a priori* segmentation (denoted by A_{manu}). Meanwhile, the automatically generated cine contours used in Section 4.6.4.1 serve as the control group (denoted by A_{auto}). Segmentation accuracies with A_{manu} and A_{auto} as *a priori* are compared to test whether our segmentation method can produce consistently good results with both manually drawn and automatically generated *a priori* segmentations. The results are presented in Table 4.6. As we can see, the segmentation results with both kinds of inputs are similarly good, though the results produced with A_{manu} are slightly better. This indicates that our method can consistently produce high quality segmentation for LGE images despite that in practice the potential *a priori* segmentation in the corresponding cine images can be either manually drawn or (semi-) automatically generated.

Experiment 2: segmentation with different simulated *a priori* segmentations. In this experiment, A_{manu} is purposely enlarged and shrunk by 1 mm to generate two sets of artificially simulated *a priori* segmentations – A_{enlg} and

Table 4.6: Segmentation accuracies with different practical *a priori* segmentations (A_{auto} and A_{manu}). The reference standard used here was C_{man1}.

		A_{auto}	A_{manu}
Mean distance error [mm]	Endocardium	1.04±0.44	0.96±0.33
	Epicardium	1.19±0.32	1.08±0.26
	Both	1.12±0.29	1.02±0.18
Slice-wise DC [%]	LV	96.05±1.08	96.53±0.59
	BP	94.89±3.33	95.65±1.91
	Myocardium	86.18±3.76	87.84±2.73

Table 4.7: Comparisons between A_{enlg} and A_{shrk}, and between segmentation results with A_{enlg} and A_{shrk} as *a priori* segmentations.

		A_{enlg} vs. A_{shrk}	Results comparison
Mean distance [mm]	Endocardium	1.96±0.03	1.21±0.21
	Epicardium	1.98±0.01	1.12±0.24
	Both	1.97±0.02	1.16±0.22
Slice-wise DC [%]	LV	93.44±1.23	96.29±1.27
	BP	90.59±2.66	94.46±1.43
	Myocardium	77.24±2.96	87.03±4.03

A_{shrk}. Differences between segmentation results with A_{enlg} and A_{shrk} as *a priori* segmentations are examined to test the consistency of our segmentation method given the *a priori* segmentations 2 mm apart from each other. The comparison is presented in Table 4.7. Mean distances between the segmentation results are greatly decreased from the mean distances between the two *a priori* segmentations themselves. Area similarity is also improved, which is revealed by the fact that DCs evaluated at all three levels are significantly increased. The comparison results further validate the consistency of our segmentation method – it can produce consistent segmentations even with varied *a priori* segmentations in the range of 2 mm.

4.6.7 Discussion

4.6.7.1 Accuracy of the myocardium segmentation

On real patient data, both the qualitative and quantitative evaluations indicate that our 3D segmentation method can produce myocardial contours close to those obtained by the experts. The general trend that the difference between C_{auto} and C_{man1} is smaller than between C_{auto} and C_{man2} is not surprising, because the expert who produced C_{man1} also supervised the *a priori* segmentation of the cine data. On the contrary, the other expert had no such *a priori* knowledge and had to guess based on her experience when the contrast is poor.

On the simulated phantom data, both the manual and automatic segmentations are very close to the ground truth, and the difference between the two segmentations is also small. The automatic segmentation by our method is even closer to the ground truth sometimes (see Table 4.4), suggesting that manual segmentation may not always be optimal. We notice that the standard deviation of the slice-wise DCs for the BP between C_{auto} and C_{grnd} is relatively high. It is caused by the most apical slice in each volume and can be explained by three facts regarding very apical slices: (i) the myocardium is usually much blurred; (ii) the apex's motion is large and causes a big change between the myocardium shape in cine and LGE images; (iii) areas of the myocardium are small and the DC is known to be sensitive to small areas. In fact segmentation of the myocardium in very apical slices is always so difficult that no method can consistently produce reliable results. In practice, we provide a simple user correction scheme to effectively handle such cases. The mean DC for the BP between C_{auto} and C_{grnd} becomes $96.97 \pm 1.50\%$ if the most apical slice in each

volume is excluded.

4.6.7.2 Comparison with related works

It is difficult to quantitatively compare the accuracy of our 3D segmentation method with those of the existing methods (Ciofolo *et al.*, 2008; Dikici *et al.*, 2004). Given that different data sets and/or evaluation metrics were used, it is often inappropriate or sometimes even impossible to directly compare accuracies or errors reported in the papers. However, qualitatively we have identified the following advantages of our 3D segmentation method over others.

First, compared to pure 2D segmentation methods (Dikici *et al.*, 2004; Wei *et al.*, 2011) which merely produce discrete cylinders in 3D space (Fig. 4.13(a)), our 3D segmentation framework produces more accurate 3D reconstruction of the LV geometry (Fig. 4.13(b)). Moreover, the 3D smoothness force $\boldsymbol{F}_{\mathrm{smooth}}$ helps extrapolate reasonable myocardial boundaries with information from the LA and neighboring SA slices, when the current slice lacks contrast.

Second, though the work by Ciofolo *et al.* (2008) also involved deforming 3D meshes for segmentation, the meshes were attracted only to features detected in SA LGE images. Due to the large anisotropy of the stacks of SA images, a respectable portion of the vertices was moved by only regulating forces because there were no feature points lying between the SA slices (Fig. 4.14 (a)). In contrast, since we incorporate the two standard LA views (4C and 2C) into our 3D segmentation framework, a considerable amount of feature points detected in the LA images fill the gaps (Fig. 4.14 (b)). These extra feature points can make the final meshes represent the physical shape of the scanned LV with higher fidelity.

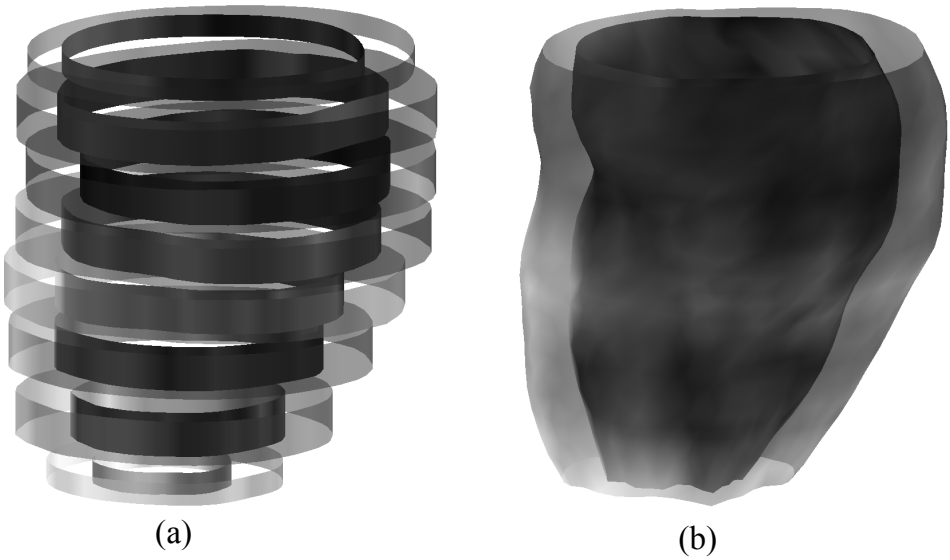

Figure 4.13: Qualitative comparison of 2D and 3D segmentation: (a) Pure 2D segmentation methods produce discrete cylinders in 3D space; (b) Our 3D segmentation achieves more accurate 3D reconstruction of the LV. Here epicardial surfaces are made transparent for visualization.

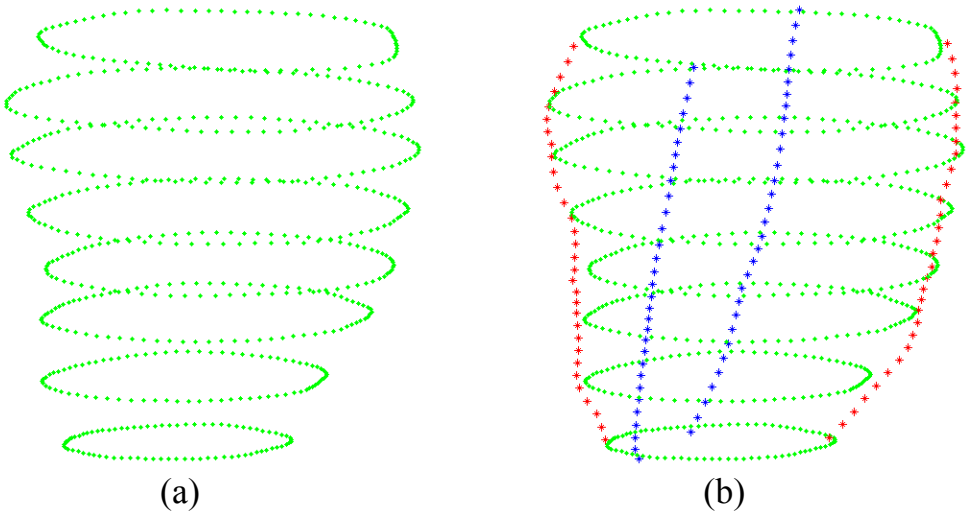

Figure 4.14: Detected epicardial edge points displayed in 3D: (a) only the SA images are used for the detection; (b) edge points from 4C (blue) and 2C (red) LA images are added, providing a considerable amount of extra information between the SA images.

Third, the work by Ciofolo *et al.* (2008) did not mention any correction of the misalignment artifacts for stacks of LGE images. This exposes the reconstructed 3D representation of the LV to potential distortion (McLeish *et al.*, 2002). In contrast, we realign all the SA and LA slices in the original patient coordinate system prior to the construction and deformation of the meshes, thus endowing the 3D segmentation with higher fidelity.

4.6.7.3 Appropriateness of the pattern intensity

Through the comparative experiment we find that PI outperforms the widely used similarity metrics including MSD, NMI and NCC for our translational registration. This is consistent with the findings from a comparative study of six similarity measures for intensity-based 2D-3D vertebra image registration (Penney *et al.*, 1998), which state that PI (together with gradient difference) outperformed the rest and was able to achieve accurate registration even when soft-tissue structures and interventional instruments were present as differences between the images.

In fact, PI's robustness with respect to the presence of the enhancements in LGE images (including infarcts and other enhanced tissues such as fat surrounding the heart) is theoretically supported by its design, especially its preference for regional homogeneity in the difference image, i.e., PI considers a pixel as a *structure* if the pixel differs greatly from its neighbors in the difference image. In the regions where there are enhancements, the homogenous interior pixels will also have homogeneous values in the difference image of the LGE and cine images. Small variations and noise are suppressed by the introduction of δ. Only the boundary pixels of these regions, which are just a small portion, differ

significantly from its neighbors in the difference image and are considered as registration errors. Due to its asymptotic nature PI is also robust to a few large differences. On the contrary, the entire enhancement regions are considered as registration errors by MSD, NMI and NCC.

To qualitatively demonstrate the superiority of PI as discussed above, a typical LGE image with a considerable amount of enhancements is selected. Given the rectangular ROI in the corresponding cine image (Fig. 4.15 (a); for definition of this ROI, please see Section 4.3, page 59), its best matching window in the LGE image is artificially found by observing how well the translated myocardial contours from the cine image outline the myocardium in the LGE image (Fig. 4.15 (b)). Then this best matching window is shifted around in the LGE image, ranging $[-16, 16]$ pixels in both x- and y-directions with a step size of unit pixel. For each shifted position, a *similarity* response between the current windowed LGE image and the ROI in the cine image can be calculated and by collecting responses at all shifted positions a similarity response map of size 33×33 can be generated (Fig. 4.15 (c)), with its center indicating no shift. A desirable similarity metric is thus expected to produce a strong and clean peak at the center of the map.

We have generated such similarity response maps with PI, NMI, MSD and NCC, respectively, and shown them in Figs. 4.15 (c)-(f). For a direct comparison, the responses in each map are scaled to $[0, 1]$ proportionally and color-mapped. Compared with the other three, the map generated with PI has a clear peak response right at its center without any local maximum, and more compact regions of hot colors for relatively strong responses around the peak. Surrounding colors in this map are also much cooler (indicating lower similarity

responses). In the maps generated with NMI, MSD and NCC, the maximum responses deviate from the center by $(2, 1)$, $(3, 0)$, and $(3, -1)$, respectively. Therefore we intuitively see that PI is more preferable than NMI, MSD and NCC for the specific problem.

4.6.7.4 Segmentation consistency

The experimental results have shown that our method can produce highly consistent segmentations despite that the given *a priori* segmentation in cine images can vary. The consistency and robustness are important and desirable because both inter-observer variability and automatic segmentation accuracies for cine images are in the range of 1-2 mm (Petitjean & Dacher, 2011). Although starting with propagating the *a priori* segmentation contours from cine images, the consistency of our segmentation framework makes it possible to obtain highly reproducible segmentation of LGE images given different *a priori* segmentations (either manual or automatic) in cine images.

4.6.7.5 Study limitations

The proposed method was evaluated with a small number of patients. To test full clinical capacity of the method, future experiments with a much larger cohort including both acute and chronic infarction patients are needed. Another limitation is that we did not use independent training and testing datasets in this work. Although the method is not learning based and insensitive to small fluctuations of the parameters, it would still be better to test the method with an independent testing set in future work.

We did not explicitly handle cases of signal intensity bias in the myocardium,

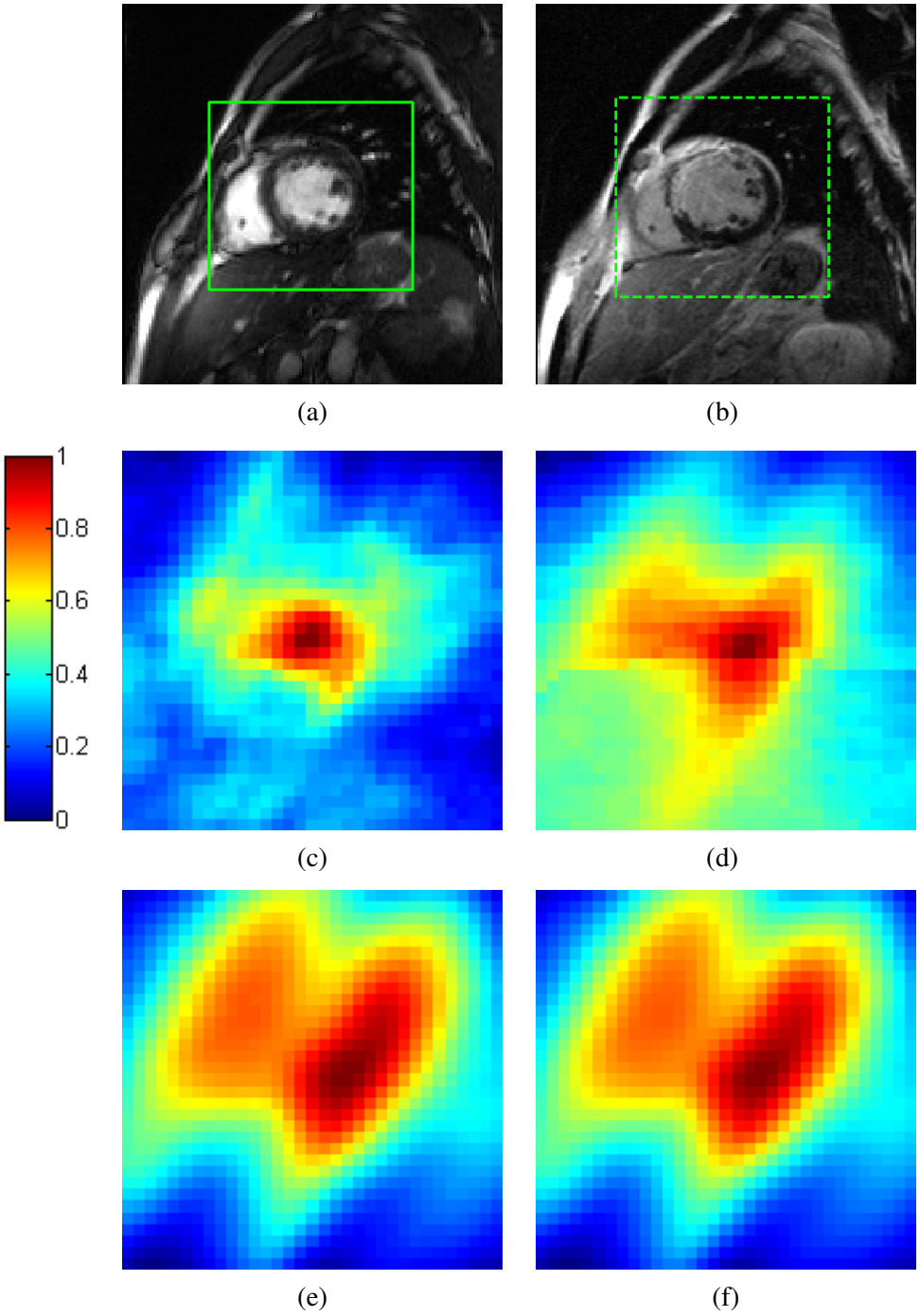

Figure 4.15: Similarity response maps. (a) A cine image with the registration ROI overlaid. (b) An LGE image with the registration matching window overlaid. By shifting the matching window in the LGE image around, similarity response maps are generated with (c) PI, (d) NMI, (e) MSD and (f) NCC, respectively. Also shown is a color bar indicating the color-mapping scheme.

such as imperfect inversion time, surface coil intensity drop off, or the existence of MR imaging artifacts. Such cases within a reasonable range are implicitly countered by the robustness of the framework. For example, the last column of Figure 4.12 shows an LGE slice in our database with a significant bright artifact and our framework still produced correct myocardial contours. However, severe cases that even cause troubles to human observers are considered imaging failures and beyond our scope. Lastly, we did not consider enhancements in the LGE images due to other pathologies, which may present complex enhancement patterns that are not covered by the proposed model. But the focus on a single pathology (i.e., ischemic heart disease) makes the framework more reliable for the target subject group.

Chapter 5

Infarct Classification and Quantification

This chapter describes subsequent processing steps after the myocardium is segmented in LGE CMR images. Section 5.1 presents our 3D method for infarct classification within the segmented myocardium. Section 5.2 introduces a quantification index commonly used by cardiologists to reflect the extent and severity of infarction. Experimental results of the infarct classification method are presented in Section 5.3. An overall evaluation of the entire quantification framework, incorporating both the segmentation and classification methods, is presented in Section 5.4.

5.1 Infarct Classification

In this section, we propose a 3D classification method that features the following advantages as compared with the aforementioned related works in Section 2.6:

(i) Crucial pre-processing measures are taken to correct both intensity inconsistency and misalignment artifacts across slices, which were omitted or improperly handled in previous works. (ii) No threshold is employed. Instead, the infarcted and normal myocardium are separated with a 3D graph-cut (Boykov & Jolly, 2001) algorithm combining the intensity distribution of the LV in LGE CMR images and spatial continuity of the infarcts and normal myocardium. (iii) It is a real 3D method since it utilizes the 3D intensity and spatial information all through the classification process.

The proposed method first performs pre-processing measures to correct intensity inconsistency and misalignment artifacts across images in a set of data. Based on the bimodal intensity distribution of the LV, it then classifies the myocardium into infarcted and normal regions with a 3D graph-cut algorithm. Followed is a post-processing procedure which removes false positives and negatives. After that, various infarct quantification indices can be calculated.

5.1.1 Pre-Processing

The two crucial pre-processing measures are the correction of misalignment artifacts and normalization of inconsistent intensities, which have already been described in detail in Section 3.1 and Section 3.2, respectively.

5.1.2 3D Graph-Cut

As mentioned in Section 2.6, infarct classification using a single threshold suffers from the lack of spatial continuity, resulting in many separated false positives probably due to noise or artifacts. To reduce this kind of false positives,

classification methods taking into account both the intensity and spatial information should be considered. We propose to use the graph-cut method as our major classification process. Compared to the level-set representation employed by Elagouni *et al.* (2010), the graph-cut formation can reach the global minimum of the proposed energy functional for a two-class segmentation problem. In our case, we need to segment the already delineated myocardium into infarcted and normal regions.

We employ the ND graph-cut algorithm proposed in (Boykov & Jolly, 2001) for our 3D classification of infarcts. Let p, q be any two different pixels in the image I and l_p the label assigned to p in a two-label system $l_p \in \{0, 1\}$, then a labeling set L of every pixel in I: $L = \{l_p \mid p \in I\}$ represents a segmentation of I. Based on the concept of maximum *a posteriori* estimate in a locally dependent Markov random field (Boykov *et al.*, 1998), the energy functional used by the graph-cut algorithm can be written as:

$$E_{\text{seg}}(L) = \eta \sum_{p \in I} - \ln Pr(i_p \mid l_p) + \sum_{p \in I} \sum_{q \in \mathcal{N}_p} V_{(p,q)}(l_p, l_q), \tag{5.1}$$

where $Pr(i_p \mid l_p)$ is the *relative* likelihood, $V_{(p,q)}$ a *clique potential*, $\mathcal{N}_p$ the set of all neighboring pixels of p, and η a positive weighting factor. The term $-\ln Pr(i_p \mid l_p)$ denotes the cost of assigning label l_p to the pixel p of intensity i_p, and $V_{(p,q)}(l_p, l_q)$ denotes the cost of assigning labels l_p and l_q, respectively, to the two neighboring pixels p and q.

The input to the graph-cut algorithm is just the segmented myocardium, that is, regions other than the myocardium are masked out to eliminate irrelevant information. Note that the input is a stack of 2D images, or, a 3D image. Since

there are only two allowable values for l_p, i.e., 1 for infarct and 0 for normal myocardium, $Pr(i_p \mid l_p)$ is defined as:

$$Pr(i_p \mid 1) = \begin{cases} Pr_{\mathrm{Gau}}(i_p), & \text{if} \quad i_p \leq \mu_G \\ 1, & \text{if} \quad i_p > \mu_G \end{cases} \tag{5.2}$$

$$Pr(i_p \mid 0) = \begin{cases} Pr_{\mathrm{Ray}}(i_p), & \text{if} \quad i_p \geq (\sigma_{\mathrm{R}} - a) \\ 1, & \text{if} \quad i_p < (\sigma_{\mathrm{R}} - a) \end{cases} \tag{5.3}$$

$Pr_{\mathrm{Gau}}(x)$ and $Pr_{\mathrm{Ray}}(x)$ are the Gaussian and Rayleigh parts of the fitted Rician distribution in (3.4), Section 3.2.1. The two special cases – $Pr(i_p \mid 1) = 1$ for i_p larger than μ_G and $Pr(i_p \mid 0) = 1$ for i_p smaller than $(\sigma_{\mathrm{R}} - a)$ – conforms to the clinical experience that a pixel brighter than the mode of the Gaussian distribution must be given the infarct label 1 and one darker than the mode of the Rayleigh distribution must be given the myocardium label 0. In these cases, there should be no cost on the corresponding labelings, which is embodied by the fact that the logarithm of 1 is 0.

For the interaction potential $V_{(p,q)}$, we also use the one proposed by Boykov & Jolly (2001):

$$V_{(p,q)} = \exp\left[-\frac{(i_p - i_q)^2}{2\sigma^2}\right] \cdot \frac{1}{\mathrm{dist}(p,q)} \cdot [1 - \delta(l_p - l_q)], \tag{5.4}$$

where σ is a constant, $\mathrm{dist}(p,q)$ the Euclidean distance between p and q, and

$\delta(x)$ the Dirac delta function:

$$\delta(x) = \begin{cases} 1, \text{ if } x = 0, \\ 0, \text{ otherwise.} \end{cases} \tag{5.5}$$

If p and q have the same label, i.e., $l_p = l_q$, then $V_{(p,q)} = 0$ and there is no interaction cost between p and q. Therefore, $V_{(p,q)}$ only penalizes neighboring pixels for having different labels. The constant σ controls the effective range of the potential well: when $|i_p - i_q| > \sigma$ the penalty is small and when $|i_p - i_q| < \sigma$ the penalty is large. This is intuitive since the intensity difference at object boundaries is often large. We set $\sigma = \mu_G - (\sigma_{\mathrm{R}} - a)$, which is the distance between the modes of $Pr_{\mathrm{Ray}}(x)$ and $Pr_{\mathrm{Gau}}(x)$.

$E_{\mathrm{seg}}(L)$ is minimized with the efficient α-expansion algorithm (Boykov *et al.*, 1999). Since only two labels are involved in our specific problem, the exact global minimum of $E_{\mathrm{seg}}(L)$ can be reached (Greig *et al.*, 1989; Kolmogorov & Zabin, 2004). As for the definition of $\mathcal{N}_p$, we use the 6-connected neighborhood. η is set to 1 at all times. Exemplary infarct classification results obtained by the 3D graph-cut method can be seen in Fig. 5.1(b) and Fig. 5.2(b).

5.1.3 Post-Processing

The post-processing steps include false positive / negative removal (Tao *et al.*, 2010) and MVO inclusion.

The false positives in infarct classification are usually caused by inclusion of thin layers of ventricular blood or epicardial fats inside the myocardial contours (Fig. 5.1(b)). This kind of contour tracing flaws are inevitable for both manual

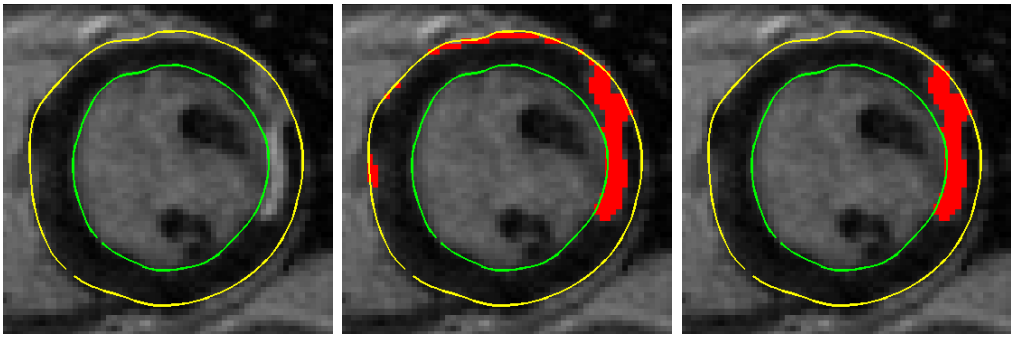

(a) (b) (c)

Figure 5.1: Illustration of the false positive removal: (a) an LGE image with myocardial contours overlaid; (b) epicardial false positives before removal; (c) after false positive removal with post-processing.

and (semi-) automatic delineations. Sometimes patches of artifacts within the myocardium are another source of false positive. Removal of the false positives is based on a 3D connected component analysis of the potential infarcts given by the graph-cut optimization in all SA slices of an LV volume. We exclude false positives according to the following criteria: (i) Only the two largest components are kept for further analysis, since it is rare for CAD patients to have multiple separated infarctions. (ii) Components that are too small (e.g., with fewer than 55 voxels) are excluded, considered as noise or bright artifacts. (iii) Thin layers of bright regions attached to the endocardium or epicardium are excluded (e.g., the proportion of myocardial boundary voxels in the entire component is larger than two thirds), considered as inaccurate myocardium delineation. (iv) Single-slice components are excluded. Figure 5.1 shows the effect of the false positive removal with an example LGE image.

False negatives may occur at regions with intermediate intensities (Fig. 5.2(b)), which are caused by the partial volume effect, i.e., mixing of infarcted and normal myocardium. It is also necessary to remove these false negatives via post

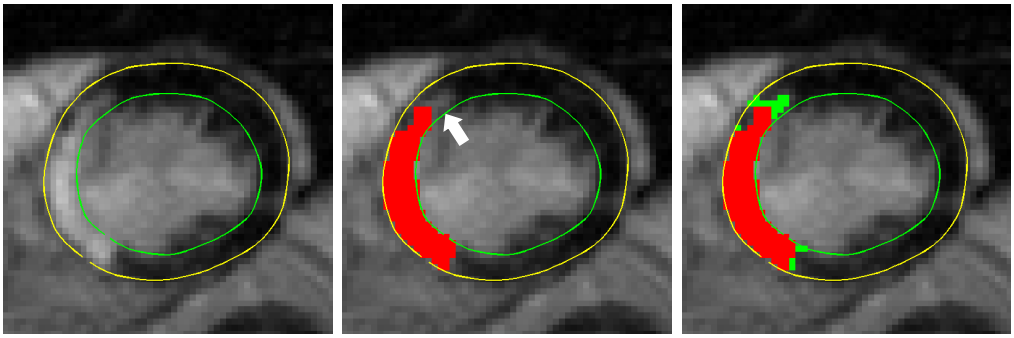

(a) (b) (c)

Figure 5.2: Illustration of the false negative removal: (a) an LGE image with myocardial contours overlaid; (b) a region of obvious false negative is pointed with a white arrow; (c) after false negative removal with post-processing – the recovered false negatives are highlighted in green.

processing. We use the following criteria to recover these misclassified infarcts: (i) the false negative should be peri-infarct regions; (ii) it should have intensity higher than 2 standard deviations above the mean of the normal myocardium (Kolipaka *et al.*, 2005; Yan *et al.*, 2006). As such, a region growing (Gonzalez & Woods, 2008, Section 10.4.1) with the already confirmed infarcts as seeds is suitable for this purpose. The standard deviation and mean of the normal myocardium are determined with the identified normal myocardium in the existing classification. As in (Tao *et al.*, 2010), the region growing is conducted per slice since the distance between contiguous SA slices is relatively big. Figure 5.2 illustrates the effect of the false negative removal with an example LGE image.

Finally, in order to also include MVOs which despite appearing dark are indeed non-viable (Fig. 5.3(b)), sub-endocardial dark blobs surrounded by hyper-enhanced infarcts are located and classified as infarcts as well. For implementation, we generate masks of the classified infarcts (M_{infr}) and BP (M_{BP}), obtain their union by $M_{\text{total}} = M_{\text{infr}} \cup M_{\text{BP}}$, and then fill holes in M_{total}. Besides

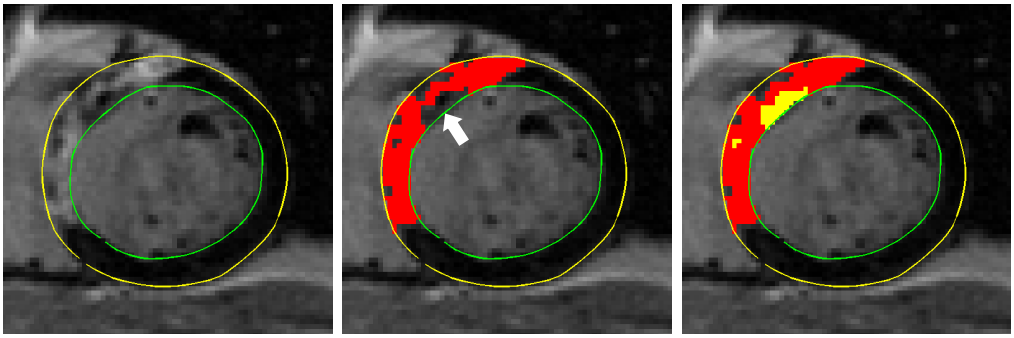

(a) (b) (c)

Figure 5.3: Illustration of the MVO inclusion: (a) an LGE image with myocardial contours overlaid; (b) the MVO region is pointed with a white arrow; (c) the MVO is located and highlighted in yellow. Besides the MVO, holes within the classified infarcts, which are possibly due to image noise, are also filled.

the MVO, holes within the classified infarcts, which are possibly due to image noise, are also filled in this way. The effect of the MVO inclusion is illustrated in Fig. 5.3.

5.2 Infarct Quantification

Various indices are used for infarct quantification in the literature, such as the infarct transmurality (Elagouni *et al.*, 2010) and absolute infarct area / volume / mass (Tao *et al.*, 2010; Valindria *et al.*, 2011). Specially, the percentage of the infarcts with respect to the entire myocardium (thereafter denoted by I/M%) is intuitively used by cardiologists to reflect the extent and severity of infarction:

$$\text{I/M\%} = \frac{\text{Size of the infarcts}}{\text{Total size of the myocardium}}. \tag{5.6}$$

Compared to the absolute infarct measurements (area / volume / mass), I/M% is a quantitative index independent of variable individual heart size. I/M% can be

calculated at different levels, such as per LV volume or per AHA standard segment. While a volumetric I/M% provides an overall evaluation of the patient's infarction severity, AHA segment-wise I/M%'s can help identify potential coronary arteries that are occluded and have caused the infarction. But we should note that despite being more sensitive, smaller quantification unit also raises the requirement on accuracy and reliability of the automatic infarct segmentation.

5.3 Experimental Evaluation of Infarct Classification Method

5.3.1 Experimental Settings

The experimental data used in this chapter are the same *real patient* data as described in Section 4.6.1.1, page 78. To evaluate the classification of infarcts alone without being affected by the quality of the myocardium segmentation, we use the manual myocardial contours C_{man1} as inputs to our infarct classification method in this section. As we have found through preliminary experiments that the classification method is insensitive to small variations in the weight η in (5.1), η is simply set to 1 empirically in all the experiments.

For quantitative assessment of accuracy, the Dice coefficient (DC), introduced in Section 4.6.2, page 82, is employed again to measure overlapping rates of the infarcted regions classified automatically and manually (i.e., S_{man1}). Besides the DC, the Bland-Altman (BA) plot (Bland & Altman, 1986), or analysis, is employed in this chapter as well. It is a statistical method assessing agreement between two methods of clinical measurement, which plots the dif-

ferences between the two measurements against their mean. If we denote the mean difference by $\bar{d}$ and the standard deviation of the differences by s, then $\bar{d} - 2s$ and $\bar{d} + 2s$ are referred to as the "limits of agreement". A BA plot with a near-zero mean difference and narrow limits of agreement indicates a strong agreement. The BA analysis is used to measure the agreement between the infarct percentages (I/M%) calculated with the automatic and manual infarct classification results. Due to its high sensitivity to small-sized subjects, the DC is only analyzed at the LV volume level. In contrast, I/M% is analyzed at both the LV volume and AHA myocardial segment levels.

5.3.2 Results

Qualitatively we observe that our method is able to correctly classify infarcts and normal myocardium as compared to the manual classification results S_{man1} by the expert. Figure 5.4 show the automatic (the third row) and manual (the fourth row) classification results, respectively, on 8 consecutive SA images of a set of LGE data. Also shown in Fig. 5.4 are the intermediate results after the 3D graph-cut but before the post-processing (the second row).

5.3.2.1 Volumetric analysis

Of the 20 sets of data, 2 sets present no infarct after three months' recovery since the heart attack and our method correctly reported zero infarct. The average DC for the other 18 sets of data is $89.97 \pm 2.28\%$, with the minimum and maximum values of 85.97% and 94.03%, respectively. Table 5.1 shows a comparison of the volumetric DCs by our method with the *best results reported* in (Tao *et al.*,

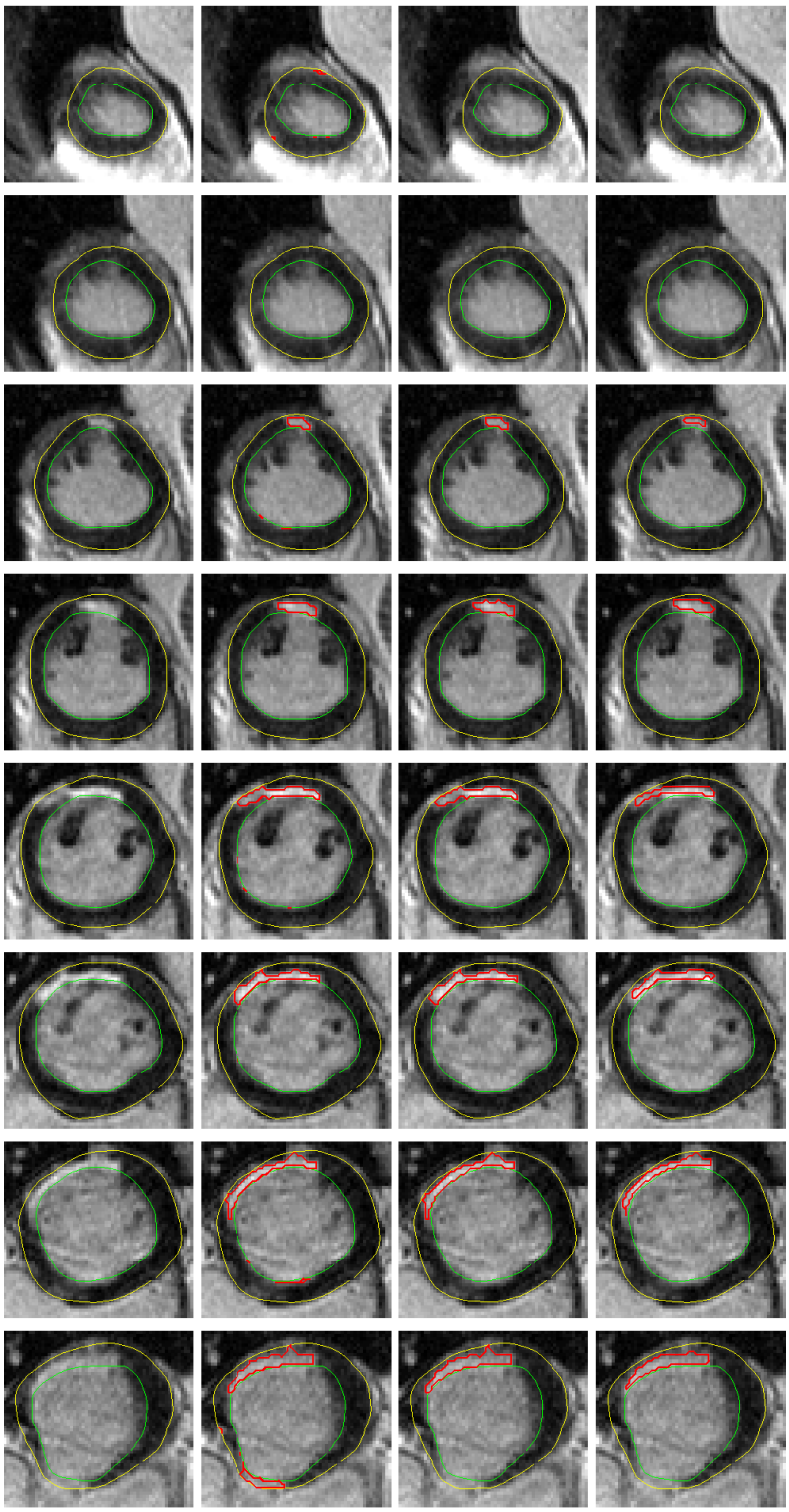

Figure 5.4: Exemplary segmentation results. First row: the original images to be classified with myocardial contours overlaid. Second row: intermediate classification results after the graph-cut minimization; there are some noticeable false acceptances. Third row: final classification results after minor post-processing. Fourth row: the reference standard manually drawn by the expert, shown as comparison.

Table 5.1: The volumetric DCs by our method versus the *best results reported* in (Tao *et al.*, 2010). N is the number of LV volumes (i.e., number of patients) included for evaluation.

	N	Mean	Min	Max
This thesis	18	**0.90±0.02**	**0.86**	0.94
Tao *et al.* (2010)	20	0.83±0.07	0.68	0.94

2010). It can be seen that our method greatly exceeded the related work in average and minimum DCs, though with the caution that different data sets were used for evaluation. Figure 5.5 top shows the BA plot of the volumetric I/M% (automatic minus manual results). The BA analysis indicates that the automatic results report slightly higher percentages of infarcts than the manual results with a mean difference of $0.58 \pm 2.21\%$. Furthermore, a Wilcoxon rank sum test indicates no significant difference between respective I/M% ($P = 0.71$).

5.3.2.2 Segment-wise analysis

As in the AHA statement (Cerqueira *et al.*, 2002) the segments are standardized with assignments to coronary arterial territories, examining segment-wise infarct presence can help identify the correlated vessel that is potentially occluded. For easy visual interpretation, I/M%'s of the 16 segments are plotted together in color-coded bull's-eye plots (Fig. 5.6).

Compared to the LV volume-wise analysis, segment-wise analysis is more sensitive and expected to reveal more insights due to the employment of location-specific smaller volumes. The BA analysis with all the $20 \times 16 = 320$ segments (Fig. 5.5 bottom) indicates that overall the automatic results report slightly higher I/M% than the manual results, with a mean difference of $0.74 \pm 5.19\%$ ($P = 0.93$). While the data points look compact around the zero level line at the

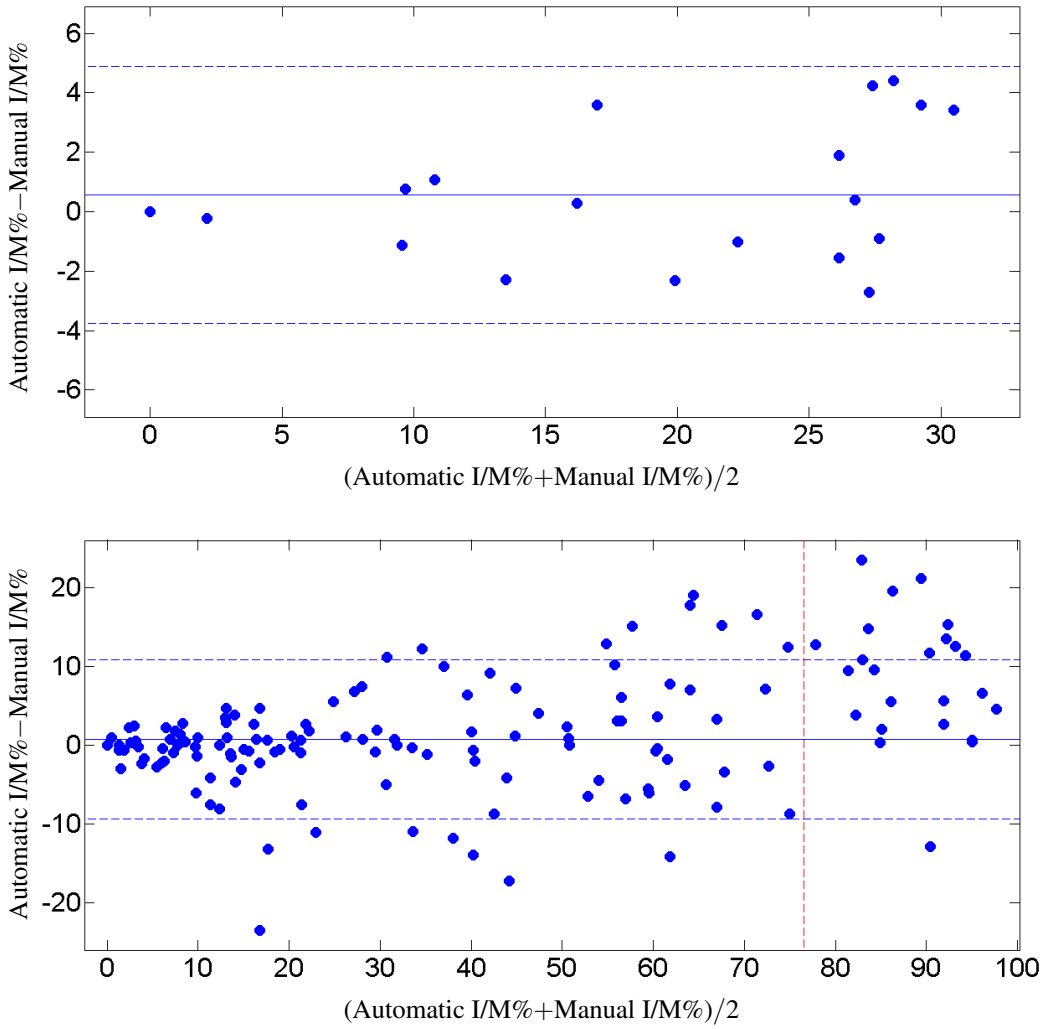

Figure 5.5: Bland-Altman plots of volumetric (top) and AHA segment-wise (bottom) I/M%, for evaluation of the 3D classification method.

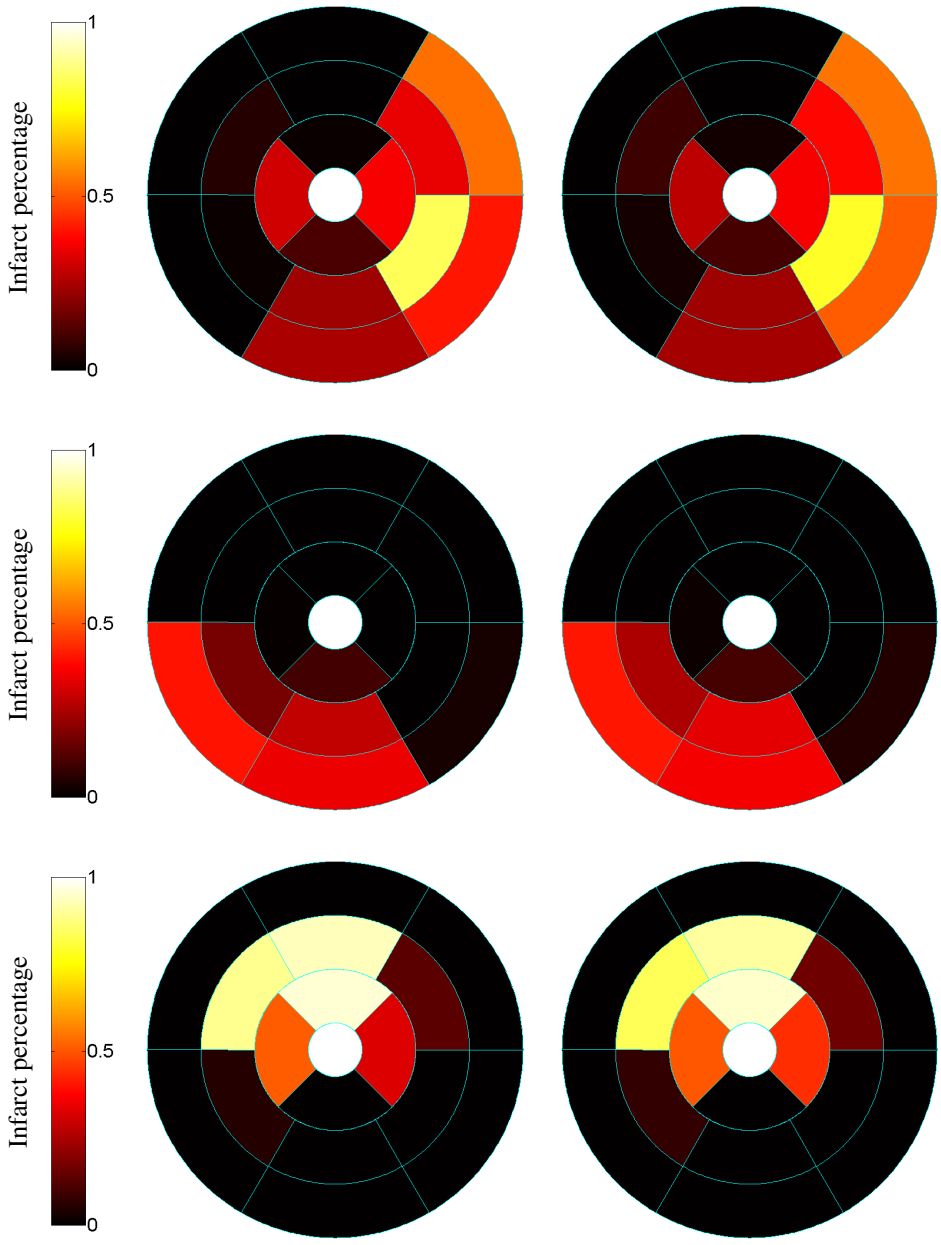

Figure 5.6: Bull's-eye plots of I/M%'s in standardized 16 segments (each row represents a different set of LGE data): (a) the automatic results; (b) the manual results. The extent of infarction is coded by the hot map.

smaller end of average I/M%, the automatic results tend to report considerably more infarcts than the manual results when the average I/M% is larger than 76.5% (see the red dashed line in Fig. 5.5 bottom).

Of the 320 segments, 144 segments are deemed infarcted and 175 segments deemed free of infarct by both results. No false positive (i.e., the manual results reported zero while the automatic results reported positive I/M%) exists. One false negative (i.e., the manual results reported positive while the automatic results reported zero I/M%) is found with a very small value: -3.03%. We have also examined absolute differences between I/M% calculated from the automatic and manual results at different slice levels: basal (Seg_{1-6}), mid (Seg_{7-12}) and apical (Seg_{13-16}). Although a multiple comparison following a Kruskal-Wallis test indicates that the absolute differences at the mid and apical levels are significantly larger than at the basal level ($P \ll 0.05$), the values are in fact quite small for all the three levels: $1.52 \pm 3.80\%$, $2.79 \pm 5.03\%$ and $3.51 \pm 4.84\%$ for the basal, mid and apical levels, respectively.

5.3.3 3D versus 2D Classification

For 2D classification of infarcts, we applied the method presented in Section 5.1.2 to one slice at a time without the volumetric correction of intensity inconsistencies. Also, the post processing took place in 2D. As the 2D classification works slice-wisely, naturally we compare the results at the slice level. The comparison is shown in Table 5.2. The classification results of our 3D framework significantly excel those of the 2D methods in three of the four compared aspects, and are equally good in the last.

Table 5.2: 3D versus 2D classification. Note: the DCs were calculated with slices deemed infarcted by all manual, 2D and 3D results ($N = 104$).

	2D	3D	p-value
DC (%)	86.05 ± 10.54	$\mathbf{88.81 \pm 7.26}$	0.04
Absolute diff. in I/M%	4.33 ± 6.27	$\mathbf{2.56 \pm 3.23}$	0.01
No. false positives	11	**2**	–
No. false negatives	0	0	–

5.3.4 Discussion

5.3.4.1 Accuracy and applicability of the method

The experimental results on the basis of LV volumes shows that our classification method can produce highly accurate evaluation of the overall extent and severity of infarction for a patient. The average DC of the infarcts classified by the method and the expert given the same myocardial contours is $89.97 \pm 2.28\%$, with the minimum DC of 85.97%. The volumetric BA analysis reports a small mean difference in I/M% with narrow limits of agreement: $0.58 \pm 2.21\%$, with the extreme differences of -2.72% and 4.41%. When examined at the AHA segment level, the mean difference in I/M% is also quite small: $0.74 \pm 5.19\%$. Although the automatic results tend to report higher percentages of infarcts than the manual results when average of the automatic and manual I/M%'s is beyond 76.5%, it is not an issue since true I/M%'s in such cases are already quite large and the overestimated results by our method will only cause more attention to the severe infarction status, instead of harmfully overlooking them. Meanwhile, we find no significant false positives or negatives in the segment-wise evaluation – the only false negative is -3.03%. Hence generally speaking, our classification method is promising for both LV volumewise and segment-vise analysis.

5.3.4.2 Advantages of 3D classification

In the comparative study, the 3D classification fully outperforms a 2D implementation of the same method applied to individual slices. The performance difference could be due to two reasons: (i) the utilization of 3D spatial continuity and (ii) the normalization of inconsistent intensities across SA slices in an LGE dataset.

5.4 Experimental Evaluation of Entire Quantification Framework

5.4.1 Experimental Settings

In this section, we evaluate the entire quantification framework, comprising both the myocardium segmentation and infarct classification methods. The experimental data used are the same *real patient* data as described in Section 4.6.1.1, page 78. *A priori* segmentations in cine data are input to the framework and the final quantification results of the LGE data are compared to those with C_{man1} and S_{man1}. Various weights and parameters are set the same as in the preceding sections. Again, the I/M% and DC are employed for quantitative evaluation. The DC is only analyzed at the LV volume level, while I/M% is analyzed at both the LV volume and AHA myocardial segment levels. I/M% calculated from the manual and automatic results are compared by the BA analysis.

5.4.2 Results

Figure 5.7 shows the automatic and manual results on three LGE images with different extents of infarction and different intensities. Qualitatively we find that our framework consistently produces myocardial and infarct segmentations close to those by the experts, though several exceptions of failed cases are found in few very apical slices (e.g., the slice shown in Fig. 5.9).

5.4.2.1 Volumetric analysis

The framework has no problem with the two cases of non-infarct. The average DC for the other 18 sets of data is $80.90 \pm 5.04\%$, with the minimum and maximum values of 67.23% and 88.25%, respectively. Figure 5.8 top shows the BA plot of the volumetric I/M% (automatic minus manual results). The BA analysis indicates that the automatic results report slightly higher percentages of infarcts than the manual results with a mean difference of $0.14 \pm 3.07\%$. Furthermore, a Wilcoxon rank sum test indicates no significant difference between respective I/M% ($P = 0.95$).

5.4.2.2 Segment-wise analysis

The BA analysis with all the 320 segments (Fig. 5.8 bottom) indicates that overall the automatic results report slightly higher I/M% than the manual results, with a mean difference of $0.66 \pm 6.68\%$ ($P = 0.99$). While the data points look compact around the zero level line at the smaller end of average I/M%, the automatic results tend to report considerably more infarcts than the manual results when the average I/M% is larger than 75% (see the red dashed line in Fig. 5.8

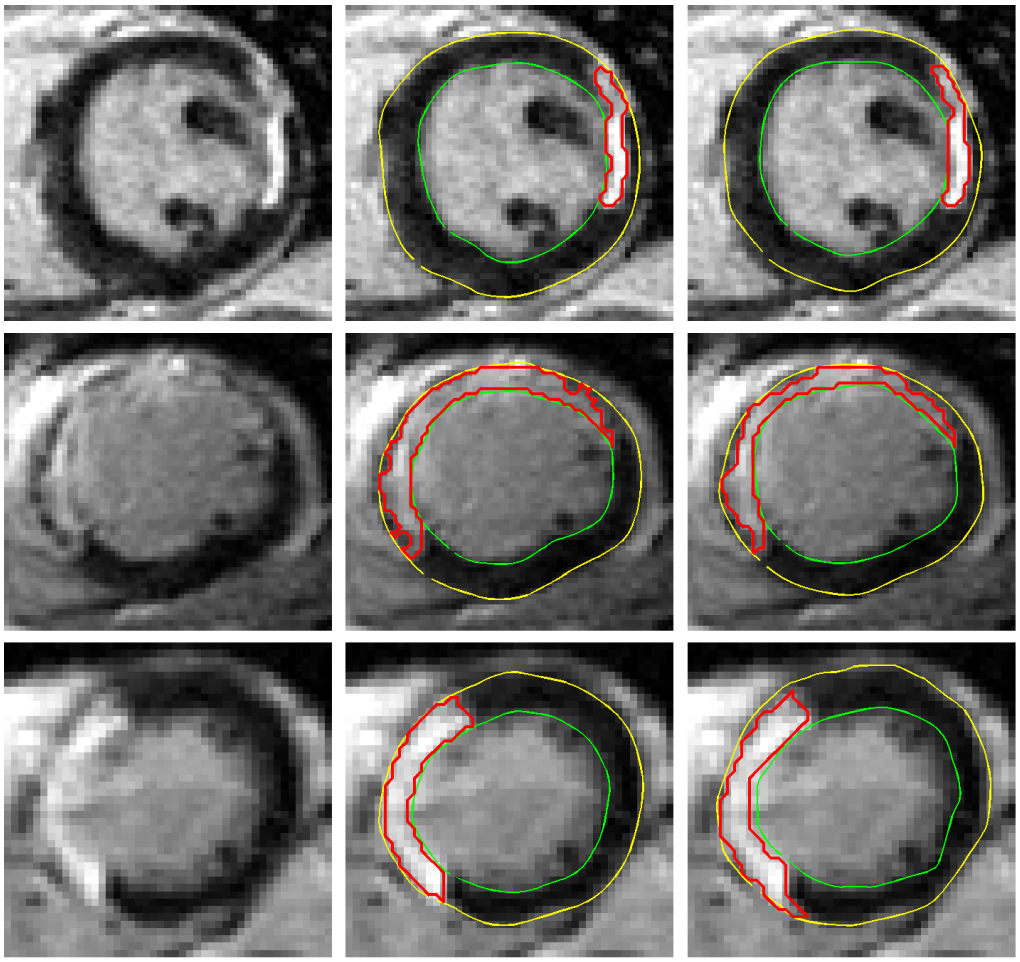

(a) (b) (c)

Figure 5.7: Exemplary results (each row shows a slice from a different subject): (a) the original image; (b) the proposed framework; (c) the reference standard. The green and yellow contours delineate the endocardium and epicardium respectively, and the red contours delineate the infarcts.

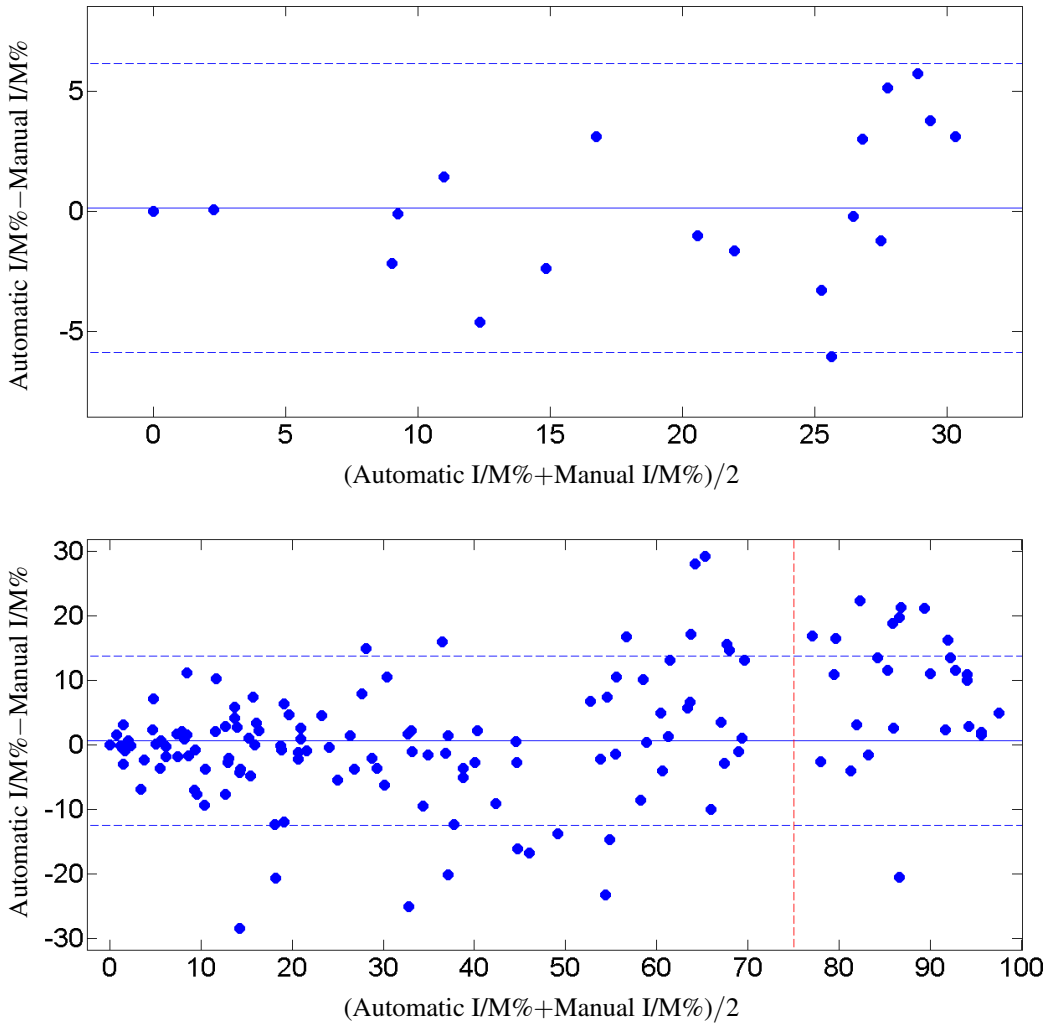

Figure 5.8: Bland-Altman plots of volumetric (top) and AHA segment-wise (bottom) I/M%, for evaluation of the entire quantification framework.

bottom).

Of the 320 segments, 142 segments are deemed infarcted and 173 segments deemed free of infarct by both results. Two false positives are found with very small values: 3.06% and 1.56%, respectively. Meanwhile, three false negatives are found and they are: -3.03%, -28.49% and -6.82%. We have also compared absolute differences between I/M% calculated from the automatic and manual results at different slice levels: basal (Seg_{1-6}), mid (Seg_{7-12}) and apical (Seg_{13-16}). The multiple comparison following a Kruskal-Wallis test indicates that while there is no significant difference between basal ($2.14 \pm 5.21\%$) and mid ($3.12 \pm 5.47\%$) levels, the absolute differences at the apical level ($5.12 \pm 6.94\%$) are significantly larger than both of the basal and mid levels ($P \ll 0.05$).

5.4.3 3D versus 2D Quantification

For 2D segmentation of the myocardium, we employed the method proposed in (Wei *et al.*, 2011). Validated against C_{man1} on the 20 sets of real patient data, the mean distance error of the 2D segmentation method is 1.09 ± 0.80 mm, and the DC for the myocardium is $85.84 \pm 9.86\%$. For 2D classification of infarcts, we applied the method presented in Section 5.1.2 to one slice at a time without the volumetric correction of intensity inconsistency. Also, the post processing took place in 2D. As the 2D quantification works slice-wisely, naturally we compare the quantification results at the slice level. The comparison is shown in Table 5.3. The quantification results of our 3D framework are significantly better than those of the 2D methods in three of the four compared aspects, and equally good in the last.

Table 5.3: 3D versus 2D quantifications. Note: the DCs were calculated with slices deemed infarcted by all manual, 2D and 3D results ($N = 102$).

	2D	3D	p-value
DC (%)	73.09 ± 16.17	$\mathbf{79.11 \pm 15.50}$	$\ll 0.05$
Absolute diff. in I/M%	5.64 ± 6.54	$\mathbf{3.56 \pm 5.04}$	0.01
No. false positives	13	**3**	–
No. false negatives	1	1	–

5.4.4 Discussion

5.4.4.1 Accuracy and applicability of the framework

Experimental results on the basis of LV volumes indicate that our framework is capable of producing a reliable evaluation of the overall extent and severity of infarction for a patient. The volumetric BA analysis reports an almost zero mean discrepancy (0.14%) between the percentages of infarcts derived from the automatic and manual results with very narrow limits of agreement ($SD = 3.07\%$). The volumetric DCs also suggest that the automatic and manual results largely agree with each other (mean DC $= 80.90 \pm 5.04\%$). However, we should be cautious when applying the framework to evaluate the extent of infarction in each AHA segment and identify potential supplying arteries of stenosis. Special attention should be paid to quantification results of segments in the apical level, i.e., Seg_{13-16}, since the Kruskal-Wallis test with the slice levels as the factor indicates that discrepancies between the automatic and manual results are significantly larger at the apical level than at the basal and mid levels ($5.12 \pm 6.94\%$ versus $2.14 \pm 5.21\%$ and $3.12 \pm 5.47\%$). Further, the only significant false negative (-28.49%) out of the five cases of false errors is Seg_{15} of DAT_5. Therefore, the framework can still be applied to segment-wise quantification of infarcts

if careful attention is paid to apical segments and proper correction schemes (where necessary) are provided.

5.4.4.2 Implications

As mentioned, we find that discrepancies between the automatic and manual results are significantly larger at the apical level than at the basal and mid levels. This may be due to two reasons: (i) Our framework tends to report considerably higher infarct percentages than the human observers when there are a large amount of infarcts. Naturally there are significantly more infarcts at the apical than at the other two levels in real patients (Kolipaka *et al.*, 2005), so our framework tends to report more infarcts for apical segments. (ii) Automatic segmentation of the myocardium in apical slices is difficult, and myocardial contours of very poor quality cause failures anyway despite the good performance of the subsequent infarct classification method. Such cases are illustrated in Fig. 5.9 with the most apical slice in DAT_5. This failure occurs because our method utilizes myocardial contours in corresponding cine CMR images as the *a priori* knowledge to guide the segmentation in LGE images. When there is a large change in myocardium shape between corresponding cine and LGE images, the method may not be able to compensate and the segmentation fails. Due to the use of ECG gating, such severe changes only happen at the extremely apical slices, where the LV is small and the apex's motion is large. In fact the segmentation of the myocardium at apical slices is always so difficult that no method can consistently produce reliable segmentations. Therefore, a user-correction scheme should be provided to handle such cases.

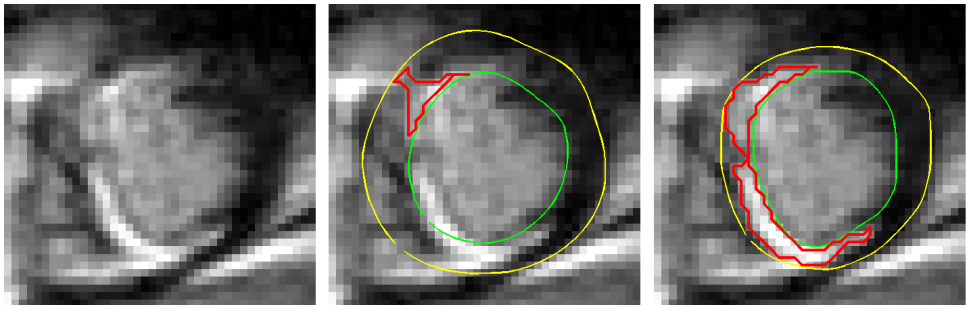

(a) (b) (c)

Figure 5.9: The most apical slice in DAT_5: (a) the original LGE image; (b) the automatic result; (c) the manual result. The incorrect classification of infarcts is caused by the failed automatic segmentation of the myocardium.

5.4.4.3 Advantages of 3D quantification

The experimental results show that our 3D quantification framework outperform the 2D methods in the control group in three of the four examined aspects and has the same good performance in the last. There are two reasons for this. First, the myocardial contours produced by our 3D segmentation method is more accurate than those by the 2D method. Second, due to the utilization of 3D spatial and intensity information in a stack of SA slices, the 3D classification of infarcts is also better than a 2D application of the same method to individual slices (see Table 5.2).

5.4.4.4 Implementation and speed optimization

The entire quantification framework, including the segmentation and classification methods, and the distortion correction methods, is implemented under the MATLAB R2011a environment, on a PC with Intel Core2 Duo T9400 processer, 3 GB RAM and running 32-bit Microsoft Windows 7 OS. Optimization of E_{align} and fitting of $Rcn(x)$ are achieved with the Optimization Toolbox and Curve Fit-

Table 5.4: Average running times of key steps in the quantification framework.

	Time
Misalignment correction	26 s
Myocardium segmentation	
Translational registration	23 s
Feature points detection	110 s
Mesh construction & deformation	0.5 s
Infarct classification	1.5 s

ting Toolbox of MATLAB R2011a, respectively. Average running times of key steps in the framework are shown in Table 5.4. The running times can be significantly reduced if the proposed framework is implemented in a more efficient programming language with multi-threading enabled. For example, by implementing in C++ the overall speed of the framework can be boosted. Furthermore, since the translational registration and myocardial edge point detection are currently applied to one LGE slice after another, theoretically the corresponding computing times can be reduced to $1/N$ of the original if N parallel threads are used with one thread for one slice.

Chapter 6

Conclusion and Future Work

This chapter concludes the thesis and suggests several directions for future work. Section 6.1 summarizes the technical contributions achieved in this thesis. Section 6.2 suggests some directions for future research.

6.1 Conclusion

6.1.1 Myocardium Segmentation

We present a novel 3D segmentation method of the LV in LGE CMR images. Unlike most related works (Ciofolo *et al.*, 2008; Dikici *et al.*, 2004; Wei *et al.*, 2011) which merely used SA images, we also incorporate the standard 4C and 2C LA images to provide supplementary information in the big gaps between contiguous SA slices. Compared to another segmentation method (Ciofolo *et al.*, 2008) which also involved 3D mesh deformation, we realign all the SA slices in a unified 3D coordinate system prior to the mesh construction and deformation, to eliminate potential distortion of the 3D representation caused by

misalignment artifacts. In addition, we propose a novel parametric model of the LV in LGE images based on 1D intensity profiles. This model is able to simultaneously detect paired endocardial and epicardial edge points with varied myocardium thickness, adaptively distinguish between healthy and infarcted myocardium, and readily be applied to both SA and LA images. It is embedded into an energy minimization scheme for reliable detection of myocardial edge points. The experimental results on both real patient and simulated phantom data have shown that our method is able to generate accurate segmentation for LGE images and is robust with respect to varied *a priori* segmentation in the referenced cine images.

6.1.2 Infarct Classification

We present an automatic method for infarct classification within the outlined myocardium in LGE CMR images. This method implements a 3D graph-cut algorithm in the major classification stage to separate the infarcted and normal myocardium by minimizing a joint cost combing both intensity- and spatial-based classification criteria. In this way, it avoids the use of a hard threshold for classification and hence greatly reduces the otherwise potential false positives and negatives. Also due to the employment of the 3D graph-cut algorithm, our method achieves real 3D classification since it segments the LV volume comprised of the stack of SA slices directly. Moreover, misalignment artifacts and intensity inconsistency across slices in an LGE dataset are corrected prior to the major classification stage to avoid potential shape and appearance distortions to the original LV volume. These distortion corrections are crucial to infarct classi-

fication techniques involving multiple slices but were overlooked or incorrectly handled in most related works. The experimental results on 20 sets of real patient data, evaluated both qualitatively and quantitatively, show that our method can reliably and accurately segment infarcts from normal myocardium in LGE CMR images.

6.1.3 Quantification Framework

Overall, this thesis presents a complete 3D framework for automatic quantification of LGE CMR images. This framework achieves 3D segmentation of the myocardium as well as 3D classification of infarcts within the segmented myocardium, with robust and effective pre-processing measures overcoming misalignment artifacts and intensity inconsistency across slices. Qualitative and quantitative evaluations using real patient data demonstrated that the proposed framework is able to produce accurate segmentation and classification results and has the potential to be developed further as a clinical tool to achieve objective quantification of LGE CMR images.

6.2 Limitations and Future Work

From the aspect of experiments, the evaluation of the framework was conducted with limited LGE CMR data (i.e., 20 sets). Future experiments with a much larger cohort are needed to test the proposed methods with more potential variations of the human heart anatomy. Moreover, reliable Kruskal-Wallis tests with the AHA segment order as the factor would be possible with a considerably larger database, other than the slice level used in this work. This would pro-

vide insights specific to every AHA segment. Independent training and testing databases could be employed to test the performance on unfamiliar data, although the methods are not learning based. Another drawback of this work is that we did not explore the potential variations between different human observers. As a study reported volumetric DCs of $80 \pm 8\%$ between the infarcts segmented by two observers given the same myocardial contours (Tao *et al.*, 2010), we expect that, if the observers draw and use their respective delineations of the myocardium, the DC would drop further.

It has recently been reported that the infarcts may not always be homogeneous and that tissue heterogeneity (core and peri-infarct zones) has great diagnostic and predictive potentials (Schmidt *et al.*, 2007; Yan *et al.*, 2006). In future work, we plan to extend our framework to also support differentiation of the infarct core and peri-infarct zones within the identified infarcts. Finally, though the 17^{th} segment in the AHA nomenclature, which stands for the apex in the LA views, is rarely used for the quantification of infarcts, it can provide valuable information on the presence and transmurality of the infarcts right at the apex. Hence we are currently extending our quantification framework to the very apex in 4C and 2C LA views to support the analysis of infarcts there.

With the myocardium segmented and infarcts quantified, we can further extend the analysis of LGE CMR data beyond the LGE CMR itself, that is, more insights for diagnosis and therapy planning can be obtained when the LGE data is combined with complementary types of CMR data. As introduced in Section 2.7, the perfusion CMR contains much fewer slices than the LGE CMR, and the cine CMR, although with comparable number of slices, cannot provide accurate motion analysis of the myocardium. We plan to combine the analysis of tagged

CMR, which has comparable spatial resolution to the LGE CMR and can provide accurate strain tensors of the myocardium, with the analysis of LGE CMR. Since a considerable amount of works have already been done on myocardial motion analysis in the tagged CMR images (e.g., Chandrashekara *et al.*, 2004; Chen *et al.*, 2010; Osman *et al.*, 1999; Smal *et al.*, 2012), analyzing the tagged CMR data would not be an issue. However, at current stage we are not sure about the correlation (if any) between the abnormality in myocardial strain tensors and the pattern of infarcts. Therefore, appropriate statistical analyses with proper quantitative indices are needed for the exploratory research.

References

ABDEL-ATY, H. & TILLMANNS, C. (2010). The use of cardiovascular magnetic resonance in acute myocardial infarction. *Current Cardiology Reports*, **12**, 76–81. 2, 14

AMADO, L., GERBER, B., GUPTA, S., RETTMANN, D., SZARF, G., SCHOCK, R., NASIR, K., KRAITCHMAN, D. & LIMA, J. (2004). Accurate and objective infarct sizing by contrast-enhanced magnetic resonance imaging in a canine myocardial infarction model. *Journal of the American College of Cardiology*, **44**, 2383–2389. 29

AXEL, L., MONTILLO, A. & KIM, D. (2005). Tagged magnetic resonance imaging of the heart: a survey. *Medical Image Analysis*, **9**, 376–393. 33

BARAJAS, J., CABALLERO, K., BARNÉS, J., CARRERAS, F., PUJADAS, S. & RADEVA, P. (2006). Correction of misalignment artifacts among 2-D cardiac MR images in 3-D space. In *First International Workshop on Computer Vision for Intravascular and Intracardiac Imaging, MICCAI 2006*, 114–121. 24, 37

BLAND, J.M. & ALTMAN, D.G. (1986). Statistical methods for assessing agreement between two methods of clinical measurement. *The Lancet*, **327**, 307–310, originally published as Volume 1, Issue 8476. xxv, 107

BOYKOV, Y. & JOLLY, M.P. (2001). Interactive graph cuts for optimal boundary & region segmentation of objects in N-D images. In *Computer Vision, 2001. ICCV 2001. Proceedings. Eighth IEEE International Conference on*, vol. 1, 105–112. 100, 101, 102

BOYKOV, Y., VEKSLER, O. & ZABIH, R. (1998). Markov random fields with efficient approximations. In *Computer Vision and Pattern Recognition, 1998. Proceedings. 1998 IEEE Computer Society Conference on*, 648–655. 101

BOYKOV, Y., VEKSLER, O. & ZABIH, R. (1999). Fast approximate energy minimization via graph cuts. In *Computer Vision, 1999. The Proceedings of the Seventh IEEE International Conference on*, vol. 1, 377–384. 103

BREEUWER, M., PAETSCH, I., NAGEL, E., MUTHUPILLAI, R., FLAMM, S., PLEIN, S. & RIDGWAY, J. (2003). The detection of normal, ischemic and infarcted myocardial tissue using MRI. In *International Congress Series*, vol. 1256, 1153–1158, Elsevier. 32

CERQUEIRA, M.D., WEISSMAN, N.J., DILSIZIAN, V., JACOBS, A.K., KAUL, S., LASKEY, W.K., PENNELL, D.J., RUMBERGER, J.A., RYAN, T. & VERANI, M.S. (2002). Standardized Myocardial Segmentation and Nomenclature for Tomographic Imaging of the Heart. *Circulation*, **105**, 539–542. xviii, 19, 20, 21, 22, 79, 110

CHANDRASHEKARA, R., MOHIADDIN, R. & RUECKERT, D. (2004). Analysis of 3-D myocardial motion in tagged MR images using nonrigid image registration. *Medical Imaging, IEEE Transactions on*, **23**, 1245–1250. 129

CHEN, T., BABB, J., KELLMAN, P., AXEL, L. & KIM, D. (2008). Semiautomated Segmentation of Myocardial Contours for Fast Strain Analysis in Cine Displacement-Encoded MRI. *IEEE Transactions on Medical Imaging*, **27**, 1084–1094. 27

CHEN, T., WANG, X., CHUNG, S., METAXAS, D. & AXEL, L. (2010). Automated 3D Motion Tracking Using Gabor Filter Bank, Robust Point Matching, and Deformable Models. *Medical Imaging, IEEE Transactions on*, **29**, 1–11. 129

CIOFOLO, C., FRADKIN, M., MORY, B., HAUTVAST, G. & BREEUWER, M. (2008). Automatic myocardium segmentation in late-enhancement MRI. In *IEEE ISBI '08*, 225–228. xv, 27, 28, 56, 84, 85, 92, 94, 125

COLLIGNON, A., MAES, F., DELAERE, D., VANDERMEULEN, D., SUETENS, P. & MARCHAL, G. (1995). Automated multi-modality image registration based on information theory. In *Information processing in medical imaging: Proc. 14th Int. Conf. IPMI'95*, vol. 3, 263–274. 56

DELINGETTE, H. (1999). General object reconstruction based on simplex meshes. *International Journal of Computer Vision*, **32**, 111–146. 57, 61, 72, 73, 74, 77

DICE, L. (1945). Measures of the amount of ecologic association between species. *Ecology*, **26**, 297–302. xxv, 82

DIKICI, E., O'DONNELL, T., SETSER, R. & WHITE, R.D. (2004). Quantification of Delayed Enhancement MR Images. In C. Barillot, D.R. Haynor &

P. Hellier, eds., *MICCAI 2004*, vol. 3216 of *LNCS*, 250–257, Springer Berlin / Heidelberg. 27, 56, 92, 125

ELAGOUNI, K., CIOFOLO-VEIT, C. & MORY, B. (2010). Automatic segmentation of pathological tissues in cardiac MRI. In *Biomedical Imaging: From Nano to Macro, 2010 IEEE International Symposium on*, 472–475. 25, 30, 51, 101, 106

ELEN, A., HERMANS, J., GANAME, J., LOECKX, D., BOGAERT, J., MAES, F. & SUETENS, P. (2010). Automatic 3-D Breath-Hold Related Motion Correction of Dynamic Multislice MRI. *IEEE Transactions on Medical Imaging*, **29**, 868–878. 24, 37

FIENO, D., KIM, R., CHEN, E., LOMASNEY, J., KLOCKE, F. & JUDD, R. (2000). Contrast-enhanced magnetic resonance imaging of myocardium at risk* 1:: Distinction between reversible and irreversible injury throughout infarct healing. *Journal of the American College of Cardiology*, **36**, 1985–1991. 2, 14

GONZALEZ, R.C. & WOODS, R.E. (2008). *Digital Image Processing*. Prentice Hall, Upper Saddle River, NJ, 3rd edn. 31, 105

GREIG, D., PORTEOUS, B. & SEHEULT, A. (1989). Exact maximum *a posteriori* estimation for binary images. *Journal of the Royal Statistical Society. Series B (Methodological)*, **51**, 271–279. 103

GUDBJARTSSON, H. & PATZ, S. (1995). The Rician distribution of noisy MRI data. *Magnetic Resonance in Medicine*, **34**, 910–914. 30, 50

HAUTVAST, G., LOBREGT, S., BREEUWER, M. & GERRITSEN, F. (2006). Automatic contour propagation in cine cardiac magnetic resonance images. *IEEE Transactions on Medical Imaging*, **25**, 1472–1482. 27

HEIBERG, E., ENGBLOM, H., ENGVALL, J., HEDSTRÖM, E., UGANDER, M. & ARHEDEN, H. (2005). Semi-automatic quantification of myocardial infarction from delayed contrast enhanced magnetic resonance imaging. *Scandinavian Cardiovascular Journal*, **39**, 267–275. 30

HENNEMUTH, A., SEEGER, A., FRIMAN, O., MILLER, S., KLUMPP, B., OELTZE, S. & PEITGEN, H.O. (2008). A Comprehensive Approach to the Analysis of Contrast Enhanced Cardiac MR Images. *IEEE Transactions on Medical Imaging*, **27**, 1592–1610. 24, 25, 30, 32

HSU, L., INGKANISORN, W., KELLMAN, P., ALETRAS, A. & ARAI, A. (2006a). Quantitative myocardial infarction on delayed enhancement MRI. Part II: Clinical application of an automated feature analysis and combined thresholding infarct sizing algorithm. *Journal of Magnetic Resonance Imaging*, **23**, 309–314. 29

HSU, L., NATANZON, A., KELLMAN, P., HIRSCH, G., ALETRAS, A. & ARAI, A. (2006b). Quantitative myocardial infarction on delayed enhancement MRI. Part I: Animal validation of an automated feature analysis and combined thresholding infarct sizing algorithm. *Journal of Magnetic Resonance Imaging*, **23**, 298–308. 29, 64

HUNOLD, P., SCHLOSSER, T., VOGT, F., EGGEBRECHT, H., SCHMERMUND, A., BRUDER, O., SCHULER, W. & BARKHAUSEN, J. (2005). My-

ocardial late enhancement in contrast-enhanced cardiac MRI: distinction between infarction scar and non-infarction-related disease. *American Journal of Roentgenology*, **184**, 1420–1426. 12, 64

INOUE, Y., YANG, X., NAGAO, M., HIGASHINO, H., HOSOKAWA, K., KIDO, T., KURATA, A., OKAYAMA, H., HIGAKI, J., MOCHIZUKI, T. & MURASE, K. (2010). Peri-infarct dysfunction in post-myocardial infarction: assessment of 3-T tagged and late enhancement MRI. *European Radiology*, **20**, 1139–1148. 33

KAFTAN, J.N., TEK, H. & AACH, T. (2009). A two-stage approach for fully automatic segmentation of venous vascular structures in liver CT images. In J.P.W. Pluim & B.M. Dawant, eds., *Medical Imaging 2009: Image Processing*, vol. 7259, 725911–1–12, SPIE, Orlando, USA. 61

KIM, R.J., FIENO, D.S., PARRISH, T.B., HARRIS, K., CHEN, E.L., SIMONETTI, O., BUNDY, J., FINN, J.P., KLOCKE, F.J. & JUDD, R.M. (1999). Relationship of MRI Delayed Contrast Enhancement to Irreversible Injury, Infarct Age, and Contractile Function. *Circulation*, **100**, 1992–2002. 2, 14

KISHORE, S. & MICHELOW, M. (2011). The global burden of disease. *Public Health in the 21st Century*, **1**, 29–45. 1, 11

KOLIPAKA, A., CHATZIMAVROUDIS, G.P., WHITE, R.D., O'DONNELL, T.P. & SETSER, R.M. (2005). Segmentation of non-viable myocardium in delayed enhancement magnetic resonance images. *International Journal of Cardiovascular Imaging*, **21**, 303–311. 25, 29, 50, 105, 121

KOLMOGOROV, V. & ZABIN, R. (2004). What energy functions can be minimized via graph cuts? *IEEE Transactions on Pattern Analysis and Machine Intelligence*, **26**, 147–159. 103

LI, C., JIA, X. & SUN, Y. (2009). Improved semi-automated segmentation of cardiac CT and MR images. In *Biomedical Imaging: From Nano to Macro, 2009. ISBI '09. IEEE International Symposium on*, 25–28. 27, 58

LIU, Y., XUE, H., GUETTER, C., JOLLY, M.P., CHRISOCHOIDES, N. & GUEHRING, J. (2011). Moving propagation of suspicious myocardial infarction from delayed enhanced cardiac imaging to CINE MRI using hybrid image registration. In *Biomedical Imaging: From Nano to Macro, 2011 IEEE International Symposium on*, 1284–1288. 33

LÖTJÖNEN, J., POLLARI, M., SARI, K. & LAUERMA, K. (2004). Correction of Movement Artifacts from 4-D Cardiac Short- and Long-Axis MR Data. In C. Barillot, D. Haynor & P. Hellier, eds., *MICCAI 2004*, vol. 3217 of *LNCS*, 405–412, Springer Berlin / Heidelberg. 24, 37, 48

MAKELA, T., CLARYSSE, P., SIPILA, O., PAUNA, N., PHAM, Q.C., KATILA, T. & MAGNIN, I. (2002). A review of cardiac image registration methods. *Medical Imaging, IEEE Transactions on*, **21**, 1011–1021. 33

MCLEISH, K., HILL, D., ATKINSON, D., BLACKALL, J. & RAZAVI, R. (2002). A study of the motion and deformation of the heart due to respiration. *IEEE Transactions on Medical Imaging*, **21**, 1142–1150. 23, 28, 37, 94

METWALLY, M., EL-GAYAR, N. & OSMAN, N. (2010). Improved technique to detect the infarction in delayed enhancement image using k-mean method. *Image Analysis and Recognition*, 108–119. 30

NOBLE, N.M., HILL, D.L., BREEUWER, M. & RAZAVI, R. (2004). The automatic identification of hibernating myocardium. In C. Barillot, D.R. Haynor & P. Hellier, eds., *Medical Image Computing and Computer-Assisted Intervention – MICCAI 2004*, vol. 3217 of *Lecture Notes in Computer Science*, 890–898, Springer Berlin / Heidelberg. 32

OSMAN, N.F., KERWIN, W.S., MCVEIGH, E.R. & PRINCE, J.L. (1999). Cardiac motion tracking using CINE harmonic phase (HARP) magnetic resonance imaging. *Magnetic Resonance in Medicine*, **42**, 1048–1060. 129

OTSU, N. (1979). A threshold selection method from gray-level histograms. *IEEE Transactions on Systems, Man and Cybernetics*, **9**, 62–66. 30, 65

PENNEY, G., WEESE, J., LITTLE, J., DESMEDT, P., HILL, D. & HAWKES, D. (1998). A comparison of similarity measures for use in 2-D-3-D medical image registration. *IEEE Transactions on Medical Imaging*, **17**, 586–595. 94

PETITJEAN, C. & DACHER, J.N. (2011). A review of segmentation methods in short axis cardiac MR images. *Medical Image Analysis*, **15**, 169–184. 82, 96

RAHIMTOOLA, S. (1989). The hibernating myocardium. *American Heart Journal*, **117**, 211–230. 11, 31

REIMER, K., JENNINGS, R. *et al.* (1979). The "wavefront phenomenon" of myocardial ischemic cell death. II. Transmural progression of necrosis within

the framework of ischemic bed size (myocardium at risk) and collateral flow. *Laboratory Investigation*, **40**, 633–644. 12, 64

RYF, S., RUTZ, A.K., BOESIGER, P. & SCHWITTER, J. (2006). Is Post-Systolic Shortening a Reliable Indicator of Myocardial Viability? An MR Tagging and Late-Enhancement Study. *Journal of Cardiovascular Magnetic Resonance*, **8**, 445–451. 33

SCHMIDT, A., AZEVEDO, C., CHENG, A., GUPTA, S., BLUEMKE, D., FOO, T., GERSTENBLITH, G., WEISS, R., MARBAN, E., TOMASELLI, G. *et al.* (2007). Infarct tissue heterogeneity by magnetic resonance imaging identifies enhanced cardiac arrhythmia susceptibility in patients with left ventricular dysfunction. *Circulation*, **115**, 2006–2014. 128

SEGARS, W.P., STURGEON, G., MENDONCA, S., GRIMES, J. & TSUI, B.M. (2010). 4D XCAT phantom for multimodality imaging research. *Medical Physics*, **37**, 4902–4915. xxv, 79

SMAL, I., CARRANZA-HERREZUELO, N., KLEIN, S., WIELOPOLSKI, P., MOELKER, A., SPRINGELING, T., BERNSEN, M., NIESSEN, W. & MEIJERING, E. (2012). Reversible jump MCMC methods for fully automatic motion analysis in tagged MRI. *Medical Image Analysis*, **16**, 301–324. 129

TAO, Q., MILLES, J., ZEPPENFELD, K., LAMB, H., BAX, J., REIBER, J. & VAN DER GEEST, R. (2010). Automated segmentation of myocardial scar in late enhancement MRI using combined intensity and spatial information. *Magnetic Resonance in Medicine*, **64**, 586–594. xvi, 25, 30, 31, 50, 103, 105, 106, 108, 110, 128

VALINDRIA, V.V., ANGUE, M., VIGNON, N., WALKER, P.M., COCHET, A. & LALANDE, A. (2011). Automatic Quantification of Myocardial Infarction from Delayed Enhancement MRI. In *Signal-Image Technology and Internet-Based Systems (SITIS), 2011 Seventh International Conference on*, 277–283. 19, 25, 30, 106

VU, N., GHOSH, P. & MANJUNATH, B. (2007). Retina layer segmentation and spatial alignment of antibody expression levels. In *IEEE ICIP 2007*, vol. 2, II –421 –II –424. 61

WEESE, J., BUZUG, T., LORENZ, C. & FASSNACHT, C. (1997). An approach to 2D/3D registration of a vertebra in 2D x-ray fluoroscopies with 3D CT images. In J. Troccaz, E. Grimson & R. Mösges, eds., *CVRMed-MRCAS'97*, vol. 1205 of *LNCS*, 119–128, Springer Berlin / Heidelberg. xxv, 56, 58

WEI, D., SUN, Y., CHAI, P., LOW, A. & ONG, S.H. (2011). Myocardial Segmentation of Late Gadolinium Enhanced MR Images by Propagation of Contours from Cine MR Images. In G. Fichtinger, A. Martel & T. Peters, eds., *MICCAI 2011*, vol. 6893 of *Lecture Notes in Computer Science*, 428–435, Springer Berlin / Heidelberg. xv, 28, 55, 58, 61, 64, 84, 85, 92, 119, 125

YAN, A., SHAYNE, A., BROWN, K., GUPTA, S., CHAN, C., LUU, T., DI CARLI, M., REYNOLDS, H., STEVENSON, W. & KWONG, R. (2006). Characterization of the peri-infarct zone by contrast-enhanced cardiac magnetic resonance imaging is a powerful predictor of post-myocardial infarction mortality. *Circulation*, **114**, 32–39. 105, 128

ZADICARIO, E., AVIDAN, S., SHMUELI, A. & COHEN-OR, D. (2008). Boundary snapping for robust image cutouts. In *IEEE CVPR 2008*, 1–8. 61

ZERHOUNI, E., PARISH, D., ROGERS, W., YANG, A. & SHAPIRO, E. (1988). Human heart: tagging with MR imaging–a method for noninvasive assessment of myocardial motion. *Radiology*, **169**, 59–63. 18

Publication List

[1] WEI, D., SUN, Y., CHAI, P., LOW, A. & ONG, S.H. (2011). Myocardial Segmentation of Late Gadolinium Enhanced MR Images by Propagation of Contours from Cine MR Images. In G. Fichtinger, A. Martel & T. Peters, eds., *MICCAI 2011*, vol. 6893 of *Lecture Notes in Computer Science*, 428–435, Springer Berlin / Heidelberg.

[2] WEI, D., SUN, Y., ONG, S.H., CHAI, P., TEO, L.L. & LOW, A. (2013). A Comprehensive 3-D Framework for Automatic Quantification of Late Gadolinium Enhanced Cardiac Magnetic Resonance Images. *Biomedical Engineering, IEEE Transactions on*, **60**, 1499–1508.

[3] WEI, D., SUN, Y., ONG, S.H., CHAI, P., TEO, L.L. & LOW, A. (2013). Three-Dimensional Segmentation of the Left Ventricle in Late Gadolinium Enhanced MR Images Combining Long- and Short-Axis Information. *Medical Image Analysis*, **in press**.